Nanoscale

GISAXS

BornAgain

Holograhpy

PNR

Magnetometry

Magnetoelectric

10 nm

Fe Au O Ti Ba

Manipulation of magnetism in iron oxide nanoparticle / BaTiO₃ composites and low-dimensional iron oxide nanoparticle arrays

Li-Ming Wang

JÜLICH
Forschungszentrum

Manipulation of magnetism in iron oxide nanoparticle / BaTiO$_3$ composites and low-dimensional iron oxide nanoparticle arrays

Li-Ming Wang

II

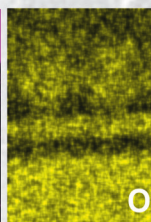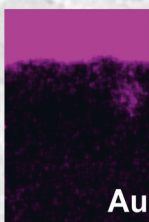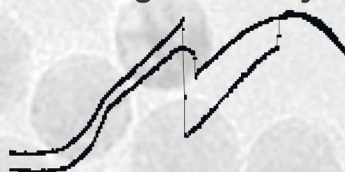## Zusammenfassung

Es wurden ferrimagnetische Eisen-Sauerstoff Nanopartikel (NP) auf ferroelektrischen $BaTiO_3$-Substraten (BTO) hergestellt. An diesen Hererostrukten konnte eine magnetoelektrische Kopplung (MEC) festgestellt werden. Zuerst wurde eine Einzelschicht von Eisen-Sauerstoff NP durch Selbstorganization auf einem BTO Einkristallsubtrat aufgebracht. Durch Röntgenstreuung unter streifendem Einfall (GISAXS) und Rasterelektronenmikroskopie (SEM) wurde gezeigt, dass die NP Einzelschicht eine dicht gepackte hexagonale Struktur aufweist. Der MEC Effect konnte durch Einbringen einer Ti-Schicht und Bedecken mit einer Au-Schicht verstärkt werden. Die Raster-Transmissionselektronenmikroskopie (STEM) lieferte Informationen über die Schichtstruktur der Probe. Die Magnetisierung zeigt scharfe Sprünge bei den Phasenübergängen des BTO-Stubtrats.

Die Manipulation der Magnetisierung durch elektrische Felder wurde mit einer supraleitenden Quanteninterferenzeinheit (SQUID) mit eingebautem elektrischem Feld durchgeführt. Die Magnetisierung aufgetragen gegen das DC elektrische Feld hat eine Schmetterlingsform und stimmt mit der piezoelektrischen Reaktion des BTO Einkristalls überein. Dies bestätigt, dass der MEC hauptsächlich durch die Grenzflächenspannungen übermittelt wird. Das Signal der magnetoelektrischen AC Suszeptibilität (MEASCS) als Funktion der Temperatur bei angelegtem AC elektrischen Feld zeigt Sprünge bei den BTO Phasenübergängen.

Das magnetische Tiefenprofil der NP Einfachschicht bei variierten angelegten DC elektrischen Feldern wurde von den Ergebnissen der polarisierten Neutronenreflektometrie (PNR) abgeleitet. Die Unterschiede bei den Reflektometriekurven werden hauptsächlich durch die strukturellen Änderungen des Substrates und der Einzelschichten hervorgerufen. Zusätzlich hat die veränderte Magnetisierung der NP Einzelschichten einen kleineren Effekt auf die Unterschiede in den Reflektometriekurven.

Es wurden zusätzlich selbstorganisierte Eisen-Sauerstoff NP auf einer BTO-Schicht auf einem Nb dotiertem $SrTiO_3$ Substrat (Nb doped STO) hergestellt. Andererseits deuteten die Messungen der Magnetisierung als Funktion des DC elektrischen Feldes und die MEACS Resultate an, dass ein MEC zwischen NP und der BTO-Schicht vorliegt. Öberflächenladungen und Spannungsübertragungen an der Grenzschicht sind für den MEC verantwortlich.

Zusätzlich wurden selbstorganisierte NP in lateral strukturierten Silizium-Substraten (Si) hergestellt um die magnetische Anisotropie und das kollektive magnetische Verhalten zu untersuchen. Die Magnetisierung als Funktion des magnetischen Feldes zeigt einen großen strukturinduzierten magnetischen Anisotropieeffekt. Die Resultate der Elektronenholographie, nach dem Anlegen eines magnetischen Sättigungsfeldes entlang der lateralen Strukturen, zeigen, dass ein geordneter magnetischer Zustand in den NP-Anordnungen existiert. Die NP zeigen einen ferromagnetisch (FM) geordneten Zustand und einen kleinen Memory-Effekt entlang der lateralen Strukturen an. Senkrecht zu den lateralen Strukturen wird aber ein großer Memory-Effekt

beobachtet. Wir folgern daraus, dass der FM geordnete Zustand den Superspin-Glas Zustand der dipolar gekoppelten NP unterdrückt.

Diese Arbeit eröffnet viele Möglichkeiten für energieeffiziente elektronische Bauteile hergestellt durch einfache Selbstanordnungstechniken.

Abstract

Ferrimagnetic (FiM) iron oxide nanoparticles (NPs) on top of ferroelectric $BaTiO_3$ (BTO) substrates were prepared and a magnetoelectric coupling (MEC) effect was observed in the heterostructures. Iron oxide NPs first were self-assembled as a monolayer on top of BTO substrates. Grazing incidence small angle x-ray scattering (GISAXS) and scanning electron microscopy (SEM) confirm a close-packed hexagonal order of the NP monolayers. By inserting a Ti layer and further capping with an Au layer, an enhanced MEC effect was observed. Scanning transmission electron microscopy (STEM) provides information about the layer structure of the sample. The magnetization shows sharp magnetization jumps at the phase transition temperatures of the BTO substrate.

Electric field manipulation of magnetism was performed using a superconducting quantum interference device (SQUID) setup with an electric field implemented. A butterfly shaped curve of the magnetic moment vs. DC electric field was obtained which is coincident with the piezoelectric response of BTO single crystals which confirms a strain mediated MEC. The magnetoelectric ac susceptibility (MEACS) signal as function of temperature under an AC electric field shows abrupt jumps at the BTO phase transition temperatures.

The magnetic depth profiles of NP monolayers at various applied DC electric fields were deduced from polarized neutron reflectivity (PNR) results. Fitting of the data shows that the observed differences in reflectivity curves are caused by the changed structural properties of the substrate and layers as a major factor and the altered magnetism of NP monolayers as a minor factor.

Also iron oxide NPs self-assembled on BTO films on Nb doped $SrTiO_3$ (Nb doped STO) substrates were prepared. The DC electric field vs. magnetization and MEACS results indicate that there is a MEC between NPs and the BTO film. Interface charge and strain transfer are responsible for the MEC effects.

Moreover, NPs self assembled into trench-patterned silicon (Si) substrates were prepared to investigate the magnetic anisotropy and collective magnetic behavior. The magnetization vs. magnetic field shows a large shape-induced magnetic anisotropy effect. After the application of a magnetic saturation field along the trenches, electron holography results show that an overall magnetic ordered state exists in the nanoparticle assemblies. In the direction of the trenches, the NPs exhibit a ferromagnetic (FM) -like ordered state and a small memory effect was observed. Whereas large memory effect was observed perpendicular to the trenches. We conclude that the FM ordered state suppresses a superspin glass state of the dipolarly coupled NP moments.

This work opens up viable possibilities for energy-efficient electronic devices fabricated by simple self-assembly techniques.

Contents

Chapter 1

Introduction

Magnetoelectric (ME) materials are systems where the magnetization can be manipulated by electric field or the polarization can be tuned by magnetic field [1, 2]. They have stimulated large research interest due to their potential applications in spintronics or multifunctional devices [3, 4, 5, 6]. For storage devices, ME artificial heterostructures can combine the advantages of ferroelectric random access memories (FERAMs) and magnetic random access memories (MRAMs) [7, 8].

Moreover, the ability to switch the magnetization via an electric field in ME materials could reduce the energy consumption to write data in electronic devices and also offers the possibility to scale down MRAMs even further [7, 9, 8]. Single-phase ME systems are rare and most of them only show an ME effect at low temperature or in a narrow temperature range [10, 11, 12, 13]. Alternatively, with greater design flexibility, multiferroic ME composites fabricated by combining piezoelectric and magnetic materials have drawn significant interest in recent years due to their multifunctionality and a large ME response (i.e., several orders of magnitude larger than in single-phase ME materials) [14, 15].

Recently, strain mediated ME coupling (MEC) effects were evidenced in various thin film systems composed of a ferromagnetic (FM) Fe, $SrRuO_3$ or $La_{0.7}Sr_{0.3}MnO_3$ layer on top of a ferroelectric (FE) substrate, e.g. BTO or $PbMg_{1/3}Nb_{2/3}O_3$ - $PbTiO_3$ (PMN-PT). The coupling is manifested as a change of the magnetization or resistance at the structural phase transition temperatures of the ferroelectric subsystem [16, 17, 18, 19, 20]. These studies argue that the MEC effects are the result of strain-mediated coupling, partially strain and partially charge mediated or purely charge-mediated coupling.

FM-FE or FiM-FE composites based on magnetic NPs are promising novel candidates for artificial nanoscale multiferroic devices [21, 22]. For example, they can be used for fabricating flexible electronics and provide the possibility of cost-efficient manufacturing via spin-coating or printing methods. A recent study showed that switching of the magnetic properties of Ni nanocrystals between a superparamagnetic (SPM) and a stable FM state by MEC to a FE substrate is possible [23]. In addition, NPs can be considered as building blocks for artificial superstructures [24, 25, 26]. One prominent route is to employ the self-organization of

NPs into regular arrangements, so called "supercrystalline lattices" or "supercrystals" [27, 28]. Such systems are particularly interesting, because of their prospective applications as multifunctional materials.

However, the understanding of ME systems including supercrystalline NP assemblies is still very limited and consequently several open questions remain, e.g. what is the exact mechanism of MEC in such nanocomposites? How can it be tuned and optimized? Therefore, we investigate strain and electric field mediated MEC in a model system composed of a monolayer of self-assembled iron oxide NPs coupled to a BTO substrate.

Large-areas of NP arrangements with long-range order with a desired morphology is an essential step to the fabrication of novel nanoelectronics, magnetoelectronics, biochemical sensors. The assembly of 1 or 2 dimensional (1D or 2D) nanoscale colloidal structures are very promising for this purpose [29, 30, 31]. An efficient route to prepare (pseudo-) 1D NP chains is the template-assisted fabrication [32, 33, 34, 35]. These methods have been widely used to self-assemble metallic NPs into long-range ordered pseudo-1D NP chains. For example, M. Kang et al. reported 1D Au NP arrays encapsulated within free-standing SiO_2 nanowires [36]. D. Xia et al. demonstrated directed self-assembly of silica NPs into nanometer-scale grooves patterned surfaces [30]. Although some FM / FiM NPs also was tried with the methods, Park and co-workers reported the assembly of iron oxide NPs into 200 nm chains using a bio-inspired template [34]. Nevertheless, the fabrication of long-rang order (pseudo-) 1D FM / FiM NP chains across large areas are still challenging.

Besides applications, such NP arrangements also play critical roles in the understanding of fundamental magnetism. Interparticle dipole-dipole interactions can lead to collective spin-glass ordering at low enough temperature. Interaction between magnetic entities causes collective phenomena at low enough temperatures, provided the dimensionality of the system is above the lower critical dimension [37]. Interacting magnetic nanoparticles can exhibit the same phenomenology as atomic spin glasses, namely superspin glass (SSG) state. Memory effect is the most significant feature of the SSG state and is widely accepted as the most direct and straightforward criterion to judge whether it is a superspin glass state.

SSG systems have received much attention in recent years for their appealing novel properties such as nonexponential relaxation, aging and memory effect [38, 39, 40]. Among them, NP systems with dipole-dipole interactions (superspins, spins in a single domain NP can be regarded as a superspin) are the most attractive SSG systems to be investigated for their easy self-assembly methods and their attractive properties. Magnetic anisotropy and the SSG state are investigated on low dimensional iron oxide NPs in patterned substrates.

This thesis is structured as follows: a short theoretical background about magnetism is given in chapter 2, it includes a description of various types of magnetic interactions and four types of magnetic orders which are most frequently mentioned in the following chapters. Afterwards, superparamagnetism is briefly explained to get a better understanding of the magnetic behavior of NPs. The structures and magnetic behavior of the several basic iron oxides are illustrated in the next section.

The ferroelectric properties of $BaTiO_3$ and the magnetoelectric materials are introduced afterwards. Since scattering methods are used extensively for the investigation of our system, the theoretical background of scattering methods are summarized. The experimental instruments are described in the chapter 3 to provide an overview of the methods we used in our investigations. The results of the magnetic and structural properties of NPs on different substrates are presented in chapter 4 to 6. The discussion on observed effects and the outlook for future investigations are given in chapter 7.

Chapter 2

Theoretical Background

2.1   Magnetic susceptibility

For magnetic materials, after applying an external magnetic field $\vec{H}$, a magnetization (magnetic moment per volume) $\vec{M}$ is generally induced. In the simplest case of a linear and isotropic response, one can write:

$$\vec{M} = \chi \vec{H} \tag{2.1}$$

where χ is the magnetic susceptibility. It is a dimensionless quantity. The magnetic materials can roughly be distinguished in three classes. When $\chi < 0$, it is diamagnetic, when $\chi > 0$, it is paramagnetic and when $\chi \gg 1$, it is ferromagnetic.

2.2   Magnetic interactions

In diamagnetism or paramagnetism for localized moments, the magnetic moments are independent and very weak magnetic interaction exist. However, some solids can show long range magnetic order. When the orientation of the moments points in the same direction, the system is known as ferromagnetic. When the ordering is alternating in opposite directions, it is known as antiferromagnetic. When the ordering is in opposite directions but with different magnitudes of the sublattice moments, it is known as ferrimagnetic. The various interactions will be briefly discussed in this section.

2.2.1   Magnetic dipolar interaction

Magnetic moments show dipole-dipole interactions amongst them. The energy between two moments $\vec{\mu_1}$ and $\vec{\mu_2}$ separated by $\vec{r}$ is given by

$$E_d = \frac{\mu_0}{4\pi r^3}[\vec{\mu_1} \cdot \vec{\mu_2} - \frac{3}{r^2}(\vec{\mu_1} \cdot \vec{r})(\vec{\mu_2} \cdot \vec{r})] \tag{2.2}$$

The energy depends on the separation and the orientation of the moments. The order of magnitude for two atomic moments each of $\mu \approx 1\mu_B$ separated by 1 Å is approximately 10^{-23} J which is equivalent to about 1K in temperature.

As for nanoparticles, since the total moment is 10^6 times larger than atomic moments, the dipolar ordering energy can be as large as thousands of Kelvin. For example, two iron oxide NPs with the diameter of 20 nm, has the moment μ of 3.7×10^6 μ_B and a center to center separation of $r = 20$ nm, the energy scale is around 2100 K.

2.2.2   Exchange interaction

The most significant interaction responsible for long-range magnetic order is exchange interaction. The origin can be explained by taking into account the electrostatic interaction between electrons.

The Pauli exclusion principle states that two or more fermions of the same kind cannot be in the same state. Hence, considering a simple system of two electrons, the overall wavefunction of the electrons must be antisymmetric. The wavefunction can be separated into a spatial part and a spin part. When the spin part is antisymmetric, the spatial part must be symmetric (singlet state, $S = 0$) and vice versa (triplet state, $S = 1$).

The exchange constant J is defined as the energy difference between the triplet state and singlet state.

$$J = \frac{E_S - E_T}{2} \tag{2.3}$$

Hence, the spin-dependent term in the effective Hamiltonian can be expressed as

$$\hat{H}^{spin} = -2J\vec{S}_1 \cdot \vec{S}_2 \tag{2.4}$$

If $J > 0$, the spatial wavefunction of the two electrons is antisymmetric, exchange energy favors electrons with parallel spins. If $J < 0$, the spatial part is symmetric, the interaction favors electrons with antiparallel spins.

However, in a many-body system, the Hamiltonian is written as

$$\hat{H}^{spin} = -\sum_{ij} J_{ij}\vec{S}_1 \cdot \vec{S}_2 \tag{2.5}$$

where J_{ij} is the exchange constant between the ith and j^{th} spins. This is called Heisenberg Hamiltonian.

The exchange interaction can be further subdivided into the following types.

Direct exchange

If electrons on neighboring magnetic atoms interact via an exchange interaction, this is known as direct exchange. The exchange interaction proceeds directly without an intermediary. It gives a strong, but short range coupling which decreases rapidly as the ions are separated.

Direct exchange interaction plays sometimes a role in NP self-assemblies, where the surfaces of the NPs are in close contact.

Indirect exchange: Superexchange

Indirect exchange interaction exists in several magnetic materials, e.g. in oxides or fluorides, as in MnO and MnF_2. There the direct orbital overlap between Mn^{2+} ions is not possible. The magnetic ions interact via a non-magnetic ion like oxygen. Such an interaction is called superexchange interaction.

Indirect exchange: RKKY

In metals the exchange interaction between magnetic ions can be mediated by conduction electrons. A localized magnetic moment polarizes the conduction electrons, which in turn couples to another localized magnetic ion and influences its magnetic state. This kind of indirect exchange is called Ruderman, Kittel, Kasuya and Yosida (RKKY) interaction. The coupling depends on the distance (hereby $r \gg k_F^{-1}$) and is given by

$$J_{RKKY}(r) \propto \frac{\cos(2k_F r)}{r^3} \tag{2.6}$$

where r is the distance between the localized magnetic moments and k_F is the radius of the Fermi surface. The interaction is long range and oscillatory in nature. The interaction leads to FM and AF coupling depending on the distance.

Double exchange

In some solids, the magnetic ion can show mixed valency. Then it has the possibility to show a FM interaction amongst the ions which is known as double exchange. E.g. in magnetite, in octahedral environment, due to the crystal field splitting effect, the Fe d-orbital will split into e_g and t_{2g} level with the former level having higher energy.
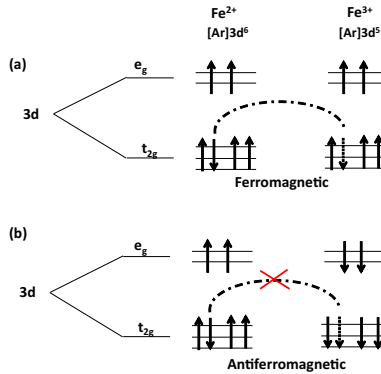

Figure 2.1: Double exchange interaction between octahedrally coordinated Fe^{2+} and Fe^{3+} in magnetite. (a) Electron hopping is allowed from Fe^{2+} to Fe^{3+} for ferromagnetic alignment. (b) Forbidden electron hopping in case of antiferromagnetic alignment due to the Pauli exclusion principle.

The configuration for Fe^{2+} and Fe^{3+} is shown in Figure 2.1. The electron hopping between Fe^{2+} and Fe^{3+} leads to an effective FM interaction, because the electron delocalization and a parallel spin alignment lowers the energy of the system. Hence, double exchange interaction leads to ferromagnetism.

2.3   Magnetic order

Depending on the interactions between magnetic moments, a solid can show various types of long-range magnetic order.

2.3.1   Ferromagnetism (FM)

When the moments are parallel to each other in its ground state, then this system is known as ferromagnet. A ferromagnet shows spontaneous magnetization in absence of a magnetic field. This is the case when J > 0. In general one can write for a system with exchange interactions in an applied magnetic field B,

$$H = -\sum_{ij} J_{ij} \vec{S}_i \cdot \vec{S}_j + g\mu_B \sum_{j} \vec{S}_j \cdot \vec{B} \qquad (2.7)$$

where $\vec{S}$ is the spin vector operator. The first term is the Heisenberg exchange item while the second term is the Zeeman item. The exchange constants J_{ij} for the nearest neighbors are positive for the case of ferromagnetic alignment.

The Weiss model is used to explain the origin of FM. In this model, the interaction between the moments is treated in such a way that each moment experiences a mean field (or "molecular field"). After neglect the thermal fluctuation effect, the effective mean field is given by

$$\vec{B}_{mf} = \lambda \vec{M} \qquad (2.8)$$

where λ is a constant known as Weiss coefficient and $\vec{M}$ is the magnetization. We are now able to treat the problem as a paramagnet placed in a magnetic field $\vec{B} + \vec{B}_{mf}$. At low temperatures, the moments are aligned by the internal mean field even without external magnetic field. As the temperature increases, thermal fluctuations begin to gradually destroy the aligned moments and finally at a critical temperature, the order becomes destroyed.

The susceptibility of ferromagnet is expressed as,

$$\chi \propto \frac{1}{T - T_C} \qquad (2.9)$$

Where T_C is the so-called Curie temperature. This is known as the Curie-Weiss law [41].

2.3.2 Antiferromagnetism (AF)

If the exchange interaction is negative, J < 0, the magnetic moments are aligned antiparallel to the nearest neighbors. This is called antiferromagnetism. Usually, it is considered as two interpenetrating sublattices (see Figure 2.2). One sublattice with all moments pointing up and the other with all moments pointing down. If we
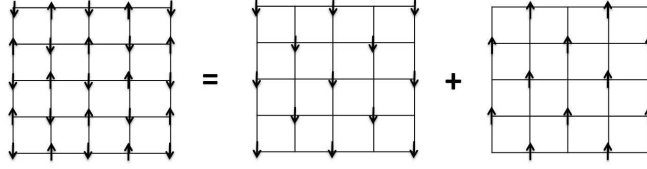
Figure 2.2: Antiferromagnetic moments configuration can be decomposed into two interpenetrating sublattices.

label the 'up' sublattice + and the 'down' sublattice -, then similar to a ferromagnet, the molecular field can be written as

$$B_+ = -|\lambda|M_- \tag{2.10}$$

$$B_- = -|\lambda|M_+ \tag{2.11}$$

The magnetization of each sublattice can be written as

$$M_\pm = M_s B_j \left(\frac{g_J \mu_B J |\lambda| M_\mp}{k_B T} \right) \tag{2.12}$$

The magnitude of the sublattices magnetizations are herby equal.

$$|\vec{M}_+| = |\vec{M}_-| = |M| \tag{2.13}$$

Analogous to the ferromagnet one can solve it as mean field problem and arrives at

$$\chi \propto \frac{1}{T - \theta} \tag{2.14}$$

where θ is the Weiss temperature. If $\theta = 0$, the material is paramagnetic, the material is FM, if $\theta > 0$, if $\theta < 0$, the material is a antiferromagnetic (AF).

There is a phase transition between AF to paramagnetic state, the temperature for the phase transition is called Néel temperature (T_N) [42].

The temperature dependence of the susceptibilities parallel and perpendicular to the easy axis are shown in Figure 2.3.

Figure 2.3: Temperature dependence of the susceptibility of an antiferromagnet for susceptibilities parallel and perpendicular to the easy axis. Taken from Ref. [42]
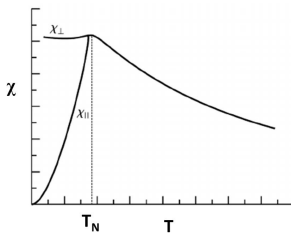
2.3.3   Ferrimagnetism (FiM)

If the two sublattices as described in the antiferromagnet have different magnitudes of the magnetic moment, $|M_+| \neq |M_-|$, then the sublattices can not cancel out and a net magnetization is expected. This is known as Ferrimagnetism (FiM).

Magnetite (Fe_3O_4) is a typical FiM material containing an equal mixture of Fe^{2+} and Fe^{3+} ions on octahedral sites, together with the same number of Fe^{3+} ions on tetrahedral sites. The Fe^{2+} and Fe^{3+} ions on octahedral sites are parallel aligned, the Fe^{3+} ions on the tetrahedral sites are antiparallel aligned to the Fe^{3+} ions on octahedral sites. Hence the net magnetization from all Fe^{3+} ions is zero and leave a net moment due to the Fe^{2+} ions alone. Magnetite shows a T_C at 858 K.

2.3.4   Spin glasses (SG)

Spin glasses (SG) are magnetic systems in which no conventional long-range order can be established. However, they exhibit a freezing transition to a state with new kind of order in which the spins are oriented in random directions [43]. This temperature is called SG transition temperature T_g.

The SG state can be induced when spin fullfills the both conditions of disorder and frustration. The disordered spins can be induced by position disorder and anisotropy disorder while the their frustration can be induced from RKKY effect or dipole-dipole interaction [44].

The most familiar and well studied SG systems are the dilute magnetic alloys such as AuFe, AgMn and CuMn, so-called canonical SG [45, 46, 47]. The localized moments of randomly distributed magnetic moments interact with each other via the $s-d$ exchange interaction mediated by the conduction electrons, the RKKY interaction. The oscillating nature of the RKKY interaction with distance, combined with spatially random arrangement of localized moments, gives rise to frustration and randomness. With the neglect of spin anisotropy, the canonical SG is well described by the three-dimensional (3D) Heisenberg model [48]. For example, AuFe, Fe 8 at.%, Fe substitutes few sites in non magnetic Au lattice in a random distribution, then the system shows a disordered state. The temperature dependence of both Hall resistivity and magnetization show a cusp at T_g and the ZFC and FC

hysteresis below T_g [45].

Analogously to the SG state in bulk materials, interacting single-domain NPs also show such state which is called superspin glass (SSG) state. Due to the large magnetic moments of NPs (superspins), the dipole–dipole interaction is considerable in closely packed nanoparticles assemblies [40, 49, 50].

2.4 Magnetic anisotropy

An important energy contribution determines the direction of spontaneous magnetization in a magnetic material, which is known as the magnetic anisotropy. One observes two different directions in the materials, known as easy axis and hard axis. Along the easy axis, it is easy to magnetize the material, and during a magnetization reversal process, a smaller magnetic field is required. For determining the overall anisotropy in a bulk material, magnetocrystalline anisotropy and magnetostatic demagnetization should be taken into consideration in the first place, while in nanostructures, the shape, surface and strain anisotropy need to be considered preferentially [24].

2.4.1 Magnetocrystalline anisotropy

Magnetic moments in a crystal are in an environment of a periodic lattice. The wavefunctions of neighboring moments exhibit different overlap energies for varied orbital moment orientations, which together with the spin-orbit interaction is the cause of magnetocrystalline anisotropy. Along certain crystallographic directions, it is easy to magnetize the crystal. In some cases, crystallographic directions are preferred over shape, surface and any other effects for the orientation of the magnetization.

For a hexagonal lattice, the easy axis is along the c-axis of the unit cell, which is known as uniaxial anisotropy. The energy associated with it is expressed as

$$E_{uni} = K_{u1}V sin^2\phi + K_{u2}V sin^4\phi + ... \qquad (2.15)$$

where K_{u1}, K_{u2} etc. are the anisotropy constants, V is the volume and ϕ is the angle between the easy axis and magnetic moment direction. The anisotropy constants show a strong temperature dependency, however, it can be regarded as a constant when the temperature is well below T_C. In most cases, K_{u1} is, by far, larger than the following terms and hence, the higher order terms can be neglected. Hence, the magnetocrystalline anisotropy energy can be simplified to $E_{uni} = K_{u1}V sin^2\phi$. It can be seen that, to switch the magnetic moments, one has to overcome an energy barrier $\sim K_{u1}V$.

For a cubic system, the anisotropy is expressed as

$$E_{cubic} = K_1(\frac{1}{4}sin^2\theta sin^2 2\phi + cos^2\theta)sin^2\theta + \frac{K_2}{16}sin^2 2\phi sin^2 2\theta sin^2\theta + ... \qquad (2.16)$$

where θ and ϕ are the polar and azimuthal angles between the favored direction and the magnetic moment, respectively.

2.4.2   Shape anisotropy

The shape of the material also creates an additional anisotropy due to the demagnetization energy. A magnetized body produces magnetic "charges" or poles at the surface. This surface charge distribution is itself another source of a magnetic field, called the demagnetizing field. This will act in opposition to the magnetization that produces it. The demagnetization energy can be written as

$$E_{dm} = -\frac{\mu_0}{2} \int \vec{M} \cdot \vec{H}_{dm} dV \tag{2.17}$$

where $\vec{M}$ is the magnetization and $\vec{H}_{dm}$ is the demagnetization field. A spherical body has zero shape anisotropy. However, in a ellipsoidal body, the demagnetizing energy is smaller if the magnetization lies along the long axis than along the short axes. Hence, it produces an easy axis of magnetization along the long axis. The demagnetization energy of a magnetized ellipsoid is given by

$$E_{dm} = \frac{1}{2}V\mu_0 M_S^2 sin^2\theta(N_\perp - N_\parallel) \tag{2.18}$$

where M_S is the saturation magnetization of the material, θ is the angle between long axis and the direction of M_S. $N_\parallel$ and $N_\perp$ are the demagnetization factors, parallel or perpendicular with respect to the long axis of the ellipse, respectively. Both factors are a function of the ellipticity k of the particles as

$$N_\parallel = \frac{1}{k^2 - 1}\left(\frac{k}{2\sqrt{k^2-1}}\ln(\frac{k+\sqrt{k^2-1}}{k-\sqrt{k^2-1}}) - 1)\right) \tag{2.19}$$

$$N_\perp = \frac{k}{2(k^2-1)}\left(k - \frac{1}{2\sqrt{k^2-1}}\ln(\frac{k+\sqrt{k^2-1}}{k-\sqrt{k^2-1}})\right) \tag{2.20}$$

The demagnetization factors always satisfy the condition $N_\parallel + 2N_\perp =1$ [51]. The magnitude of shape anisotropy depends on the saturation magnetization.

2.4.3   Surface anisotropy

Atoms at the surface are unsaturated, which leads to an enhancement of the anisotropy energy. Especially in reduced dimensional systems, surface anisotropy plays a dominant role over magnetocrystalline anisotropy and magnetostatic energies. In case of small spherical particles, the effective magnetic anisotropy can be written as

$$K_{eff} = K_V + \frac{S}{V}K_S = K_V + \frac{6}{d}K_S \tag{2.21}$$

where $S = \pi d^2$ and $V = \pi d^3/6$ are the surface and volume of the particles. S/V is the ratio of surface to volume, and d is the diameter of the particle. K_V and K_S are the volume and surface anisotropies, comprising the terms of magnetocrystalline, shape and magnetostriction terms, respectively [52, 53]. A simulated spin structure in dependence of K_V and K_S is depicted in Figure 2.4.
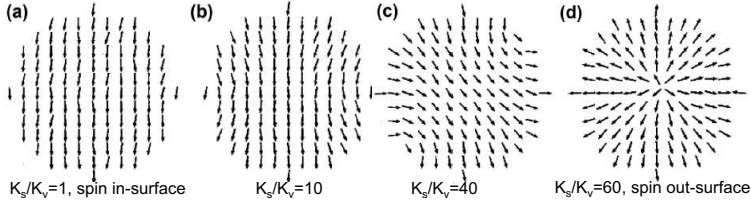
Figure 2.4: Spin structure from Monte-Carlo simulation of FePt NPs. The spin structures are collinear along the in-plane direction, when the ratio of surface anisotropy to volume anisotropy is equal. As the surface anisotropy becomes larger than the volume anisotropy, spins are canted away from the in-plane direction and tend to lie outward or inward. Taken from Ref [54].

The surface anisotropy can exert a strong influence on the magnetic structure of magnetic nanoparticles. In sufficiently small particles, there is a sharp cross-over from a throttled spin structure, where the core spins are parallel to each other and where the outermost spins tend to lie normal to the surface, forming a hedgehog structure where all the spins are radially oriented either inward or outward, giving a net magnetization close to zero.

2.4.4 Strain anisotropy

Strain anisotropy arises from the strain dependence of the anisotropy constants. It is often interpreted by the magnetostriction effect, which is a change in the material's physical dimensions as a result of the change in orientation of the magnetization. Usually, the relative deformation is very small, in the order of 10^{-5} to 10^{-6} [55]. An uniaxial stress can produce an unique easy axis of magnetization, if the stress is sufficient to overcome all the other anisotropies. The magnitude of the strain anisotropy is often described by two empirical constants, known as the magnetostriction constants, (λ_{111} and λ_{100}), and the magnitude of stress σ. For example, in a cubic system, the magnetostriction constant along [110] can be a linear combination of λ_{111} and λ_{100}. For an isotropic magnetostriction (i.e. in iron oxide NP), $\lambda_{111} = \lambda_{100} = \lambda$ [56].

The way in which a material responds to stress depends on its saturation magnetostriction λ_s. For this analysis, the compressive stress σ is considered as negative, whereas the tensile stress is positive.

In the case of a single stress σ acting on a single magnetic domain, the magnetic strain anisotropy energy E can be expressed as

$$E = \frac{3}{2}\lambda_s \sigma sin^2\theta \qquad (2.22)$$

where θ is the angle between the measured magnetic moment and the σ-axis. The effect of stress on the isotropic sample depends on the sign of the $\sigma\lambda_S$ product.
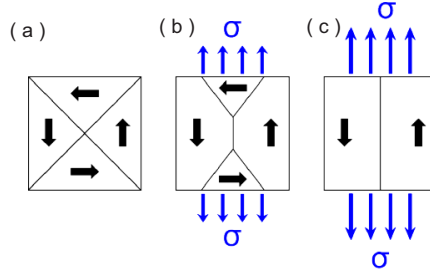
Figure 2.5: (a) A ferromagnetic body with 90 degree domains. (b) Tensile strain decreases the magnetic moments in domains perpendicular to the stress direction. (c) Higher stress leaves only magnetic moments parallel to the stress direction.

Stress applied to a multi-domain ferromagnetic body will affect the orientation of magnetization through magnetostriction [57]. An example of the stress on the magnetization reversal of a Ni sample is given in the Figure 2.5. Hereby, the $\sigma\lambda_S$ is positive for Ni. The application of tensile stress causes the domains with magnetic moments perpendicular to the stress to dwindle, as shown in Figure 2.5(b). As the strength of the tensile stress increases, the domains perpendicular to the stress vanish and leave only the magnetic moments parallel to the stress. If compressive stress was applied instead, the vertical domains would disappear accordingly. In the Ni samples, the stress of 6.4×10^6 Pa causes stress anisotropy to be roughly equal to the magnetocrystalline anisotropy [57].

Overall, if $\sigma\lambda_s$ is negative, the perpendicular alignment of magnetization with respect to the σ-axis is favored; on the other hand, when $\sigma\lambda_s$ is positive, the parallel alignment is preferred.

2.5   Superparamagnetism

Superparamagnetism describes a form of magnetism, which appears in small ferromagnetic or ferrimagnetic nanoparticles.

Formation of domain walls in ferromagnetic materials is determined by the competition between the energy cost for domain wall formation E_{DW} and the energy reduction of the magnetostatic energy E_{MS}. By assuming spherical particles with the radius r, the volume energy of the magnetostatic energy is given by

$$E_{MS} = \frac{1}{2}\mu_0 N M_s^2 V = \frac{2}{3}\pi\mu_0 N M_s^2 r^3 \tag{2.23}$$

where μ_0 is the vacuum permeability, $N = \frac{4\pi}{3}$ for a sphere is the demagnetizing factor, M_s is the saturation magnetization and V is the volume of the particle. It can be seen that the magnetostatic energy is proportional to the volume or the cube of the diameter of the particle.

Domains are separated by domain walls. Domain walls have finite widths, because there is a competition between the anisotropy and the exchange interaction. The energy of a domain wall can be expressed as

$$E_{DW} = \pi^2 r^2 \sqrt{AK} \qquad (2.24)$$

where A, being proportional to J, is called the exchange constant, and K is the uniaxial anisotropy constant. The domain wall energy is proportional to the surface area or the square of the radius. For a particle, as the radius is decreased, the magnetostatic energy drops. It can be expected that below a critical radius, E_{MS} is smaller than E_{DW}. A single domain state is preferred in the particles; the evolution of the domain states in the particles can be seen in Figure 2.6.
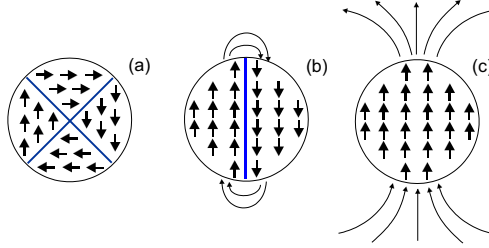

Figure 2.6: Schematic pictures of a spherical particle in (a) four domain state and zero magnetostatic energy (b) two domain state and low magnetostatic energy (c) single domain state and large magnetostatic energy. Taken from Ref [58].

The critical radius r_c can be derived from the comparison of the two energy terms of E_{MS} and E_{DW},

$$r_c = \frac{9\pi\sqrt{AK}}{\mu_0 M_s^2} \qquad (2.25)$$

Example values for the critical radius of single domain nanoparticles are given in Table 2.1 below.

Table 2.1: Critical radius of some materials. The values are obtained at room temperature. Values of Fe and Ni are uniaxial estimates. Taken from [59].

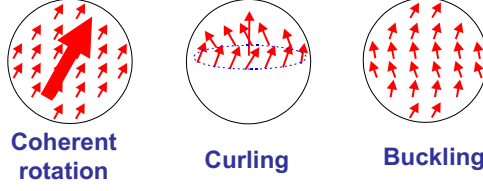| Material	$\mu_0 M_s$(T)	A (pJm^{-1})	K_1(MJm^{-3})	r_c (nm)
Fe	2.15	8.3	0.05	6
Co	1.76	10.3	0.53	34
Ni	0.61	3.4	-0.005	16
Fe_3O_4	0.6	12	0.013	50

Figure 2.7: Several possibilities for magnetization reversal in the case of a single-domain nanoparticle. The case of coherent rotation can be considered as the super-spin case. Taken from [58].

The magnetization reversal in such a single-domain nanoparticles can occur via different modes, as shown in Figure 2.7.

For coherent rotation, all moments rotate in unison while pointing always in the same direction. The spins in a single-domain NP reverse in coherent rotation mode can be regarded as a superspin.

The superspins in an applied field can be described using the Stoner-Wohlfarth model. The model, composed of anisotropy, shape anisotropy and Zeeman energy, is read as:

$$E = K_1 V sin^2\phi + \frac{1}{2}(N_\perp - N_\parallel)\mu_0 M_s^2 V sin^2\psi - \mu_0 H M_s V cos(\theta - \phi) \qquad (2.26)$$

The first item is the magnetocrystalline anisotropy and the second is the shape anisotropy, which can be simplified into an effective anisotropy $KV sin^2\psi$. K is the density of effective anisotropy energy and ψ is the angle between the superspin moment and the axis of effective anisotropy. The last item is the Zeeman energy. The angles and anisotropy axis are depicted in Figure 2.8. At zero field, the energy has two minimum values for $\phi = 0$ and π separated by an energy barrier of KV. The energy barrier changes after applying a magnetic field H; in order to figure out the magnetization reversal in a field, the field can be expressed as a dimensionless parameter.

$$h = \frac{\mu_0 M_s H}{2KV} \qquad (2.27)$$

If $KV \gg k_B T$, the superspin of the particle is stable, fixed at the easy axis and not able to overcome the barrier. As a consequence, the particle shows stable FM or FiM properties. However, if $KV \sim k_B T$, the thermal energy will lead to fluctuations of the superspins, and a statistic reversal of the moment between the two easy directions can be detected during a measurement. This stochastic switching behavior defines a "superparamagnetic" (SPM) system [58].

The frequency f or the characteristic time scale τ of the fluctuation is decided by the measurement time and follows an Arrhenius type of activation law, known as the Néel-Brown model. The random flipping of the superspin is induced by thermal energy. The average time τ to perform such a flip is given by

$$\tau = \tau_0 \exp\left(\frac{\Delta E}{k_B T}\right) \qquad (2.28)$$
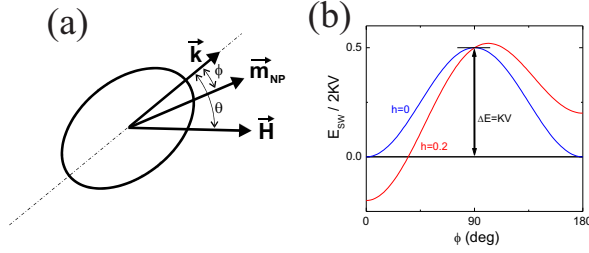
Figure 2.8: (a)A prolate shaped particle for the Stoner-Wholfarth model, with the anisotropy superspin $\vec{m}_{NP}$, effective anisotropy constant $\vec{k}$ and applied magnetic field $\vec{H}$. (b)The plot of $E_{SW}/2KV$ as a function of ϕ for h = 0 (blue) and h = 0.2 (red) when $\theta = 0$, where E_{SW} is the free energy of the NPs. Taken from [58].

where $\tau_0 \sim 10^{-9}$s is the relaxation time of the atomic spins. τ is highly temperature dependent and shows a large time span. At high temperature, when τ is smaller than τ_m at high temperatures, the magnetic moments will rapidly fluctuate, the measurement observes only a fluctuating state. On the other hand, at low temperature, when τ is larger than the measurement time τ_m, the particles will appear 'blocked', leading to a well defined state which is called the blocked state. This is known as the superparamagnetic state. It is clear that there is a characteristic crossover temperature, where the relaxation timescale meets the probing one. This characteristic crossover temperature is called the blocking temperature, T_B.

$$T_B = \frac{\Delta E}{k_B ln(\tau_m/\tau_0)} \tag{2.29}$$

For example, a particle with a barrier height of $KV/k_B = 315$ K shows a relaxation time of $\tau \approx 10^{-9}$ s at 300 K and $\approx 10^{+18}$ s at 5 K. However, for our magnetic measurements, the typical time scales are in the range of 10^2 s. There will be normally a T_B between 300 K and 5 K. Below T_B, the particles will appear in a blocked state, while there show the superparamagnetic state above T_B.

Important consequences for the magnetic behavior of SPM systems can be best seen in the so-called ZFC and FC curves, as shown in Figure 2.9. Starting from 300 K, the samples are first cooled in zero field, down to 5 K. Subsequently, a constant field of 4 mT is applied and the ZFC curve is recorded upon warming up to 50 K. At the same applied field, the sample is then cooled to 5 K and the FC curve is recorded.

2.6 Iron oxides

There are, in total, 16 different kinds of iron oxides in nature and laboratory [60]. However, out of all the oxides, only four are widely investigated and used, which are Wüstite, Magnetite, Maghemite and Hematite. Their structures and magnetic properties will be discussed below.
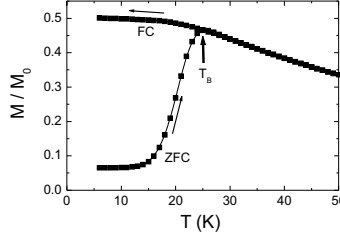
Figure 2.9: Magnetization curves, measured as zero field cooling (ZFC), followed by field cooling (FC), from the Monte-Carlo simulations of an ensemble of non-interacting superparamagnetic particles with $KV/k_B = 315$ K at a magnetic field of 4 mT. The arrow indicates the blocking temperature T_B. Taken from [58].

2.6.1 Wüstite, Fe_xO

Wüstite (Fe_xO) is a gray-colored mineral form of iron oxide, which is found in meteorites and native iron. Fe_xO is unstable below 840 K at atmospheric pressure. It can be quenched to room temperature, leading to a metastable state [61, 62]. Fe_xO contains Fe^{2+} ions and mostly, Fe_xO is non-stoichiometric. The composition of x varies from 0.84 to 0.95 depending on the temperature and pressure [60].

Wüstite has a similar crystallographic structure as rock salt ($Fd\bar{3}m$), which is visualized in Figure 2.10(a). The lattice d-spacing varies from 4.28Å to 4.31Å, depending on the stoichiometry. In its unit cell, oxygen atoms occupy the main face-centered cubic (FCC) sites and the Fe^{2+} cations fill the octahedral interstitial sites. Both the cations and anions are arranged in a cubic close packed structure. The presence of many vacancies in its structure causes a high mobility of Fe^{2+} cations towards the surface and they will be oxidized to Fe^{3+}. This means wüstite is a thermodynamically unstable phase in bulk and tends to fully oxidize to magnetite when exposed to air.
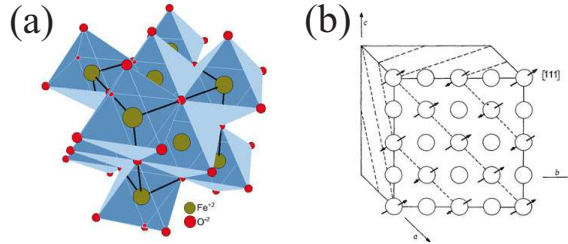

Figure 2.10: (a)Wüstite crystal structure, Fe^{2+} is represented as yellow dots while O^{2-} as red dots. (b)Magnetic structure of wüstite. Taken from Ref. [63] and Ref. [64], respectively.

Wüstite shows antiferromagnetism below T_N. The T_N of Wüstite varies from 190 K to 211 K, depending on the different stoichiometry [60]. Below T_N, the spins

in [111] planes point in the same direction shown in Figure 2.10(b). The spins in this layer are in the FM order, while the spins in the adjacent layer are oriented in the opposite direction, leading to antiferromagnetism in the system. Wüstite becomes PM above T_N [60, 64].

2.6.2 Magnetite, Fe_3O_4

Magnetite (Fe_3O_4) is a black, FiM material, known as loadstone, and it is found in rocks and living organisms. Fe_3O_4 is the most common mineral of all iron oxides [65].

Fe_3O_4 has has a spinel structure with the space group Fd3m. The lattice parameter is $a = 8.397$Å. Both Fe^{2+} and Fe^{3+} ions are present in each unit cell, moreover, where 32 O^{2-} ions are regularly cubic packed along the [111] direction. Fe_3O_4 is sometimes represented as $FeO \cdot Fe_2O_3$.

The formula can be written in the general formula for a common spinel structure as $A^{2+}[B_2^{3+}]O_4^{2-}$, where A represents the tetrahedral site with divalent ions and B the octahedral site with trivalent ions. However, the situation in Fe_3O_4 is opposite to the conventional case: the divalent ions sit on the octahedral sites (B sites) while the trivalent ions are equally distributed at the octahedral (B) and tetrahedral (A) sites. That means, all of the tetrahedral sites and half the octahedral sites are occupied by Fe^{3+} and the other half of the octahedral sites are occupied by Fe^{2+}. In total, in one unit cell, 8 Fe^{3+} sit at the tetrahedral sites while the other 8 Fe^{3+} together with the 8 Fe^{2+} sit at the octahedral sites, which can be visualized in Figure 2.11(a). A magnified view of the two kinds of sublattices is shown in (b). Hence, the formula can be written as $Fe_8^{3+}[Fe_8^{2+} Fe_8^{3+}]O_{32}^{-2}$.

In one unit cell, 8 Fe^{2+} ions sit in the octahedral sites and align in an FM order with respect to the 8 Fe^{3+} sitting in the octahedral sites due to the double exchange interaction. The other 8 Fe^{3+} ions distribute in a tetrahedral structure and align in an AFM order with respect to the 8 Fe^{3+} at the octahedral sites. As a consequence, the spins of the Fe^{3+} from both sites are cancelled out and only the spins of Fe^{2+} contribute to the total magnetic moment. The total spin $S_{Fe^{2+}} = 4/2$ gives a magnetic moment of 4 μ_B, which is close to the experimental value of 4.1 μ_B. The saturation magnetization of magnetite is 480 KA/m.

Fe_3O_4 is an interesting candidate for fundamental and applied magnetism studies due to its rich magnetic states, i.e. the Curie temperature (T_C) at 850 K and a Verwey transition temperature (T_V) at 120 K (a transition between metal and semiconductor). Also, many useful properties of Fe_3O_4 have been reported; for example, Fe_3O_4 shows both metallic and FM properties in the temperature range of 850 K to 120 K; it has a conductivity in the order of $10^2 - 10^3 \Omega^{-1}m^{-1}$.

2.6.3 Maghemite, γ-Fe_2O_3

Maghemite (γ-Fe_2O_3) is a reddish-brown FiM mineral at room temperature. Similar to magnetite, maghemite has a spinel crystal structure with a space group of $Fd\overline{3}m$, which is shown in Figure 2.12(a). It also has an inverse spinel unit cell, with a lattice
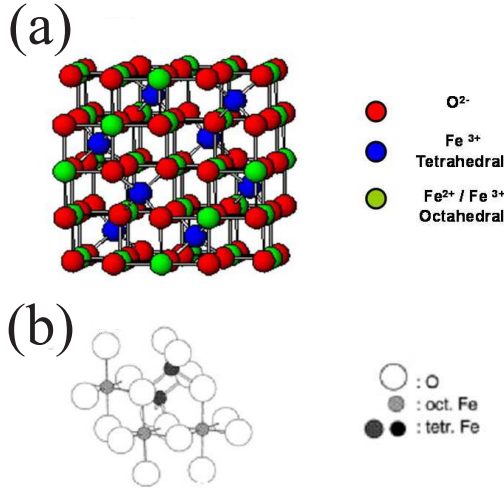
Figure 2.11: Magnetite crystal structure; (a) Unit cell reproduced by the ball and stick model; red balls represent the O^{2-} ions, blue balls represent the Fe^{3+} ions sitting on the tetrahedral sites and green balls represent the Fe^{3+} or Fe^{2+} ions sitting on the octahedral sites (b) Magnified view of 3 octahedral and 3 tetrahedral arrangement. Taken from Ref. [64].

spacing a of 8.33Å. The unit cell consists of tetrahedral and octahedral sublattices. 32 O^{2-} ions are regularly cubic packed in both sublattices, 8 Fe^{3+} ions occupy the tetrahedral sites; but, out of the 16 octahedral sites, only 12 are occupied by Fe^{3+} ions, while the rest 4 sites consist of $2\frac{2}{3}$ vacancies and $1\frac{1}{3}Fe^{3+}$. Therefore, the formula of the unit cell can be described as $Fe_8^{3+}[Fe_{12}^{3+} \otimes_{2\frac{2}{3}}^{3+} Fe_{1\frac{1}{3}}^{3+}]O_{32}^{2-}$, where $\otimes$ means one vacancy. A magnified view of the surroundings of Fe^{3+} at octahedral sites is shown in Figure 2.12(b).

Since maghemite is almost of the same crystal structure as magnetite, it is difficult to distinguish them by crystal structures via x-ray diffraction. Fortunately, magnetic or transport measurements are helpful to tell the differences between them.

In each unit cell, spins of 8 Fe^{3+} ions at octahedral sites are cancelled out by the same number of Fe^{3+} at tetrahedral sites, due to the antiparallel alignment of the spins in both sites. As a consequence, some remnant Fe^{3+} ions at the octahedral sites lead to a net magnetic moment. The value of remnant moment $S_{Fe^{2+}} = 2.5 \, \mu_B$ is quite close to the experimental value of 2.36 μ_B. Moreover, γ-Fe_2O_3 shows a T_C of 820 K, but it is difficult to observe the transition because it is converted to α-Fe_2O_3 above 700 K. γ-Fe_2O_3 is an insulator.
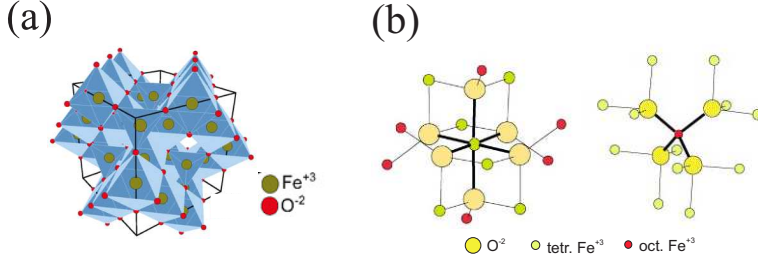
Figure 2.12: (a) Maghemite crystal structure with the space group of $Fd\bar{3}m$ cubic lattice. The red balls represent Fe^{3+} while the yellow balls represent O^{2-}. (b) Magnified model of the surroundings of Fe^{3+} at tetrahedral and octahedral sites. (a) and (b) are taken from Ref. [66] and Ref. [67], respectively.

2.6.4 Hematite, α-Fe_2O_3

Hematite (α-Fe_2O_3) is a blood red AFM mineral. It is one of the most abundant minerals in rocks. It has a hexagonal unit cell with lattice constants $a = b = 5.34$ Å and $c = 13.75$ Å. O^{2-} ions are stacked in hexagonal close packed (HCP) arrays along the [100] direction while two-thirds of the sites are filled with Fe^{3+} ions.

Hematite shows PM behavior above 956 K. In the temperature range between 956 K and 263 K, it shows weak FM and it becomes AFM below 263 K. Hematite is an insulator.

At last, some significant properties of iron oxides discussed before are included in the Table 2.2 for comparison.

Table 2.2: Some parameters of iron oxides. Taken from [65].

Iron Oxides	Crystalline	Magnetic behavior	Electric behavior	Saturation Magnetization (kA/m)	Anisotropy Constant J/m^3	Magneto-restriction constant
Wüstite	FCC	T_N(198K)	Insulator	-	-	-
Magnetite	Inverse spinel	T_C(850K)	Insulator	480	-1.35×10^4	8×10^{-6}
Maghemite	Inverse spinel	T_C (820K)	T_V(122K)	380	-4.65×10^3	3.5×10^{-5}
Hematite	HCP	T_C (956K)	Insulator	2.5	1.26×10^6(c)	3.5×10^{-5}

2.7 Ferroelectric and magnetoelectric materials

2.7.1 Piezoelectric and ferroelectric materials

Piezoelectricity is a property which exhibits electric charge accumulation in response to applied mechanical stress (see Figure 2.13(a)). The piezoelectric (PE) effect is a reversible process in PE materials, with the direct PE effect (the internal accumulation of electrical charge resulting from applied mechanical stress) and the converse

PE effect (the internal generation of mechanical strain resulting from an applied electrical field) [68].
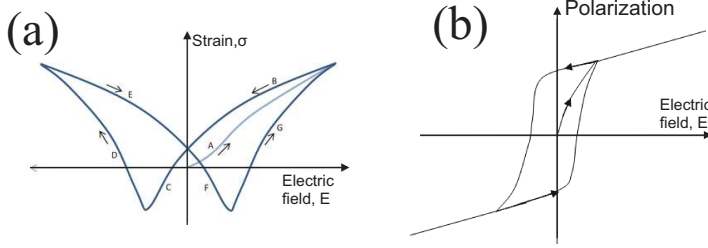

Figure 2.13: (a) Typical piezoelectric hysteresis loop for a piezoelectric material (b) Typical ferroelectric hysteresis loop for a ferroelectric material. Figure (a) is adopted from [69].

For some piezoelectric materials, they exhibit spontaneous electric polarization, and the polarization can be reversed by an external electric field. This property is called ferroelectricity. The most straightforward method to measure the reversal process is the ferroelectric (FE) hysteresis loop, which is shown in Figure 2.13(b).
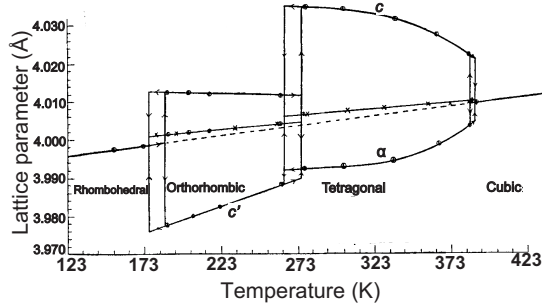
Figure 2.14: Temperature dependent lattice parameters of BTO single crystals. Taken from [70].

Barium titanate (BTO) is a typical FE material, which has received wide interest since the 1940s [71]. Single crystal BTO exhibits three distinct structural phase transitions with decreasing temperature: cubic-to-tetragonal (C $\rightarrow$ T) at a temperature of $T \approx 393$ K, tetragonal-to-orthorhombic (T $\rightarrow$ O) at $T \approx 278$ K and orthorhombic-to-rhombohedral (O $\rightarrow$ R) at $T \approx 190$ K, respectively. C phase is the paraelectric phase while the other three phases are ferroelectric phases. The detailed information about the lattice parameters at each phase can be seen in Figure 2.14 [70].

Density functional theory calculations provide the interpretation of the ferroelectricity origin of BTO [72]. The barium ions occupy the corners of the cubic lattice, the oxygen ions the face centers and the titanium ions the body center, as displayed

in figure 2.15(a). Below 393 K, the lattice becomes tetragonal: One of the axes (usually taken to be the *c*-axis) becomes lengthened and the other two axes shortened. The FE polarization is created by the shift of the positive transition metal ion Ti^{4+} away from the center of the negatively charged oxygens. This leads to a net dipole moment of 26μ C/cm^2 per unit [73]. The macroscopic electric polarization can be induced when such a dipole moment occurs coherently in the neighboring unit cells. The polarization dependence of the electric field for a (100) oriented BTO single crystal is shown in Figure 2.15(b).
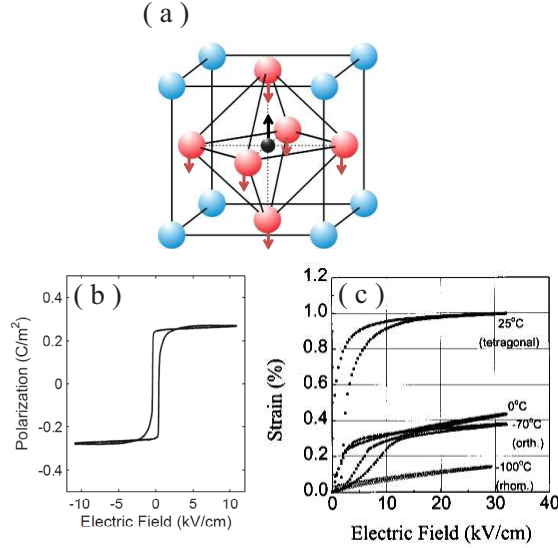
Figure 2.15: (a) The unit cell of BTO perovskite structure; the blue balls represent barium, pink balls oxygen and a black ball titanium. The arrow indicates the shift of titanium ion with respect to the oxygen octahedra, leading to a spontaneous electric polarization. (b) Polarization vs. electric field for a BTO single crystal under the electric field amplitude of ±10 kV/cm at room temperature. (c) Strain vs. electric field for (001) oriented BTO single crystal with input amplitude of ±40 kV/cm at different phases. FE loops are taken from Ref. [74] and PE loops are taken from Ref. [75].

Although all FE materials have piezoelectric properties, BTO is widely used as a PE material in applications. Strong alternating electric fields cause strain effects of substantial magnitude. The strain vs. electric field plot for a (001)-oriented BTO single crystal is shown in Figure 2.15(c). It shows a PE curve as a "butterfly" loop in the T phase while the strain becomes linearly dependent on the electric field, as temperature decreases to R phase, and the induced strain strength decreases. Caspari and Merz reported that the nature of the strain effects in BTO single crystals is a combination of linear piezoelectricity and domain switching effects [76].

2.7.2 Magnetoelectric systems

Magnetoelectric (ME) materials are systems where the magnetization can be manipulated by electric field or the polarization can be tuned by magnetic field. The coupling may arise directly between two order parameters or indirectly via strain. The magnetoelectric effect can be established in the form of electric polarization as a function of the magnetic field $P_i(H_j)$ or magnetization as a function of the electric field $M_i(E_j)$.

$$P_i = \alpha_{ij}H_j + \frac{\beta_{ijk}}{2}H_jH_K + \cdots \tag{2.30}$$

$$\mu_0 M_i = \alpha_{ij}E_j + \frac{\gamma_{ijk}}{2}E_jE_K + \cdots \tag{2.31}$$

where E and H are the electric and magnetic fields, and α and β are the linear and nonlinear ME susceptibilities. The effect can be observed in both single phase ME materials and artificial ME heterostructures.

The single-phase ME materials can be classified into three different classes, depending on the microscopic mechanism of ferroelectricity, namely i) hybridization effects, such as $BiFeO_3$. ii) Geometric constraints, such as $YMnO_3$, and iii) electronic degrees of freedom (spin, charge or orbital), such as $TbMnO_3$ and $LuFe_2O_4$. The MEC effect in single-phase ME materials is induced by intrinsic mechanisms [77, 78].

However, single-phase ME materials are very rare and their ME coefficients are usually too low to be used in applications. In order to overcome the shortages of single-phase ME materials and provide new ME coupling (MEC) mechanisms, more and more research interests have been moved to artificial ME materials in the last decades.

Remarkable MEC effects in artificial ME materials were reported [2, 79, 80]. The MEC effect can be ascribed to the following two mechanisms: i) Direct coupling, MEC owing to an interfacial electronic effect. This type of mechanism has been theoretically predicted based on bond-reconfigurations driven by ionic displacement or spin dependent screening mechanisms [4, 81, 82]. ii) Indirect coupling, MEC mediated by strain. It means that the magnetization manipulation by the electric field or the electric polarization manipulation by the magnetic field between the two phases is mediated via strain. This MEC effect has been evidenced in various thin film systems [3, 6]. The MEC effect in artificial ME composites is induced by extrinsic mechanisms.

2.8   Scattering methods

Scattering is widely used as a non-destructive technique to study the structural and excitation information in condensed matter physics. Depending on method, various structural information can be obtained. For instance, X-ray scattering is usually used as a method to provide the crystal structure while the magnetic structure can be complemented using neutron scattering. The basic knowledge of general

scattering and, especially, reflectometry theory is introduced in this section. For a complete understanding of the scattering theory, please see Ref. [83].

2.8.1   Basics of scattering methods

In my thesis, only elastic scattering is considered. A schematic sketch of the elastic scattering experiment is displayed in Figure 2.16.
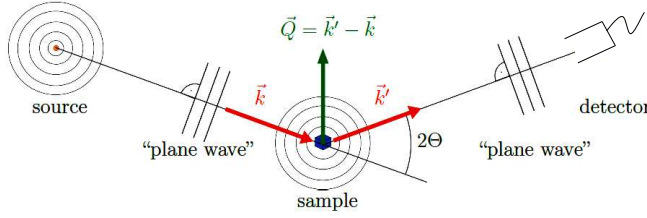

Figure 2.16: The sketch of a scattering experiment in the Fraunhofer approximation. Taken from Ref. [83].

The incident wave is produced by a monochromatic source and can be described by a plane wave under the Fraunhofer approximation. The same applies for the scattered beam. The incident and scattered beam can be fully described by the wave vectors $\vec{k}$ and $\vec{k}'$, respectively. For elastic scattering, $k = |\vec{k}| = |\vec{k}'| = \frac{2\pi}{\lambda}$, where λ is the wavelength of the neutron source. Hence, the so-called scattering vector can be defined as

$$\vec{Q} = \vec{k}' - \vec{k} \tag{2.32}$$

with

$$|\vec{Q}| = \frac{4\pi}{\lambda} sin\theta \tag{2.33}$$

In a scattering experiment, the intensity $I(\vec{Q})$ is measured as a function of the scattering vector $\vec{Q}$. The scattered intensity is observed by the detector, which covers the solid angle $d\Omega = dS/r^2$ with the area dS of the detector and its distance r to the sample. The position of the detector is determined by the angles Θ and Φ, as displayed in Figure 2.17. The measured intensity from the detector is proportional to the so-called scattering cross-section, which is corresponding to the probability for an interaction of the incident beam with the sample. The sketch to define the scattering cross-section can be seen in Figure 2.17.

If N particles being scattered per second into a solid angle $d\Omega$ is seen by the detector under a scattering angle 2θ, and the energy E is kept the same, then the so-called differential cross-section can be defined by

$$\frac{d\sigma}{d\Omega} = \int_0^\infty \frac{d^2\sigma}{d\Omega dE} dE \tag{2.34}$$
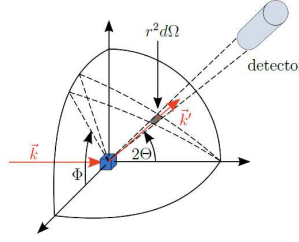
Figure 2.17: Geometry to derive the scattering cross-section. Taken from Ref. [83].

The differential scattering cross-section is proportional to the probability that a particle is scattered into the solid angle $d\Omega$ by the interaction with the sample. The relationship between the arrangement of the atoms in the sample and the scattering cross-section $d\sigma/d\Omega$ is simplified using the so-called Born approximation, which is also known as the kinematic scattering approximation.

In quantum mechanism, the probability to find a particle in the volume of d^3r is given by the absolute square of the probability amplitude; hence, the differential scattering cross-section, which is defined as the angular dependent scattering probability, can be expressed as $|f(\vec{Q})|^2$, which reads as

$$\left(\frac{d\sigma}{d\Omega}\right) = |f(\vec{Q})|^2 = \frac{m^2}{4\pi^2\hbar^4}\left|\int V(\vec{r'})e^{i\vec{Q}\vec{r'}}d^3\vec{r'}\right|^2 \tag{2.35}$$

where $\vec{r}$ is the sample to detector distance and $V(\vec{r})$ is the interaction potential of neutrons.

2.8.2 Bragg scattering

X-rays and moderated neutrons are widely used to investigate the crystal structures, since the wavelengths of both beams are in the same range of the lattice distances. A plane wave with a wavelength λ scattered on an atomic periodical structure in constructive interference yields Bragg reflections. The conditions for constructive interference are described by the so-called Bragg law:

$$n \cdot \lambda = 2d \cdot sin\theta \tag{2.36}$$

d is the interplanar spacing and θ is the scattering angle. The equivalence of the Bragg law and the Laue condition stems from the relationship between real space and reciprocal space.

2.8.3 Grazing incidence scattering - Reflectometry

In reflectometry measurements, the scattering vector $\vec{Q} = \vec{k'}$ - $\vec{k}$ is close to 0, resulting in nearly no sensitivity to the atomic structures, which means no crystallographic Bragg scattering is visible. Instead, reflectometry measures the in-depth

profile of the scattering potentials. Depending on different types of beams, nuclear or magnetic scattering length density (nSLD or mSLD) can be obtained. In the reflectometry setup, a monochromatic, collimated beam impinges upon the sample under a well-defined angle $\alpha_i = \theta$ (usually $\ll 5^o$). Most of the beam scattered at the sample is reflected by the sample within a so-called specular scattering. The incoming angle α_i and outgoing angle α_f are always kept the same, leading to the scattering vector $\vec{Q}$ being always perpendicular to the sample surface. The beams are reflected from different interfaces, so that constructive and destructive interference of beams reflected from the two interfaces are displayed as peaks, the so-called Kiessig fringes. The layer thickness information is included in the peaks. Furthermore, lateral correlations can be probed in the so-called off-specular or diffuse scattering at angles $\alpha_i \neq \alpha_f$.

In contrast to the diffraction experiment, the Born approximation is no longer valid for reflectometry measurements, because multiple scattering in the reflection mode cannot be neglected [84]. Since the Q region covered by reflectivity measurements is not sensitive to the atomic periodical structure, it is possible to describe the scattering potential within the continuum approximation. $\vec{Q}$ is always perpendicular to the surface; the scattering potential of the sample can be simplified only in the z component $V(z)$. In the thickness direction, the beam is partly transmitted to the substrate and partly reflected. The reflection (transmission) coefficients is defined as the modulus squared of the ratio of the amplitudes of reflected (transmitted) and incoming waves. They are represented by R and T and expressed by the Fresnel equations:

$$R = \left|\frac{\theta - n\theta_t}{\theta + n\theta_t}\right|^2 \tag{2.37}$$

$$T = \left|\frac{2\theta}{\theta + n\theta_t}\right|^2 \tag{2.38}$$

θ_t is the transmission angle of the beam, $n = 1 - \delta + i\beta$ is the index of refraction, shown in Figure 2.18. Depending on the different types of materials and beams, the values of the scattering power δ and absorption β will be determined.

For most materials, the refractive index n is smaller than 1, which leads to a total reflection in the sample. The total reflection means that during the reflectom-
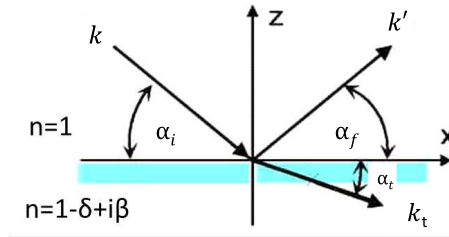
Figure 2.18: Typical geometry of reflectometry under the grazing incident angle θ.

etry process, when the incident angle is smaller than the critical angle θ_c, all the beam are reflected and no beam transmitted into the sample. Hence, the intensity dependence of Q shows a plateau during the total reflection process. When the incident angle above the θ_C, the intensity drops as $|Q|^4$, assuming a perfect smooth surface without further layer structures. Roughness will additionally speed up the intensity decrease, which can be described by the Debye-Waller model, multiplying $I(Q) \sim e^{Q_z^2 \sigma^2}$ with the roughness σ of the surface. For a multilayer system, e.g. a thin film on a substrate, an iterative formalism, describing the scattering process using the reflection and transmission coefficients in each material, is introduced in Ref.[85].

Polarized neutron reflectometry (PNR)

For magnetic materials, the unpaired electrons inside the atoms will show a magnetic moment and will additionally generate a magnetic induction field $\vec{B}$. Fortunately, the neutron is a particle with 1/2 spin; by using neutrons as the beam, one can probe the magnetic structure of the matter, besides the nuclear structure. The interaction potential for neutrons can be averaged from the Fermi-pseudo-potential to:

$$V(Z) = \frac{2\pi\hbar^2}{m_N}\rho_N b - \gamma_n \mu_N \vec{\sigma} \cdot \vec{B} \tag{2.39}$$

The first item is the nuclear potential, while the second one is the magnetic potential. m_N is the mass of neutron, ρ_N is the nuclear density and b is the scattering length. $\vec{\sigma} = (\sigma_x, \sigma_y, \sigma_z)$ is the vector of Pauli-matrices. The gyromagnetic factor $\gamma_n = -1.913$ and the nuclear magneton $\mu_N = 5 \cdot 10^{-27}$ J/T are two constant coefficients. With this interaction potential, the differential magnetic scattering cross-section can be described as

$$\frac{d\sigma}{d\Omega} = (\gamma_n r_e)^2 \frac{1}{2\mu_B}|\langle \sigma'_z|\vec{\sigma} \cdot \vec{M}_\perp(\vec{Q})|\sigma_z\rangle|^2 \tag{2.40}$$

where r_e is the radius of electron and σ_z is the spin projection along a quantization axis given by the external field. $\vec{M}_\perp = \widehat{Q} \times \vec{M} \times \widehat{Q}$ is the Fourier transformation of the magnetization component of the sample, which is perpendicular to the scattering vector $\vec{Q}$. The equation tells us that only the in-plane magnetization component, which is perpendicular to the $\vec{Q}$, can be measured. The typical geometry of a PNR experiment at the sample position is shown in Figure 2.20. The magnetic induction $\vec{B}_0 = \mu_0 \vec{H}$ is constant over the sample and gives a constant contribution to the index of refraction.

Hence, this contribution cancels out for the calculation of refraction and transmission. Depending on the neutron beam polarization before and after the sample, one can define four channels, namely R_{++}, R_{--}, R_{+-} and R_{-+}. The former two are called non-spin-flip channels and the neutron spin direction is not changed after it is scattered at the sample, while the later two are called spin-flip channels. The polarized neutron beam can be described by plane waves with two spin components $\psi_+(\vec{r})$ and $\psi_-(\vec{r})$, for polarization "up" and "down". The Schrödinger equations for
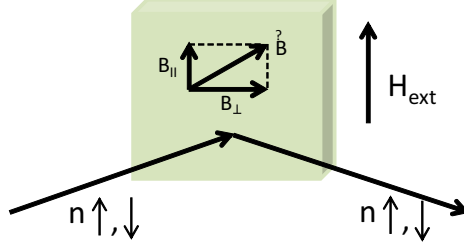
Figure 2.19: The geometry of PNR experiment at the sample position. Neutrons are polarized, either parallel or antiparallel to the external magnetic field H_{ext}. The magnetic signal in samples are induced by the external magnetic field, leading to a magnetic induction of $B = \mu_0(H_{ext} + M))$, while $\vec{B}_{||}$ and $\vec{B}_{\perp}$ are two projections of $\vec{B}$ with respect to H_{ext}.

the potential of neutron state can be simplified as coupled equation as

$$\psi_+''(z) + [k_z^2 - 4\pi b\rho_N + \frac{2m\gamma_n\mu_n}{\hbar^2}B_{||}]\psi_+(z) + \frac{2m\gamma_n\mu_n}{\hbar^2}B_{\perp}\psi_-(z) = 0 \qquad (2.41)$$

$$\psi_-''(z) + [k_z^2 - 4\pi b\rho_N - \frac{2m\gamma_n\mu_n}{\hbar^2}B_{||}]\psi_-(z) + \frac{2m\gamma_n\mu_n}{\hbar^2}B_{\perp}\psi_+(z) = 0 \qquad (2.42)$$

In the R_{++} channel, the contribution of the potential comes from the magnetic scattering added with nuclear scattering, while they are subtracted in the R_{--} channel. The contribution from the spin flip channel is the magnetization of the $B_{\perp}$ component.

Reflectivity data reduction
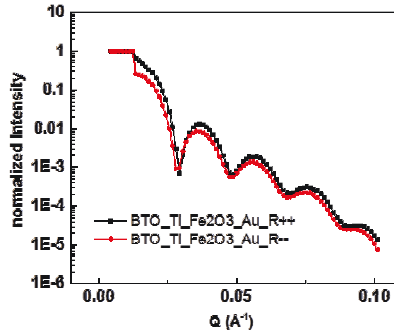
Figure 2.20: PNR simulation of the sample (substrate) BTO/(7 nm) Ti/(22 nm) Fe$_2$O$_3$/(25 nm) Au by GenX, the R_{++} and R_{--} channels are simulated together with the reference value of every parameter of every component layer.

The XRR and PNR data are analyzed by fitting the reflectivity curve using the Parratt formalism [85] within the framework of the program "GenX" [86]. The fitting result yields a structural model for the investigated sample.

In XRR reflexivity, a structural model is used for the sample, which usually consists of the ambient environment, the substrate and the layers. Several parameters are used to describe the substrate and layers, for example, the stoichiometry of the material, the layer thickness, roughness and nSLD. The simulated X-ray reflexivity of the sample can be implemented by the structural parameters. The fitting procedure will give the best representation of the raw data, by modifying the open parameters. For PNR measurements, a magnetic profile needs to be added besides the structural model, which is mainly represented by mSLD. In PNR simulation, the R_{++} and R_{--} channels are simulated at the same time by the combination of the nuclear and magnetic scattering length density (SLD).

In our simulation, different models are used for finding the best fitting of our measured results, which are illustrated in Chapter 4. For evaluating the goodness of the fit, the Figure of Merit (FOM) is used to calculate the average of the absolute difference between the logarithms of the data Y_Q and the fitting S_Q:

$$FOM_{log} = \frac{1}{N-1} \cdot \sum_Q |lgY_Q - lgS_Q| \qquad (2.43)$$

Chapter 3

Methods and Instruments

In this chapter, the instruments and methods for the sample preparation and investigation used in the thesis are briefly introduced. Also, the colloidal self-assembly methods are described.

3.1　NP self-assembly methods

The NP preparation and assembly methods can be divided into two groups depending on the growth strategy [87, 88]. To the first group belong the top-down methods. Materials start from large structure sizes and end up with small structures via several methods. These methods include deposition techniques, such as sputtering evaporation and laser ablation.

The other group consists of bottom-up methods. Nanostructure units are stacked on each other onto the substrate and self-organized into desired structures and functionalities via interaction forces. For example, NP building blocks can be used to build monolayer or multilayer structures by some degree of control to direct the aggregation process. These methods comprise self-organization of nanostructures and self-organization of nanostructures on templates. Comparing with the top-down method, bottom-up methods are easier to access and much cheaper. They can also produce homogenous nanostructures with few defects and long-range order, if the aggregation process is properly controlled.
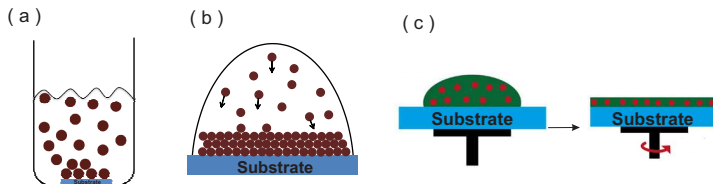
Figure 3.1: Schematics of NPs self-assembly routes: (a) Sedimentation, (b) Drop-casting and (c) Spin coating

Colloidal self-assembly methods of nanostructures are the most simplest methods

to prepare homogenous 2D and 3D NP arrangements. In this thesis, three self-assembly methods have been used, as shown in Figure 3.1. The parameters of each method are optimized to obtain NP arrangements with the best long-range order and least defects.

The first self-assembly method is sedimentation. Here, the NP dispersion sediment onto the substrate driven by gravity. The NP self-assembly process occurs during the evaporation of the solvent.

The second is dropcasting. The NP suspension is pipetted onto the substrate directly and the NPs self-assemble on the substrate during the evaporation.

The third method is spin coating. The substrate is fixed onto a rotating stage of a spin coating device via a vacuum pump. The NP suspension is dropped onto the substrate and subsequently spin coated with a tunable rotation speed and time. The thickness of the NP layer can be controlled by adjusting the rotation speed, time and the concentration of the NP suspension. Optimized parameters for a 2D NP monolayer are searched and recorded in the section 4.1.2.

3.2   Scanning Electron Microscopy (SEM)

The morphology of nanoparticles and thin films has been probed using a Scanning Electron Microscope (SEM, SU8000, Hitachi) at the institute PGI-7. In SEM, a beam of electrons is generated by a field emission gun. The electron beam is accelerated through high voltage and passes through a system of apertures and electromagnetic lenses to produce a focused beam of electrons. The beam scans the surface of the specimen by means of scan coils. Secondary electrons are emitted from the specimen and collected by a detector [89].

Two most commonly used modes in SEM are the secondary electron (SE) mode and the backscattered electron (BSE) mode. The SE mode is the process of detection of secondary electrons emitted by atoms in the specimen excited by the primary electron beam via inelastic scattering. By scanning the specimen and collecting the secondary electrons using a detector, an image that displays the morphology of the sample can be obtained. This mode is widely used to capture surfaces and provide high-resolution images. The BSE mode is the process of collecting the scattered primary beam electrons, scattered from the sample. BSEs emerge from deeper locations within the specimen and can probe the distribution of different elements in the sample. In our thesis, the SE mode has been used to check the morphology of the as-prepared thin film and NP arrangement, while the BSE mode has been used to analyse the layer structure of the ME sample.

3.3   Scanning Transmission Electron Microscopy (STEM)

The stacking geometry and the element distribution of the sample in cross-sectional direction are measured using a Scanning Transmission Electron Microscope (STEM,

FEI Titan 80-200) at the Ernst Ruska-Centre (ER-C) at the Forschungszentrum Jülich.

STEM is a type of transmission electron microscope (TEM). However, a STEM operates in a very similar way to a SEM; a focused electron beam is scanned over the sample. Electrons which pass through the sample are collected to produce a variety of transmission images.

The rastering of the beam across the sample makes STEM suitable for analytical techniques, such as High Angle Annular Dark-Field imaging (HAADF). The images arise from elastically scattered electrons. The HAADF signal is directly proportional to the density and thickness of the specimen and proportional to $Z^{3/2}$, where Z is the atomic number. Thus, it is possible to obtain images which show the contrast due to the mass-thickness or Z contrast.

STEM also offers microanalysis capabilities, i.e. energy dispersive X-ray analysis (EDX) and electron energy loss spectroscopy (EELS). In conventional TEM, the spatial resolution is limited to tens of Å, by the interaction volume of the beam within the sample. However, in STEM, the EDX analysis can be performed at the nanometer scale. EELS offers elemental mapping at 2 nm spatial resolution and achieves real-time mapping, which is particularly useful for the determination of valencies of the light elements and transition metals.

3.4 Atomic Force Microscopy (AFM)

The topography of the sample was probed by an Atomic Force Microscope (AFM, Agilent Technologies 5400).

Hereby, three types of modes are relevant, according to the nature of the tip motion: contact mode, tapping mode and non-contact mode. In our work, the non-contact mode is the most frequently used mode. Here, the tip is close enough to detect the sample surface for short-range forces (distance < 10 nm). Moreover, the tip avoids touching the sample surface.

In the probing process, the cantilever is first excited close to its resonant frequency. After the tip is brought in proximity of the sample surface, forces between the tip and the sample lead to a deflection of the cantilever, according to Hooke's law. The deflection changes its amplitude due to the various interactions between the surface and the tip. The deflection amplitude as the recorded signal reflects the height profile of the sample surface (Figure 3.2).

The topographic image, amplitude image, phase image and deflection image are recorded simultaneously in one measurement. Topography is often the most relevant one. It is possible to estimate both the lateral (xy) and height (z) information from this image; hence, the surface quality can be probed in terms of surface roughness. The root mean square roughness (R_q), which indicates the height distribution of the surface, is also an often-used parameter.
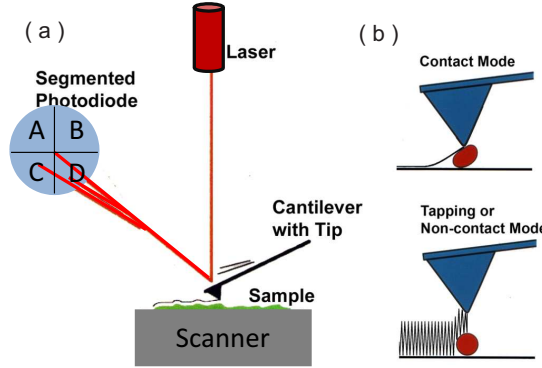
Figure 3.2: (a) Block diagram of AFM using beam deflection detection. As the cantilever is displaced via its interaction with the sample surface, the reflection of the laser beam is displaced on the surface of the photodiode; furthermore, the height and phase information are also calculated and obtained. (b) The AFM imaging modes: contact mode and tapping or non-contact mode.

3.5   Piezoresponse Force Microscopy (PFM)

The piezoresponse of BTO substrates with the application of a voltage was probed using a Piezoresponse Force Microscope (PFM, Keysight 9500 AFM) at the institute PGI-6.

PFM measures the mechanical response when an electrical voltage is applied to the sample surface using a conductive tip. In response to the electrical stimulus, the sample locally expands or contracts, as shown in Figure 3.3.
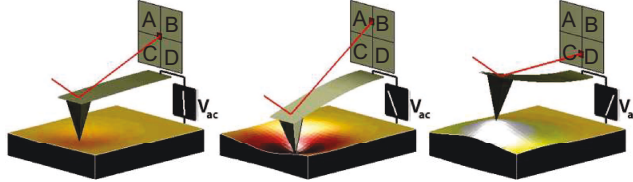
Figure 3.3: Depiction of the PFM operation. The sample deforms in response to the applied voltage, which, in turn, causes the cantilever to deflect. This can then be interpreted in terms of the piezoelectric properties of the sample. Image courtesy: S. Jesse, ORNL.

When the tip is in contact with the surface, the local piezoelectric response is detected as the first harmonic component of the tip deflection. The phase φ of the electromechanical response of the surface yields information about the polarization direction below the tip.

For c− domains (polarization vector oriented normal to the surface and pointing

downward), the application of a positive tip bias voltage results in the expansion of the sample. The surface topography is in phase with the tip voltage, i.e. $\varphi = 0°$.

For c+ domains, the response is opposite and $\varphi = 180°$. The detection of lateral components of the polarization can be realized by lateral PFM, which is a technique where the in-plane component is detected as lateral motion of the cantilever due to the bias-induced surface shearing. This option was not available at the instrument used here, unfortunately.

3.6 SQUID magnetometry

The Magnetic Property Measurement System (MPMS, Quantum Design) is a dedicated equipment used for measuring the magnetic properties of various types of samples. Here, an external magnetic field up to 7 T with a field uniformity of 0.01% over a range of 4 cm can be applied. The MPMS also provides a high-precision temperature unit that covers a temperature range of 1.9 to 400 K.

The MPMS magnetometer utilizes a Superconducting Quantum Interference Device (SQUID) to probe the magnetization very precisely down to 10^{-11} A · m². The SQUID magnetometer has as its main element a superconducting ring incorporated with a Josephson junction; the junction is inductively coupled to a RF circuit.

The sample moves through the second-derivative coils resulting in an inductive current. The current causes a magnetic field at the SQUID and leads to a impedance change in the superconductor ring and subsequently causes a change of the voltage amplitude in RF circuit. The change in the voltage amplitude gives the response function with respect to the sample position. Hence, the magnetic moment of the sample can be determined by fitting the measured response curve to a theoretical one.

The Reciprocating Sample Option (RSO) is a sample transport mode for samples with small magnetic moment. RSO offers a relatively fast type of measurement, which then allows averaging and good noise rejection. Another frequently used option is the DC option, which is also the default mode in MPMS. Here, a stepped DC scan is performed and the sample starts at the lowest point of the scan length and sequentially moves the sample upwards through the pickup coils.

More details regarding the SQUID magnetometry can be found in the MPMS hardware manual [90].

Since the manipulation of the magnetization with respect to an applied electric field is of interest, not only magnetic fields, but also electric fields need to be applied to the sample. One can apply electric fields throughout the sample via conductive wires from a power supply. The sample is fixed at a Vespel rod which is covered by a straw. The Vespel rod is further connected to a conductive sample rod. Electric connection between the sample and the power supply is implemented by two copper wires and the sample rod. One wire is attached on the surface of the sample via sliver paste and the other wire to the bottom. Both voltages at the positions of sample and the power source were measured to make sure the voltage loss on the way from power source to sample is less than 5%.
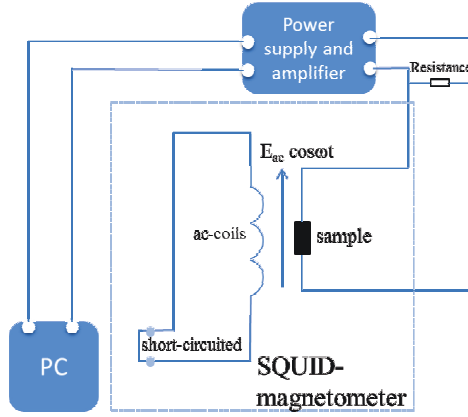
Figure 3.4: Schematic illustration of the MEACS setup attached to the SQUID magnetometer.

The Magnetoelectric AC susceptibility (MEACS) option is realized by utilizing the magnetic AC susceptibility (MACS) option. The AC coil was disconnected and short-circuited, and instead, an electric application setup was introduced to apply a DC or AC electric field on the sample, which was remotely controlled by the MACS option. The concrete connections are shown by a schematic diagram in Figure 3.4. Here, a resistance is introduced between the sample and the power amplifier (Krohn-Hite Corp., model 7602) to transform the driving current $I = I_{max} \sin(\omega t + \varphi)$ into a corresponding voltage $U = RI_{max}\sin(\omega t + \varphi)$. The voltage can be amplified and biased to a maximum value of 200 V. The phase between the driving voltage and the voltage output is monitored using an oscilloscope (TDS220, Tektronix) to ensure there is no phase shift in the frequency range of 1 to 10 Hz. More details about the principle of MEACS measurement are given by Borisov in Ref.[91].

The lock-in technique provides accurate signals as one expects to obtain from the measurements. It uses the frequency of the sinusoidal AC electric field as a reference signal and yields the first Fourier coefficient of the input signal as output for two phases shifted by 90°, corresponding to m' and m''. Analogy to the MEAC, the two components probed in the MEACS measurement are the real part of the susceptibility m' and imaginary part m''. $m' = \chi_{ME} \cos \varphi E_{ac} V$, where χ_{ME} is the magnitude of the magnetoelectric susceptibility and φ is the phase shift of the signal due to the delay or loss of the signal, E_{ac} is the applied AC electric field and V is the volume of the system. m' contains the information of the magnitude of the system's susceptibility to the changing of electric field. Mathematically speaking, it indicates the slope of the magnetization between $+E_{max}$ and $-E_{max}$. $m'' = \chi_{ME} \cos \varphi E_{ac} V$, which means the dissipative process in the system might result from irreversible domain wall movement, etc.

To better understand the physical meaning of m', a comparison measurement

between m' and ΔM in dependence of temperature on the system of Au / BTO / Ti / NP / Au was probed and shown in Figure 3.5. In the ΔM measurement, electric fields were manually tuned between $+E_{max}$ and $-E_{max}$ at each temperature point, and at each $+E_{max}$ and $-E_{max}$, the m_{+E} or m_{-E} was measured, respectively. ΔM was obtained by the subtraction of m_{+E} and m_{-E}. As seen from the figure, ΔM follows the behavior of the temperature dependent m' measured in the MEACS option, i.e. the signal jump happens at both phase transitions, which is indicated as the grey bars in the figures, and the scales of both measurements also match. Thus, the result reveals that if the AC electric field amplitude and frequency were controlled in a reasonable low range, m' approximately equals the magnetization difference between $+E_{max}$ and $-E_{max}$.
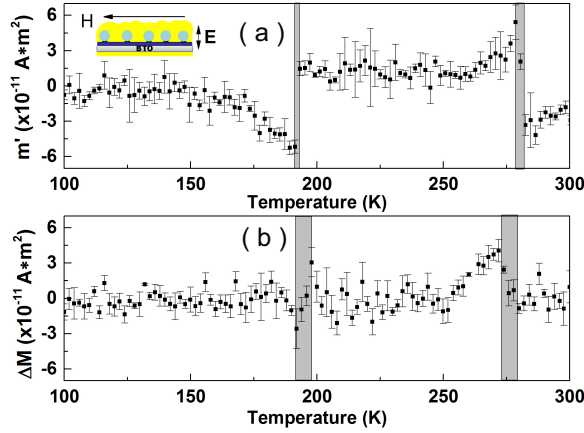
Figure 3.5: m' and ΔM in dependence of temperature on sample Au/BTO/Ti/Ti/NP/Au (a) MEC measured with MEACS option in MPMS at the frequency of 1 Hz and E_{max} of 3.2 kV/cm. (b) measured in the DC option in MPMS with an attached electric power source to apply 3.2 kV/cm on the sample, ΔM is obtained by manually switching the electric field polarization point by point and subtracting each negative to positive electric field result.

However, to be comparable with other ME materials, m' is converted into the so-called real part of the ME coefficient $\alpha_{ME} = \frac{\mu_0 m'}{EV} = \frac{\mu_0 M'}{E}$, where μ_0 is the vacuum permeability. m'' is conversed into the imaginary part of the ME coefficient $\alpha_{ME} = \frac{\mu_0 M''}{E}$ in the following results. The specific derivation of real and imaginary parts of α_{ME} to be $\mu_0 M'/E$ and $\mu_0 M''/E$ and their units are attached in appendix A.

A reference sample, a Cr_2O_3 single crystal (3 mm x 3.5 mm x 0.5 mm), was used to calibrate the MEACS setup. The measured results were compared to the results measured in W. Kleemann's group as shown in Figure 3.6. The ME coefficient α_{ME} is introduced from the equation $\alpha_{ME} = \frac{\mu_0 m'}{EV}$, where m' is the measured real part of the susceptibility, E is the applied electric field and V is the volume of the measured sample. From the figure, one finds that the reference data corresponds
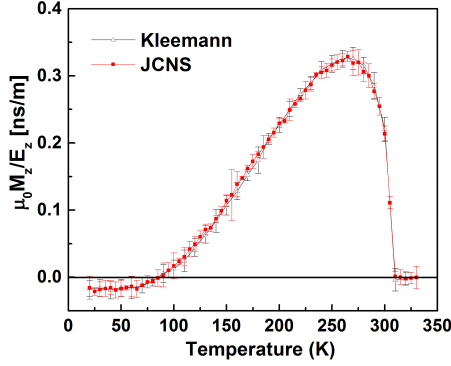
Figure 3.6: ME coefficient α_{ME} of a Cr_2O_3 single crystal vs temperature measured at $f = 1$ Hz and $E_{max} = 63.4$ kV/m after ME field cooling. Reference data points are reproduced from W. Kleemann (see Ref [91]). The $y = 0$ line is a regular line of the coordinate system.

with the literature data.

3.7   X-ray Reflectometry/Diffractometry (XRR, XRD)

The thickness, roughness and crystalline quality of the prepared layers, including thin films and self-assembled NP layers, were characterized using the X-ray diffractometer (D8 Advanced, Bruker AXS) at JCNS-2.

An X-ray beam with a wavelength of $\lambda = 1.54$ Å is generated by a Cu-κ_α source and collimated by a Göbel mirror and two slits. A monochromator is used to narrow down the wavelength band of the X-ray source. A vacuum sample stage is available to provide the possibility of measuring the sample in vacuum. Moreover, a temperature unit can be attached to the sample stage to measure the sample in the temperature range from room temperature to 700 K. A heater and a water cooling system are responsible for warming up and cooling down, while a thermocouple is used to measure the temperature. Besides this, a knife-edge collimator is installed to have an optimal collimation of the incident beam and a suppression of background. The outgoing beam passes another combination of Göbel mirror and slits and is recorded by the detector.

The X-ray diffractometer mode is used to determine the crystalline quality and out-of-plane lattice parameters. It also can be used in a reflectometer mode to investigate the thickness and laterally averaged roughness of the film. To fulfill the requirements of each kind of experiment, the slits can be changed.

3.8 Grazing Incidence Small Angle X-ray Scattering (GISAXS)

The size distribution of NPs as well as the in-plane correlations of self-assembled NPs were determined using the grazing-incidence small-angle X-ray scattering (GISAXS) instrument $GALAXI$ at JCNS-2.

The X-rays are produced by an electron beam hitting a liquid metal jet of a GaInSn alloy. After the parabolic optics, the X-ray beam is directed through the 4 m long collimation. Afterwards, two slits are used to define the size of the beam. The beam arrives at the sample position with a flux of $1 \cdot 10^9$ photons/mm$^2 \cdot$s.

The sample can be adjusted in the beam with 2 translational and 2 rotational degrees of freedom. After the X-ray beam is scattered at the sample, the reflected beam is received by a detector with 169 x 179 mm^2 active area. The distance between the sample position and the detector can be adjusted from 835 mm to 3535 mm to fill the material with different correlation sizes up to 200 nm. The schematic diagram of the GISAXS geometry on a self-assembled NP monolayer can be seen in Figure 3.7.
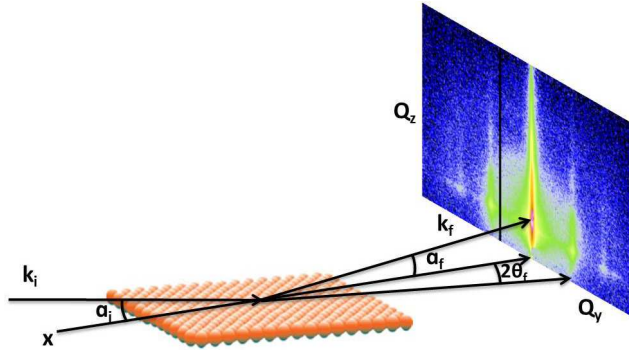
Figure 3.7: The geometry for GISAXS experiments. The Bragg reflections are superimposed by the blurry powder rings. This results from the scattering of the X-ray on the carbon gratings, which are in front of the 2D detector in order to fix the Kapton window.

The intensity of the X-ray beam detected by the 2D detector provides information about the electron density profile of the NPs statistically averaged over the area of the illustrated sample. With $\vec{Q}$ being the scattering vector, lateral correlations are found in the Q_y direction, while out-of-plane correlations are probed in the Q_z direction. The 2D detector hereby records the Q_y - Q_z plane. For the case of a monolayer of NPs, and hence, for the case of a 2D lattice, Bragg peaks appear as vertical stripes in the Q_y - Q_z detector plane. Their intensity along Q_z in modulated due to the laterally averaged electron density distribution in the layer.

The stripe distance d and the lattice constant a are related according to the equation

$$d_{hk} = \frac{a}{\sqrt{\frac{4(h^2+hk+k^2)}{3}}} = \frac{2\pi}{Q_y^{hk}} \tag{3.1}$$

Here, h and k are the Miller indices and Q_y^{hk} is the position of the rods (2D-Bragg peak).

3.9   Polarized neutron reflectometry (PNR)

The magnetization depth profile of the iron oxide NP monolayers were investigated using Polarized Neutron Reflectometry (PNR) at the instrument MARIA at Heinz Maier-Leibnitz Zentrum (MLZ) in München.
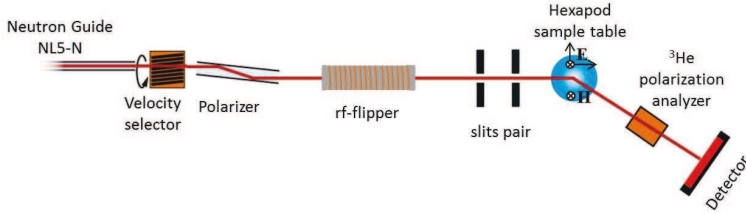
Figure 3.8: Schematic setup of the Polarized neutron reflectometer MARIA.

The setup is schematically shown in Figure 3.8. The white neutron beam is produced by the reactor and passes through a velocity selector. Since MARIA is designed for a Q range from (0.002 Å^{-1} to 3.2 Å^{-1}), the velocity selector chooses the wavelength from 4.5 Å to 40 Å and provides a wavelength distribution of $\triangle\lambda/\lambda$ = 0.1. Next to the velocity selector is a polarizer. The beam is polarized by a double reflection polarizer, which is essential for the PNR. A RF-flipper is used to flip the spin state of neutrons. Before the neutron beam is scattered by the sample, a pair of slits is used to optimize the beam size to balance the resolution and the final intensity.

The setup is optimized for sample sizes of 1 x 1 cm^2 by using a vertical focusing elliptic neutron guide. The sample is mounted on a hexapod, which provides the movement of the sample. The sample space is covered by the closed cycle cryostat that can be pumped to 10^{-6} mbar, which reduces the scattering from are during the measurement. Meanwhile, the cryostat provides the temperature, ranging from 4 K to room temperature. This space is the only region in the entire measurement path where one can manipulate the magnetic field. A special sample holder is designed for our measurements to apply an electric field on the sample. The sample holder is made of aluminum and covered with boron, which is a good neutron absorber.

The bottom electrode is connected to the ground of the cryostat via the aluminum holder, while the top electrode is connected by a copper wire to the electric generator through the pinhole in the cryostat. With this setup, a voltage of up to 500 V can be applied at the sample position.

Behind the sample, the neutron state is analyzed via a ^{3}He cell analyzer for a full horizontal polarization analysis. Finally, the neutrons are detected using a 400 x 400 mm^2 ^{3}He 2D detector..
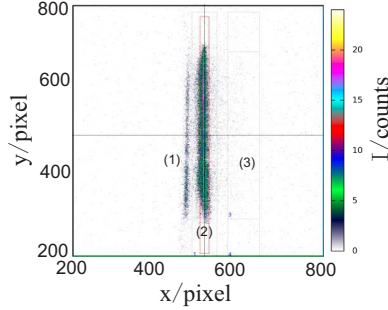
Figure 3.9: Detector image taken at MARIA. (1) is the tail of the almost blocked direct beam and the intensity in the rest area, (2) represents the region of interest, which is the beam reflected region, and (3) contributes to the background.

The instrument saves one detector image for each angle, and an example of the detector image is shown in Figure 3.9. The almost blocked tail of the direct beam is shown in region (1). The reflected beam is shown in region (2), which is also the region of interest. A Gaussian profile is used to fit the distribution to give the final intensity. Region (3) indicates the background that comes from the scattering on air, the sample holder and the other components within the neutron beam path. For every final reflected intensity, the background intensity has to be subtracted. At last, the final reflected intensities are collected to obtain the final Q-dependent reflectivity curve.

Chapter 4

Results I: Iron oxide NPs on BTO single crystals

In this chapter the results of the iron oxide NPs on BTO substrates are presented. Iron oxide NPs are self-assembled on BTO substrates as monolayers and multilayers, respectively. First, the results on the characterization of the structural properties of BTO substrates are presented. This is followed by the magnetic and magneto-electric properties of the sample iron oxide NP monolayers on BTO substrates as the main part. After the analysis of the magnetic profile performed by PNR, the characterization and investigation results of the iron oxide NP multilayers on BTO substrate are introduced.

4.1 Sample preparation

The characterization of the BTO substrates will be presented including their topography, piezoelectric property, dielectric property and domain deformation depending on electric field and temperature. Afterwards, the preparation of the samples ranging from BTO / NP monolayers up to the final sample Au / BTO / Ti / NP monolayers / Au will be introduced.

4.1.1 BTO single crystals

(001) oriented BTO single crystals with the size of 5 mm × 5 mm × 0.5 mm and 5 mm × 5 mm × 0.1 mm are commercially available from CrysTech GmbH. These BTO single crystals are used as substrates to support the self-assembled NP monolayers. Since clean substrates are needed to obtain smooth films, the BTO substrates were first cleaned with acetone to remove organic residuals on the surface. Afterwards, they were annealed at 1200 K in an oxygen atmosphere at a pressure of $1 \cdot 10^{-6}$ mbar for 6 h to remove adatoms like carbon. The surface quality was checked by AFM and the surface topography is shown in Figure 4.1(a). A stripe-like corrugation is seen from the figure. The possible reason responsible for the
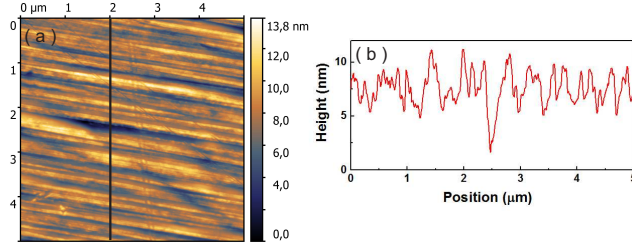
Figure 4.1: (a)Topography of the (001) oriented BTO substrate measured by AFM. The stripe pattern in the image results from the different domain structures in the BTO substrate. (b)Line scan profile. The position of the extracted line is indicated as a black line in (a), the line cut profile indicates BTO corrugations reaching a height of up to 8 nm.

corrugations is the formation of differently oriented a- and c- domains in the BTO in the tetragonal phase at room temperature.

In order to quantitatively evaluate the roughness of the substrate, a line cut perpendicular to the long direction of domain structures was made which is marked as a black line in the AFM image. The plot in Figure 4.1(b) indicates that each domain structure has a width around 0.2 μm. It is clearly seen that some domain corrugations reach a height of 8 nm. They are the main cause of the surface roughness.

The piezoelectric response of the BTO substrate was evaluated by PFM at the PGI-6, Forschungszentrum Jülich which is shown in Figure 4.2. The [001] direction
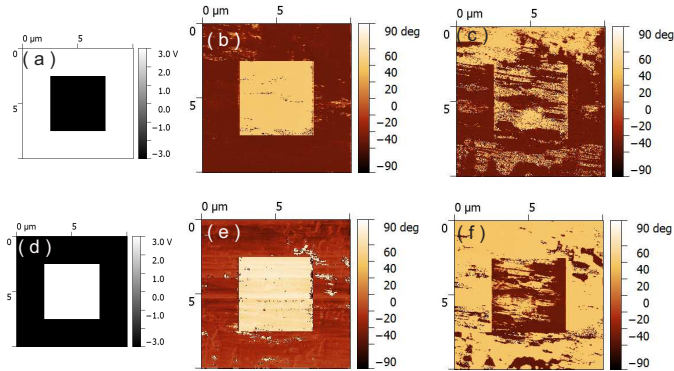
Figure 4.2: BTO substrate measured by PFM.(a) and (d) represent the electrode pattern. The white area is the area where the voltage of +3V was applied and the black area is where -3V was applied. (b) and (e) are the PFM phase images measured during the electric field application. (c) and (f) are the PFM phase images measured after removing the electric field.

of the as-prepared BTO substrate was aligned parallel to the sample stage. The sample was measured in the range of $10 \times 10 \ \mu m^2$. For the PFM measurement, a patterned electrode was attached to the sample to provide the electric field. The schematic drawing of the electrode pattern is shown in Figure 4.2 (a) and (d). The inner square has a size of $5 \times 5 \ \mu m^2$. During the measurement of (b), $+3$ V were applied to the white area and -3 V were applied to the black area. After poling for 30 s, the phase image of the BTO substrate was recorded as shown in (b). The inner square shows a polarized phase of 60 degrees while the outer shell shows a polarized phase of -60 degrees.

The application of a higher voltage is not possible in this setup. It can be expected that one could polarize the two areas by a 180 degree difference with a larger voltage [92]. The same measurement was conducted again immediately after removing the electric field. The BTO substrate shows a remanent polarization. However, the remanent polarization vanishes with time. The electrode pattern on the BTO substrate with an opposite electric field was applied and similar results are seen in (e) and (f). PFM measurements thus reveal the polarization state of the BTO surface and that it can be tuned under electric fields of few volts.
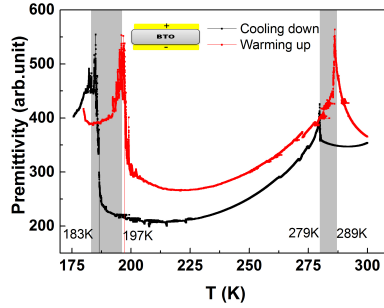
Figure 4.3: Permittivity versus temperature of the 0.5 mm thick BTO substrate. An AC electric field was applied to the sample Au/BTO/Au. The sample was first cooled down from 300 K to 10 K without electric field and by the application of an AC electric field, the sample was probed while warming up and subsequent cooling down.

The temperature dependent permittivity of the BTO substrates was investigated using the Closed Cycle Measurement System (CCMS) from Cryogenics Ltd. Hereby, a sample with 10 nm Au / 0.5 mm BTO / 10 nm Au was prepared. The results are shown in Figure 4.3. The sample was first cooled down to 10 K. Afterwards, an AC electric field with a frequency of 9 Hz and amplitude of 20 kV/cm was applied to the sample. The measurements were carried out first during the direction of warming up (FW) and then cooling down (FC).

Two peaks are observed in both curves, 197 K and 289 K for the FW branch and 183 K and 279 K for the FC branch, respectively. The first peak at lower temperature indicates a phase transition from the R to O phase, while the other

one at higher temperature corresponds to the phase transition from the O to T phase. The temperature difference of the same phase transitions between FC and FW curves results from the lattice thermal hysteresis [93].

The surface roughness of the BTO substrate was reduced by the application of an electric field via unifying the domain structures. The evolution of the BTO domain structures under an electric field was probed by a laser system as shown in Figure 4.4. The multiple reflections in Figure 4.4(a) represent the reciprocal space of the stripe-patterned domains which was also observed by AFM before. After gradually increasing the voltage to 300 V, the multiple reflections vanish and a single reflection appears (seen in Figure 4.4(b)). If the electric field is switched back to zero, the BTO substrate gradually recovers the stripe-patterned corrugations which are confirmed as the reappearance of the multiple reflections pattern as shown in (c).

A negative electric field has a similar effect onto the BTO surface judging from the appearance of the reflection pattern. The results are shown in (d) and (e). It is worth mentioning that the evolution of the reflection pattern is reproducible which indicates that the BTO corrugations can be manipulated by the application of an electric field. However, when the voltage increases beyond 350 V, sparking occurs. In order to avoid the short circuiting of the substrates, such strong electric fields should be avoided.
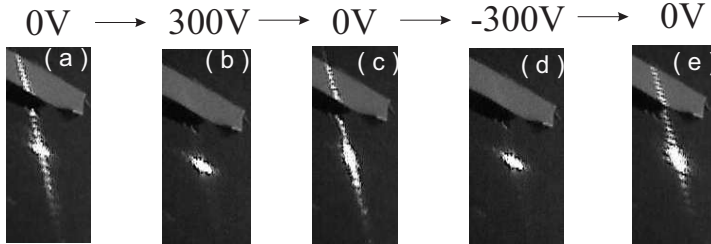
Figure 4.4: Reflection images by a laser beam system from a 10 nm Au / 0.5 mm BTO / 10 nm Au sample. The electric field applied to the sample is in the range from -300V to 300V. The evolution from multiple reflections pattern to a single reflection pattern and back to a multiple reflections pattern indicates the manipulation of BTO domain structures by the electric field. The chip in the image was used as a reference position of the reflection laser pattern.

X-ray θ - 2θ scans of the 200 reflections of the BTO substrate from 300 K to 420 K are shown in Figure 4.5. The samples were first warmed up to 450 K and then measured while cooling. Only the 200 peak is observed at 420 K which indicates the cubic symmetry of BTO being paraelectric.

However, as the temperature decreases to 380 K, the peak splits into two peaks as shown in Figure 4.5(b). The two peaks separate from the original peak and they can be indexed as the (200) and (002) peaks using the BTO tetragonal symmetry. The peak splitting is associated with the phase transition of BTO.
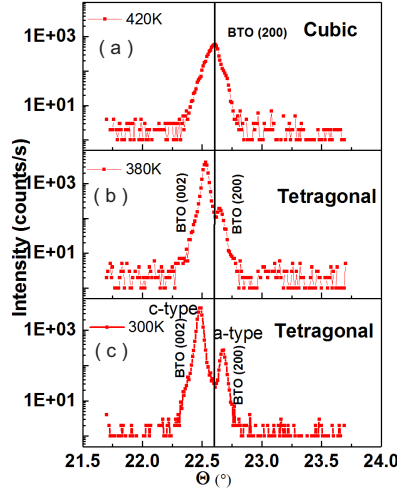
Figure 4.5: Temperature dependent XRD scans on the 200 Bragg peak of the BTO substrate. The samples were first heated up to 450 K and measured while cooling down in the sequence of (c) 420 K (b) 380 K (a) 300 K. The black line is used for a better visualization of the peak shift. The Cubic and Tetragonal phases are marked under the consideration of theoretical values.

Depending on the direction of the lattice extension, a-type and c-type domains are formed [68]. However, the narrow peaks indicate that BTO at this temperature shows a coexistence of C and T phases with the cubic lattice still dominating. The peak splitting becomes more pronounced after further decreasing the temperature to 300 K which suggests that more a- and c-type domains are formed. Due to limitations of our setup, it is not possible to measure the domain state below room temperature.

4.1.2 NPs self-assembled on BTO

Iron oxide spherical shaped NPs with a diameter of 20 nm and 8% size distribution were commercially obtained from Ocean NanoTech LLC (See Appendix B). The NPs were synthesized by thermolysis of an iron precursor in presence of oleic acid and dispersed in toluene. The initial composition is a mixture of ferrimagnetic maghemite (γ-Fe_2O_3) and antiferromagnetic wuestite(Fe_xO) [94, 95].

In order to obtain homogenous 2D iron oxide NP monolayers on BTO substrates, three different colloidal self-assembly methods were used to self-assemble iron oxide NPs. The schematics of the three methods are depicted in Figure 3.1. The first method is sedimentation and is shown in Figure 3.1(a). BTO substrates were placed at the bottom of a beaker which is filled with toluene. 30 μl of iron oxide NPs solution was dropped into the beaker by a transferpettor. The gravity driven NP sedimentation took 1 h. Afterwards, the solution was evaporated in air for 12 h and
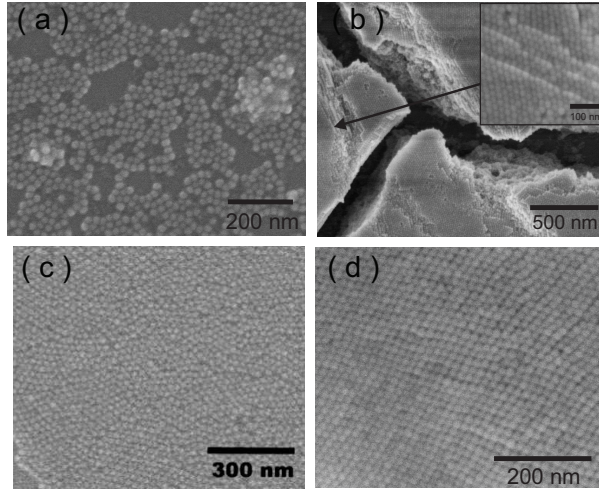
Figure 4.6: SEM images of iron oxide NPs self-assembled on a BTO substrate using the three methods, (a) sedimentation (b) dropcasting (c) spin coating at 50 rps for 45 s (d) spin coating at 15 rps for 20 s. The inset in (b) is a zoom-in look of the area indicated by the arrow.

NPs self-assembled on top of the BTO substrate during this period. The results are shown in Figure 4.6(a). The particles are arranged in a disordered state and some particles are aggregated in 3d clusters. Hence it departs from our aim to prepare a homogenous NP monolayer.

The second method is dropcasting. The schematic is shown in Figure 3.1(b). In the dropcasting process, 5 μl NPs solution are taken and dropped onto a 5×5 mm^2 sized BTO substrate. The solvent evaporated in air and the NPs self-assembled during this period. NPs mesocrystals were formed by this route and the results are shown in Figure 4.6(b). The cracks between mesocrystals developed at the moment when the sample is nearly dry. The NP arrangement is better seen from the zoomed-in image as shown in the inset. The NPs are arranged in an hexagonal pattern. However, the surface is still not homogenous enough.

The third method is spin-coating whose schematic diagram is shown in Figure 3.1(c). The optimized parameters for preparing a 2D NP monolayer were determined after the iteration of preparation and characterization. First, the NPs solution was diluted by a factor of 10 with toluene solvent. Then 2.5 μl diluted NPs solution were dropped onto a 5×5 mm^2 BTO substrate. After spin coating at 50 rps for 45 s, a homogenous NP monolayer was prepared. The results are displayed in the Figure 4.6(c). The NPs self-assembled into a hexagonally closed-packed arrangement as a monolayer of particles with approximately 80% coverage averaged over the substrate. For fabrication of NP multilayers, 15 rps and 20 s were used during the spin coating process while the other parameters were kept the same. The

morphography of multilayers is seen in Figure 4.6(d). The surface of the layer is homogenous and in some regions, NPs are arranged almost in a crystalline fashion.
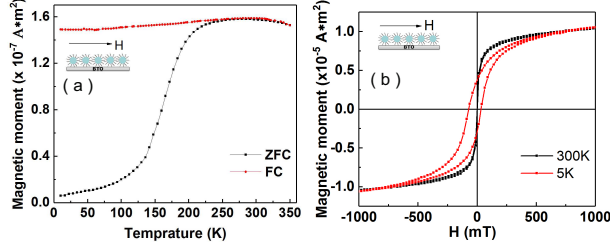
Figure 4.7: (a) Magnetic moment versus temperature curves of a NP monolayer on top of a BTO substrate after ZFC and FC measured at a magnetic field of 5 mT by SQUID.(b) Magnetic moment versus magnetic field at 300 K and 5 K for the same sample. The inset shows the schematic of the sample and the direction of the magnetic field applied on it.

The magnetization of the NP monolayers on BTO substrates as a function of temperature or magnetic field is shown in Figure 4.7. The M-T curve displayed in Figure 4.7(a) shows a typical superparamagnetic behavior of iron oxide NPs, i.e. the FC and ZFC curves show a peak marking the blocking temperature of the iron oxide NPs at around 275 K. The M-H curves of the sample, displayed in Figure 4.7(b) were probed at 300 K and subsequently at 5 K. The closed hysteresis loop at 300 K indicates the unblocked state of superparamagnetic NPs while the open loop at 5 K corresponds to the blocked state.

The exchange bias effect observed from the hysteresis loop at 5 K is due to the existence of the AFM component FeO_x (wüstite) inside the NPs. FeO_x has a Néel temperature of 190 K [94].

4.1.3 BTO / Ti / NP monolayers

For the samples of the type BTO / Ti / NP monolayer, before the NPs were spin-coated onto the BTO substrate, a Ti buffer layer of 7.8 nm thickness was deposited onto the BTO using a molecular beam epitaxy (MBE) setup (please see Section 5.3.1). The surface quality of the film was checked by the XRR and the data is presented in the next section.

In order to remove the organic oleic acid shell around the NPs, the samples were treated in an oxygen plasma asher (PNA Telpla 300, CNST) with an oxygen pressure of 0.3 mbar, a gas flow of 200 ml/min and a power of 3000 W for 5 min. After oxygen plasma etching, a fraction of γ-Fe_2O_3 is hereby transformed into Fe_3O_4. The influence of oxygen plasma etching onto iron oxide nanoparticles is similar to the thermal annealing process as reported both by M. J. Benitez and Gena Wilbs [94, 95].

4.1.4   Au / BTO / Ti / NP monolayer / Au

In order to obtain more pronounced ME coupling effect, a 25 nm thick Au capping layer was deposited again by MBE. For electrical contacting and to apply an electric field across the sample, a second Au layer was deposited onto the opposite BTO surface. In this way the two Au layers serve as bottom and top electrode, respectively. Moreover, several reference samples, i.e. without Ti layer, without NPs, without Au capping or using a Si substrate instead of BTO have been prepared to compare to the complete sample (Au / BTO / Ti / NPs / Au).

In order to check the thickness and roughness of the as-prepared samples, XRR was used to measure the samples in each preparation step and the results are collected in Figure 4.8.
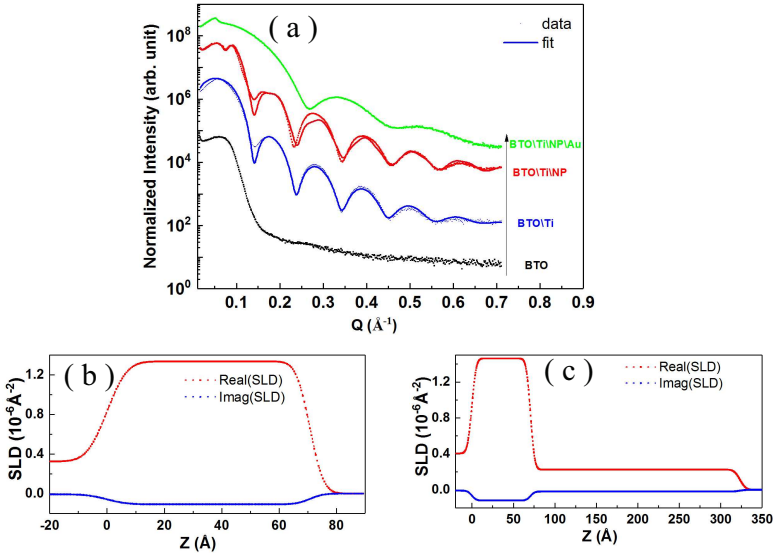
Figure 4.8: (a) XRR measurements for each sample preparation step from BTO substrates to the final sample BTO / Ti / NP / Au. The arrow indicates the preparation sequences of each sample with the sample geometry marked besides it. The fit of the XRR data of the samples BTO / Ti and BTO / Ti / NP are given as solid lines. The resulting SLD as a function of the layer thickness for (b) the sample BTO / Ti and (c) the sample BTO / Ti / NP.

The XRR curve of BTO substrates shows a plateau and then dies out very quickly indicating a large roughness of the surface.

The XRR curve of BTO / Ti shows several Kiessig oscillations up to a Q value of 0.6 Å^{-1} indicating a good quality of the Ti film. The further results of the fit shows the thickness of the Ti layer is 7.8 $\pm$ 0.3 nm and the roughness is 0.3 nm. The nSLD is plotted against the layer thickness z in Figure 4.8(b). The real part of nSLD gives the dispersion while the imaginary part gives the absorption.

The XRR curve of BTO / Ti / NP shows an additional superimposed peak at the first two oscillations which corresponds to the NP monolayer. The results from the fit provides a NP monolayer thickness of 22.4 ± 1.1 nm with a roughness of 3.1 nm. The nSLD as a function of z is plotted in Figure 4.8(c).

The XRR curve of BTO / Ti / NP /Au shows only two broad Kiessig oscillations which is due to the large SLD and absorption of Au layer to the X-ray. X-rays only penetrates several nanometers into the Au layer and are blind to the layer below.

4.2 Results

At the beginning of this section, the morphology of the self-assembled NPs on BTO substrates are presented being characterized by SEM and GISAXS. Further measurements were performed on BTO / Ti / NP / Au samples by SEM and STEM. The magnetic properties were studied using a SQUID magnetometer, the MEC effect using a MEACS option attached to the SQUID magnetometer and the E field manipulation of the magnetic depth profile using PNR.

4.2.1 Macroscopic magnetic properties
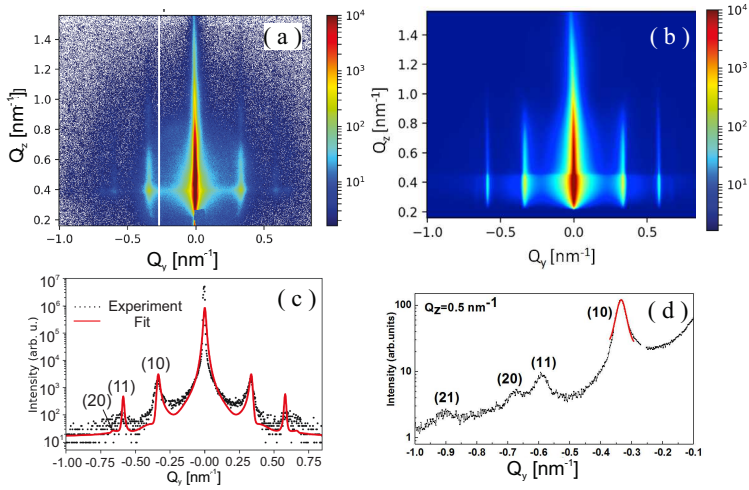
Figure 4.9: (a) GISAXS pattern of an iron oxide NP monolayer spin-coated onto a BTO substrate (sample BTO / NP). The white line is a dead region of the detector. (b) Simulation of the GISAXS data by the BornAgain software. (c) shows the intensity of experimental (black dash line) and simulated (red solid line) data as a function of Q_y with the integration of Q_z (d) shows a line cut of raw data along Q_y at $Q_z = 0.5$ nm^{-1} along with a Gaussian fit (red line) to the (10) Bragg peak. Bragg peaks were indexed according to a hexagonal lattice with $a = 21$ nm.

A 8 nm thick Ti buffer layer on top of BTO substrate is prepared using an MBE setup before the NPs were spin-coated onto the BTO substrate. Subsequently, NPs were self-assembled onto the BTO / Ti layer by spin coating, as described in section 4.1.2. During the spin-coating procedure, the NPs self-assemble in a hexagonally closed-packed arrangement as a monolayer of particles with approximately 80% coverage averaged over the substrate. The overall morphologies of the self-assembled NPs was studied by GISAXS which are shown in Figure 4.9(a). The angle of the incident beam is $\alpha_i = 0.1°$. The observed vertical intensity rods in the Q_z direction are due to the monolayer nature of the NPs. The 2d-Bragg rods were successfully indexed assuming a two-dimensional closed packed hexagonal lattice with a lattice constant of $a = 21.03 \pm 0.53$ nm. The observed stripe positions and calculated positions based on the NP diameter match well confirming the hexagonal arrangement. The data is fitted by the BornAgain software as shown in Figure 4.9(b). A truncated spherical NP shape is found to give a better fitting of the data, which might be due to the fact that X-rays with a certain incident angle only see a part of the spheres. The experimental data and its fitting are shown in Figure 4.9(c), the fitting intensity as a function of Q_y with the integration of Q_z shows a good agreement with the experimental data. The fitting confirms a hexagonal closed packed NP arrangement and the 21 nm lattice constant. The line cut at $Q_z = 0.5$ nm^{-1} along Q_y is shown in Figure 4.9(d). The intensity modulation along Q_z is related to the laterally averaged electron density of the NP layer. The plot demonstrates that the rods are relatively sharp in Q_y direction, indicating a good lateral order. After taking the instrument resolution into account, a Lorentzian profile is used to fit to the first order peak which yields a structural coherence length of 168 ± 9 nm, which indicates a relatively good supercrystalline NP ordering.

The NPs are coated with organic oleic acid shell, in order to remove the shell to get a more direct and pronounced MEC effect, the sample was treated in an oxygen plasma asher (PNA Telpla 300, CNST) for 5 mins with an oxygen pressure of 0.3 mbar, a gas flow of 200 ml/min and a power of 3000 W. Structural characterization of the NP ordering of the sample is performed using SEM as displayed in Figure 4.10(a) for the uncoated sample. From the comparison between the SEM pictures of NPs before and after oxygen plasma, it can be seen that the oxygen plasma treatment has obviously no effect on the ordering of the NPs.

Figure 4.10(b) and (c) show the results of different sample processing steps, i.e. after oxygen plasma etching to remove the oleic acid shells (Figure 4.10(b)) with the 8 nm Ti layer between the substrate and NPs, and after coating the NPs with a 25 nm Au layer (Figure 4.10(c)). The Au coating almost covers perfectly the NP layer as a percolated Au network embedding the NPs. This is evidenced by our STEM/EDX observation.

Figure 4.11(a) shows the morphology of the multilayer system viewed along the cross-sectional direction. The upper white area represents hereby the Au layer. The elemental maps (Figure 4.11(b–f)) detected by EDX clearly identify the Au / NP, NP / Ti and Ti / BTO interfaces, in which the BTO / Ti and Ti / NP interfaces are further manifested by the dark-contrast stripes in the oxygen map. It can be clearly
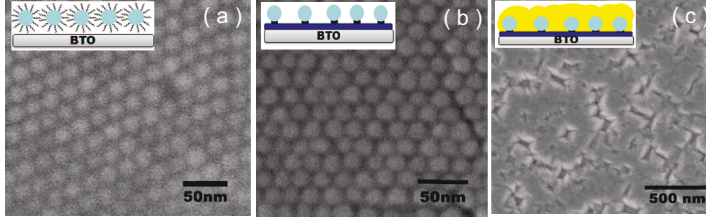
Figure 4.10: (a) Zoomed-in on-top view of the BTO / NP sample observed by SEM. (b) A similar sample but with an 8 nm Ti layer deposited before spincoating the NPs. Moreover, the sample was treated in oxygen plasma (sample BTO/Ti/NP). (c) The same sample after deposition of a 25 nm Au capping layer on top of the NPs (sample BTO / Ti / NP / Au). Note the different scale between (c) and (a)(b).
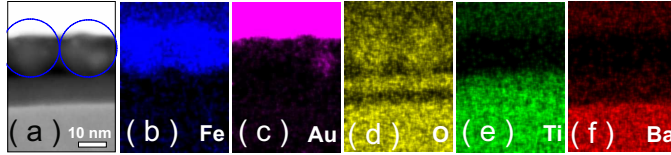
Figure 4.11: Energy-dispersive X-ray spectroscopy in scanning transmission electron microscopy mode (STEM–EDS) acquired at 200 kV.(a–f) Z-Contrast high-angle annular-dark-field STEM image showing the stacking sequence of different layers in the BTO / Ti / NP / Au sample and the simultaneously collected EDX maps of Fe (blue), Au (pink), O (yellow), Ti (green) and Ba (red), respectively. The scale bar in (a) represents 10 nm vertically. The scales are identical for the panels (a–f). The dashed circles with a radius of 21 nm in (d) indicate the NPs as a guide to the eye.

seen that the top surface of the Ti layer is oxidized while the bottom surface is oxygen-free, i.e. the dark band at the Ti / BTO interface indicating a pure metallic Ti layer. In addition, the coverage of the Au layer of about half of the particle diameter is revealed from the Fe and Au maps, see Figure 4.11(b and c). The oxygen map in Figure 4.11(d) shows that there is no oxygen gap between the TiO_2 layer and NPs. This is most probably due to the fact that the NPs are attached with the TiO_2 layer after oxygen plasma treatment.

A more direct evidence of the oxidized Ti layer can be seen in electron energy loss spectroscopy (EELS) of Ti which is displayed in Figure 4.12. The EELS experiments were performed on an FEI Titan 80-200 Chemi-STEM microscope with an operating voltage of 200 kV. The energy resolution for the EELS experiments was 1.5 eV, which is defined by full-width-at-half-maximum of the zero-loss peak. The energy dispersion used for collection of the electron energy loss spectrum is 0.25 eV/pixel with an entrance aperture of 2.5 mm.

The high-angle annular dark-field image (HAADF) is shown in Figure 4.12(a) where the lattice planes of the BTO substrate can be seen. The EELS of the elements
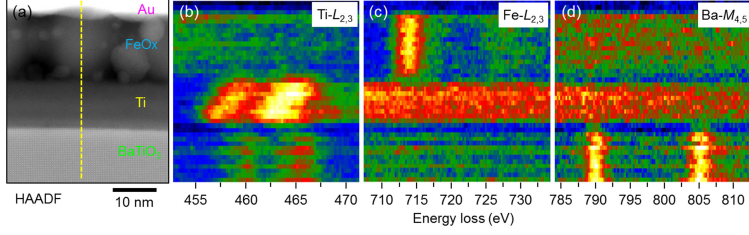
Figure 4.12: EELS study of sample Au / BTO / Ti / NPs / Au. (a) high-angle annular dark-field image (HAADF) image of the cross-sectional nanostructure. The yellow dashed line denotes the linear region of interest for EELS characterization. (b)-(d) Stacked absorption edges of (b) Ti-$L_{2,3}$,(c) Fe-$L_{2,3}$ and (d) Ba-$M_{4,5}$ collected from the linear region of interest indicated in (a). The vertical axis corresponds to the real space distance in (a).

Ti, Fe and Ba are shown in (b) to (d) respectively. The two vertical stripes in the bottom part of the Ti map indicates the uniform valency state of Ti in the BTO substrate. The two brighter oblique stripes above represent the different Ti valency states in the Ti and TiO_2 layer. The Fe map indicates the uniformity of the Fe valence state of iron oxide NPs. However, the broadness of the stripes indicate the coexistence of several iron valences states.

Moreover, several reference samples, i.e. without Ti layer, without NPs, without Au capping or using a Si substrate instead of BTO have been prepared to compare to the complete sample (Au / BTO / Ti / NPs / Au).

Magnetometry measurements were performed using a superconducting quantum interference device (SQUID) magnetometer.

On these three sample structures magnetometry measurements were performed. Figure 4.13 (a-c) shows the magnetic moment as function of temperature for (a) the untreated NP monolayer on top of the BTO substrate (BTO/NP), (b) the oxygen plasma treated NP monolayer deposited onto a Ti buffered BTO substrate (BTO/Ti/NP), and (c) the complete system, where the NPs are embedded in an Au top layer (BTO/Ti/NP/Au).

In each case the measurement protocol was the following: starting from 300 K the samples were first cooled in zero field down to 10 K. Subsequently, a constant field of 5mT was applied and the field warming (FW) curve recorded upon warming up to 350 K. At the same applied field the sample was then cooled and the FC curve recorded. All three measurements were performed at the same cooling/heating rate of 2 K/min. In Figure 4.13, the FC and FW curves are displayed to show possible temperature hysteresis effects upon warming vs. cooling. The results shown in Figure 4.13(a-c) were taken with magnetic fields oriented in-plane.

The comparison of the data from the three systems yields several interesting observations. For the sample BTO/NP, the FC and FW curves are basically identical to each other and only a slight kink at the $R - O$ phase transition at 190 K can be seen (Figure 4.13(a)). Since the particles are only weakly bound to the substrate
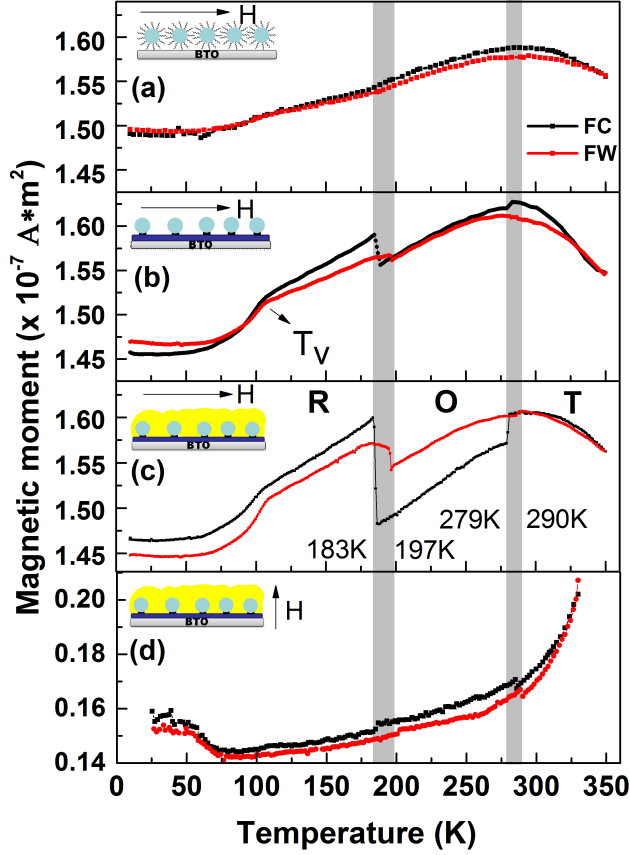
Figure 4.13: (a-c) In-plane magnetic moment vs. temperature during field warming (FW) and during subsequent field cooling (FC) in 5 mT for the three types of samples, (a) BTO / NP, (b) BTO / Ti / NP and (c) BTO / Ti / NP / Au as depicted schematically in the insets. (d) Out-of-plane magnetic moment under the same conditions to be compared to (c). The vertical grey bars indicate the temperature region, where bulk BTO has first order phase transitions from the T to O to R phase. T_V indicates the Verwey transition of magnetite.

by van der Waals interactions and because they are coated with an organic shell, no MEC is expected here. We attribute this kink to the magnetic response of the dipolarly coupled NPs to a change of the BTO corrugation and hence to the slight positional rearrangement of the NPs. Apart from the kink the curves are identical to those obtained on NPs on a Silicon substrate [24].

Self-assembled iron oxide nanoparticles on BTO substrates show typical superparamagnetic behavior (ZFC and FC curves of sample BTO/NP can be seen in Figure 4.7(a)). They correspond to the response of dipolarly interacting iron oxide NP [94].

For the sample BTO/Ti/NP, the FC and FW curves show magnetization steps near the $R-O$ transition at 190 K and the $O-T$ transition at 287K (Figure 4.13(b)). We assume that strain mediated MEC is responsible for the observed magnetization changes. The oxygen plasma treatment burnt the oleic acid surrounding the NPs into a carbon shell. In addition, the surface of the Ti layer was oxidized into titanium oxide. The carbon shell and the oxidized titanium oxide appear to be the critical components for providing a good adhesion of NPs to the BTO substrate, giving rise to a non-vanishing MEC. Comparable samples without a Ti layer yield no magnetization steps which confirms the observation made in Ref. [23]. We assume that strain-mediated coupling is dominant, because any significant charge effect will play no role due to the conductive Ti layer and the carbonized NP shells.

One should note that the kink found at ca. 110 K after oxygen plasma etching is due to a fraction of maghemite / wüstite is transformed into magnetite. Hereby, the influence of oxygen plasma etching onto iron oxide nanoparticles is similar to the thermal annealing as reported by M. J. Benitez *et al.* [94].

The results on the BTO / Ti / NP / Au sample display also magnetization jumps but with a significantly enhanced amplitude as shown in Figure 4.13(c). Our interpretation is that the embedding Au layer effectively mediates the strain produced by the BTO substrate onto the NPs and hence increases the MEC between BTO and NPs.

Second, one should note the sign of the magnetization changes and the relative amplitudes at the phase transition temperatures. Here we focus on the complete system BTO / Ti / NP / Au. With increasing temperature, at the $O \rightarrow R$ transition at around 190 K, a positive magnetization step is found for the FC curve and a negative for the FW curve. The FC curve hereby displays an about three times larger jump compared to the FW curve. Due to the first order nature of the BTO phase transitions these features exhibit a temperature hysteresis. At the $T \rightarrow O$ transition at around 280 K the FC curve shows a negative magnetization step, while the FW is basically unaffected.

In order to investigate the MEC effect at the high temperature transition of BTO (C to T phase) onto the magnetism of the NPs, the PPMS VSM Oven option was employed. The sample BTO / Ti / NP / Au was measured from 300 K to 450 K in the sequence of FW and subsequently FC and the results are displayed in Figure 4.14(a).

It can be seen that a magnetization jump is formed in FW and FC curves at
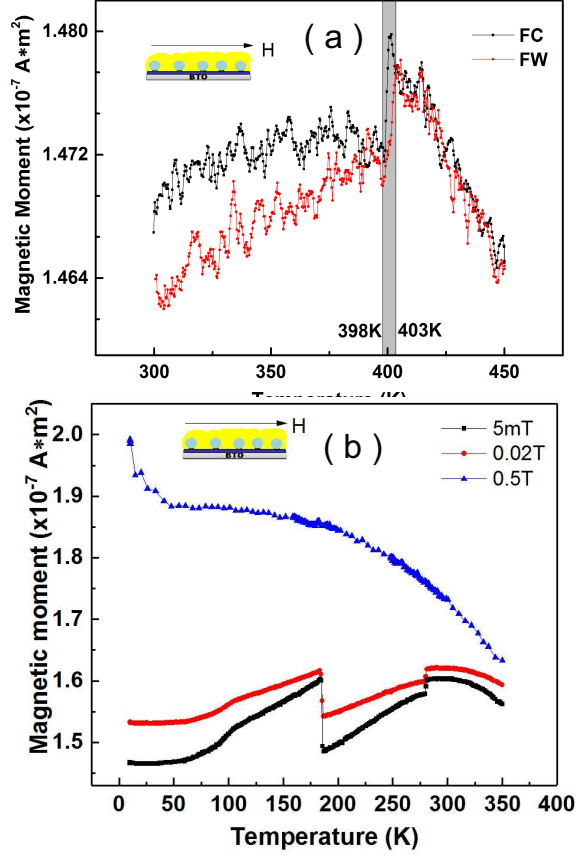
Figure 4.14: (a) In-plane magnetic moment vs. temperature during FW and during subsequent FC in 5mT for the sample BTO / Ti / NP /Au as depicted schematically in the insets (b) In-plane FC under different magnetic fields for the sample BTO / Ti / NP / Au.

around 400 K which corresponds to the BTO phase transition from C to T. Moreover, a thermal hysteresis behavior between FW and FC is observed and the gap of the hysteresis is reduced to 5 K, which is coincident with the thermal hysteresis behavior of the BTO lattice change, which can be seen in Figure 2.14.

In order to obtain a better insight into the origin of the MEC between iron oxide NPs and BTO substrate, we also investigated the magnetic field dependence of the magnetization jumps. The results are shown in Figure 4.14(b). It can be seen that the magnitude of the magnetization jumps are suppressed by the increased magnetic field and vanish under a magnetic field of 0.5 T.

To check for an anisotropy effect, we performed an analogous measurement with the magnetic field oriented perpendicular to the sample plane. The results obtained on the identical sample as in Figure 4.13(c) are shown in Figure 4.13(d). One finds an overall much smaller amplitude of the magnetization jumps. In addition, the signs of the magnetization steps are reversed.

To understand the observed effects one should note that the magnetoelastic energy gives rise to an uniaxial anisotropy which can be expressed as $\Delta E =$ (-$3/2)\lambda\Delta\sigma sin^2\theta$ [16, 96], where λ is the effective magnetostriction coefficient of the NPs, σ is the induced effective strain and θ is the angle between the measured magnetic moment and the σ-axis.

It can be deduced that if the compressive or tensile strain is abruptly increased, θ will tend to be 90° or 180° in order to minimize the anisotropy energy. Furthermore, the magnetization projection onto the in-plane and out-of-plane direction will increase or decrease causing an increase or decrease of the magnetization, correspondingly.

Taking the $O \to R$ phase transition for an example, the a(b) axis lattice parameter changes abruptly from 4.012 Å to 3.998 Å leading to an in-plane contraction of $\varepsilon_{ab} = \frac{1}{2}(\varepsilon_{xx} + \varepsilon_{yy})= 0.18\%$, where ε_{xx} and ε_{yy} are the xx and yy components of the strain tensor of BTO. The in-plane compressive stress transmits via the interface of the Ti/TiO$_2$ layer and the Au matrix onto the NPs. This causes the increase in magnetization of the in-plane component via changing the direction of magnetization easy axis. The relation between strain and magnetism becomes more complex at the $O-T$ transition, because the twinning domain state occurring at this transition results in an randomly distributed and hence in total smaller strain [70, 93].

The strain anisotropy energy effect was further investigated by the temperature dependence of the ratio of the remanent magnetization (M_r) to the saturation magnetization (M_s) and coercivity (H_c).

The magnetic hardness, M_r / M_s, (sometimes also referred as "squareness" of the hysteresis loop) is a quantitative measure of magnetic anisotropy, but also of the magnetization reversal mode (i.e. domain wall motion vs. coherent or incoherent rotation) [97]. Here we can assume that the reversal mode inside the NPs will stay unchanged, i.e. the reversal will always occur via rotation of the superspins of the NPs [24]. Therefore the hardness value will yield information on changes of the anisotropy.

Figure 4.15(a) displays four examples of hysteresis loops for the sample BTO/Ti/NP/Au
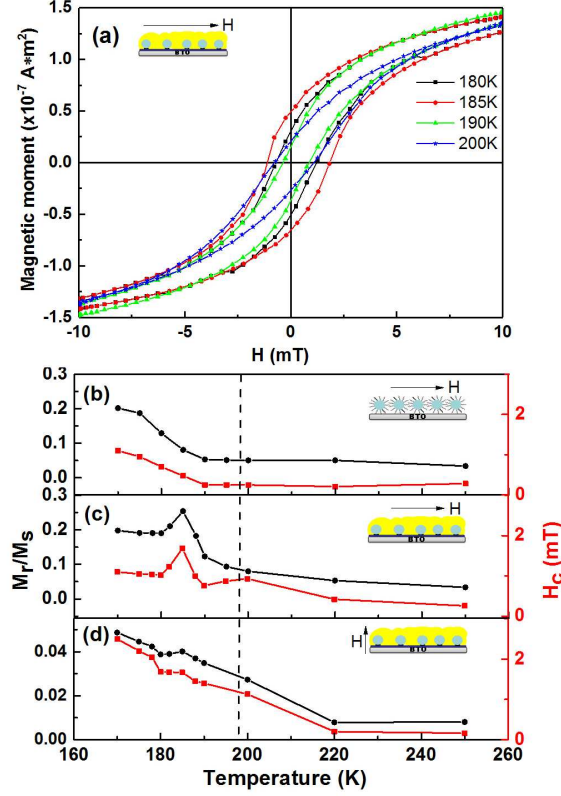
Figure 4.15: (a) In-plane zoomed-in hysteresis loops of the sample BTO / Ti / NP / Au above and below the $O-R$ phase transition measured in cooling direction. (b-d) Values of magnetic hardness M_r / M_s (black circles) and coercivity H_c (red squares) vs. temperature obtained from in-plane hysteresis loops (b-c) on the sample BTO/NP (b) and BTO/Ti/NP/Au (c). Panel (d) shows the corresponding out-of-plane data for the sample BTO/Ti/NP/Au. The dashed line marks the Néel temperature of bulk FeO.

above and below the $R - O$ phase transition measured in cooling direction with in-plane geometry. From such loops we extracted both the hardness and the coercivity H_c, as function of temperature (Figure 4.15(b-d)).

The MEC effect at the $R - O$ phase transition at about 185 K can be clearly seen in Figure 4.15(c) as a peak in both the hardness and the coercive field. The sample and the measurement geometry (in-plane field) are hereby the same as for Figure 4.13(c). The increase in the hardness means that the MEC to the BTO induces an additional magnetic anisotropy in the NPs. The comparison to the results with the perpendicular geometry shows that the induced anisotropy direction lies preferentially in-plane as only a slight jump is observed in the perpendicular case at this temperature.

One should note that also other effects might give rise to a temperature dependent change of the anisotropy. One is the exchange bias (EB) effect [98]. Our NPs are composed of ferrimagnetic maghemite and magnetite and antiferromagnetic wüstite and it was previously shown that comparable particles exhibit an EB effect below the Néel temperature of wüstite [94]. Therefore we have performed analogous measurements on the reference system BTO/NPs. The results are shown in Figure 4.15(b). One finds that below about 198K the hardness and coercivity increases with decreasing temperature as expected for an EB effect, but no peak is observed. Therefore we conclude that the peak in Figure 4.15(c) is due to MEC coupling between NPs and BTO.

Besides the anisotropy change induced by temperature, an anisotropy change caused by an electric field can be found. Magnetic hysteresis loops with simultaneous application of electric field of $E = 0$ kV/cm and ± 3.6 kV/cm were performed using the regular MPMS DC option with a special sample holder. Measurements of the M-H curves were performed at 300 K and 5 K, respectively.

The data is shown in Figure 4.16. The hysteresis loops at different electric fields at 300 K are shown in Figure 4.16(a). A typical superparamagnetic behavior is observed. No modification of the magnetization with respect to the applied electric field is observed. Both M_r and H_c keep the same value for the conditions of $E = 0$ kV/cm, +3.6 kV/cm and -3.6 kV/cm. The hysteresis loops at different electric fields at 5 K are shown in Figure 4.16(b). Both M_r and H_c change dramatically after the electric field application. The application of the electric field leads to a increase of the coercivity of 26.3 %. The hardness is increased from 0.47 to 0.88.

The magnetic moment as function of the applied DC electric field at room temperature can be seen in Figure 4.17. In order to maximally saturate the BTO substrate, a 0.1 mm thick BTO substrate is used in this measurement. Other samples are prepared on 0.5 mm thick BTO substrates. As seen from the figure, a typical butterfly shaped curve was obtained as expected from in-plane strain mediated MEC in ME composites [99]. This indicates that the magnetization of the iron oxide NPs follows the strain varied during the electric field application.

MEACS was measured on the same SQUID magnetometer with an additional upgrade implemented as described in section 3.6.

So far, the observed effects are due to structural phase transitions of the BTO
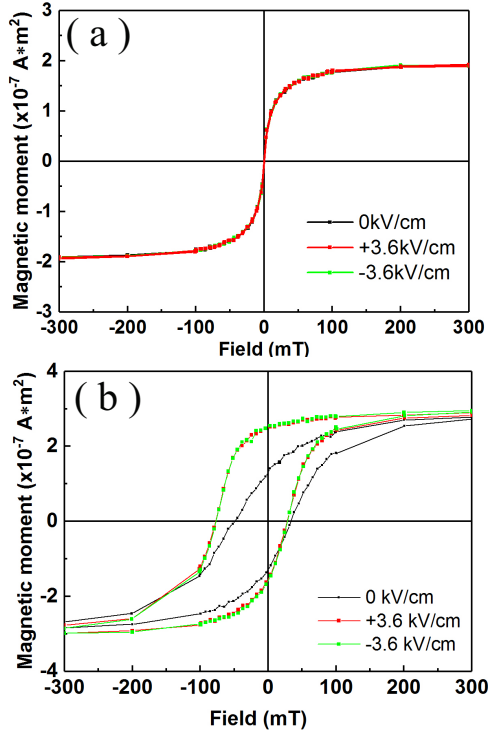
Figure 4.16: (a) Hysteresis loops of BTO / Ti / NP / Au as function of magnetic field for different applied electric fields at 300 K. No change in the magnetic behavior is found for the different electric fields at this temperature. (b) Hysteresis loops of BTO / Ti / NP / Au at different applied electric fields at 5 K. The electric fields are applied in the order of 0 kV/cm, +3.6 kV/cm and -3.6 kV/cm.

substrate. In what follows, we demonstrate that the magnetization of the Au / BTO / Ti / NP / Au system (with a thin BTO substrate) can be influenced by an AC electric field.

A clear evidence of a true MEC in contrast to possible artifacts is provided by probing the converse ME effect using MEACS [91].

The real and imaginary parts of α_{ME} as a function of temperature for various electric field amplitudes and frequencies are displayed in Figure 4.18. The sample, Au / BTO / Ti / NP / Au, was measured upon cooling while a constant small 5 mT bias magnetic field is applied to provide a magnetic alignment of the NPs.

Figure 4.18(a) was probed under an AC electric field with an amplitude of $\pm$ 3.2 kV/cm and frequency of 1 Hz. The real part of α_{ME} shows two clear jumps in the BTO phase transition regions at 190 K and 280 K. Deep inside each phase the MEACS signal, being a direct probe of the MEC strength, is approximately constant. This is expected because inside a phase only a negligible change of strain occurs by
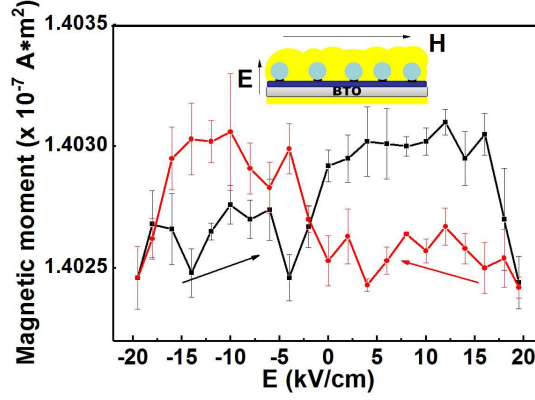
Figure 4.17: Magnetic moment vs. applied electric field of sample Au / BTO / Ti / NP / Au at 300 K and 5 mT. The black square points were measured with increasing DC field from -20 to +20 kV/cm while the red circles were measured in reversed sequence.

lattice expansion only. However, near the BTO phase transitions a large change of the MEC and hence a jump in the MEACS signal is observed due to the step-like transformation of the BTO lattice parameters, the change in the domain structure and consequently the change in the BTO surface morphology. The imaginary part of α_{ME} is constantly zero in the measured temperature range because under such low frequency, there is nearly no delay between the incoming and outgoing signal and almost zero dissipation through the sample.

The same sample was measured with an increased frequency of 9 Hz while other parameters were kept constant (Figure 4.18(b)). Both MEACS coefficients become more noisy and the two steps in the real part of α_{ME} become less obvious. One possible explanation is that while the lock-in technique only allows the signal of the selected frequency to be received, the strain generated by the BTO phase transitions has a frequency dependence that does not follow the electric field.

Under the larger frequency of 9 Hz, the imaginary part of α_{ME} starts to deviate from zero and the deviation become larger when the frequency is increased to 19 Hz which is shown in Figure 4.18(c). In principle, the imaginary part of α_{ME} indicates the delay and dissipation in the sample. The increasing nonzero value of the imaginary coefficient indicates an increasing dissipation as the frequency increases.

A smaller electric field strength causes a smaller amplitude of the steps in real part of α_{ME} and a smaller nonzero value in imaginary part of α_{ME}. This is found when the electric field strength decreased to 1.8 kV/cm and the frequency decreased to 1 Hz and 9 Hz (Figure 4.18(d) and (e)).

To systematically investigate the effect of frequency and amplitude of the AC E-field onto the real part of α_{ME}, the frequency and amplitude dependency of the real part of α_{ME} is measured which is shown in Figure 4.18(f) and (g), respectively.
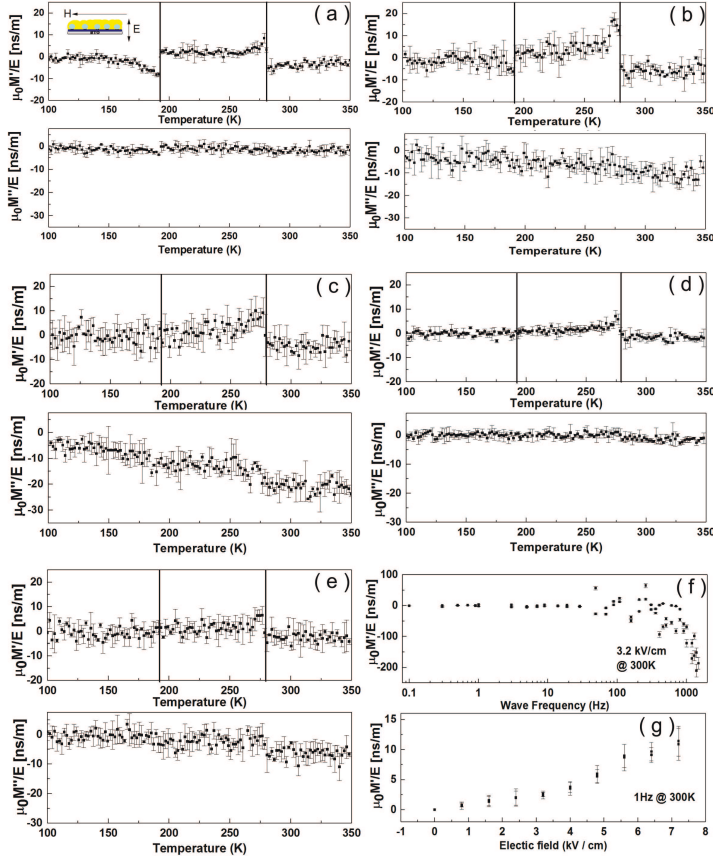
Figure 4.18: The real and imaginary parts α_{ME} vs temperature measured in a AC E-field with different frequencies f and E-field amplitude E_{max} and a constant magnetic field of 5 mT, (a) at E_{max}=3.2 kV/cm and f=1 Hz, (b) at E_{max}=3.2 kV/cm and f=9 Hz, (c) E_{max}=3.2 kV/cm and f=19 Hz, (d) E_{max}=1.8 kV/cm and f=1 Hz, (e) E_{max}=1.8 kV/cm and f=9 Hz, (f) the real part α_{ME} as a function of frequency measured at 300 K and E_{max}=3.2 kV/cm, (g) the real part α_{ME} as a function of E-field strength measured at 300 K and 1 Hz. The two black lines at 192 K and 280 K in figure (a) to (e) indicate the R-O and O-T phase transitions of the BTO substrate. The measuring geometry is shown as the inset in (a). Both real and imaginary part α_{ME} are shown in the same scale for better comparison.

Both curves were measured from zero to maximum value first, and then decreased back. At low frequency, the real part of α_{ME} is almost frequency independent and very close to zero. The real part of α_{ME} decreases to negative values above 300 Hz (Figure 4.18(f)). In the electric field amplitude dependence seen in Figure 4.18(g), the ΔM is the absolute value of the difference between the coefficients obtained at

each positive and negative electric field. As expected, the coefficient increases as the electric field frequency or strength increases.

Moreover, we have measured two reference samples, i.e. one with a bare BTO substrate contacted with a bottom and top electrode (sample Au/BTO/Au), and one with only a silicon substrate with NPs (sample Au / Si / NP / Au). Both samples show only white noise without any specific features (see Figure 4.19). The results rule out any MEACS signal from the BTO substrate and from the NPs alone, respectively.
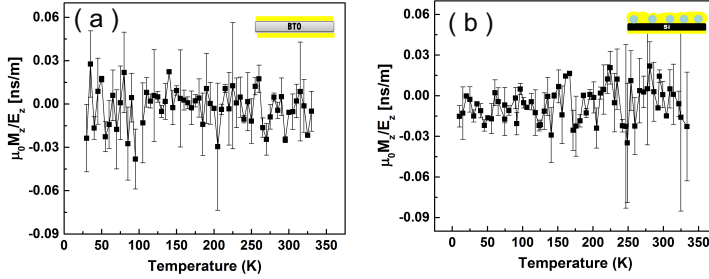
Figure 4.19: ME coefficient of (a) Au / BTO / Au and (b) Au / Si / iron oxide NPs / Au systems in dependence of temperature measured at $f = 1$ Hz and E_{max} = 4 kV/cm after ME field cooling. The samples stacking are displayed as the diagrammatic drawing inside each figure.

We also measured, with the same protocol, but with a larger saturating constant magnetic field of 100 mT, and found no jump. This is in accordance with the fact that a larger Zeeman energy stabilizes the NP magnetization along the field direction which results in a smaller influence of the ME effect.

The real and imaginary parts α_{ME} as function of magnetic field are shown in Figure 4.20. The measurements were taken at 300 K, 270 K and 180 K which corresponds to the T, O and R phases of BTO, respectively. The measurement started from zero magnetic field and then was increased to +0.5 T, reduced to -0.5 T and finally swept back to zero. Both parts of α_{ME} only show a field dependence in the region between 150 mT and -150 mT. The data beyond that region is not shown in order to clearly show the region of interest.

The measurement at 300 K shows a hysteresis behavior of the real part of α_{ME} (Figure 4.20(a)). The maximum and minimum values of the coefficient occur at +7 mT and -7 mT, respectively. The coefficient decreased to zero when the magnetic field increased beyond these fields. The imaginary part of α_{ME} is zero within the entire magnetic field range.

Figure 4.20(b) shows the α_{ME} at 270 K, which is corresponding to the O-phase of BTO. A less obvious hysteresis behavior of the real part of α_{ME} between 50 mT and -50 mT is observed, while the maximum and minimum coefficient happen at +8 mT and -8 mT. Moreover, one should note that the amplitude of the real part of α_{ME} is smaller than that in the T-phase indicating a temperature dependent real
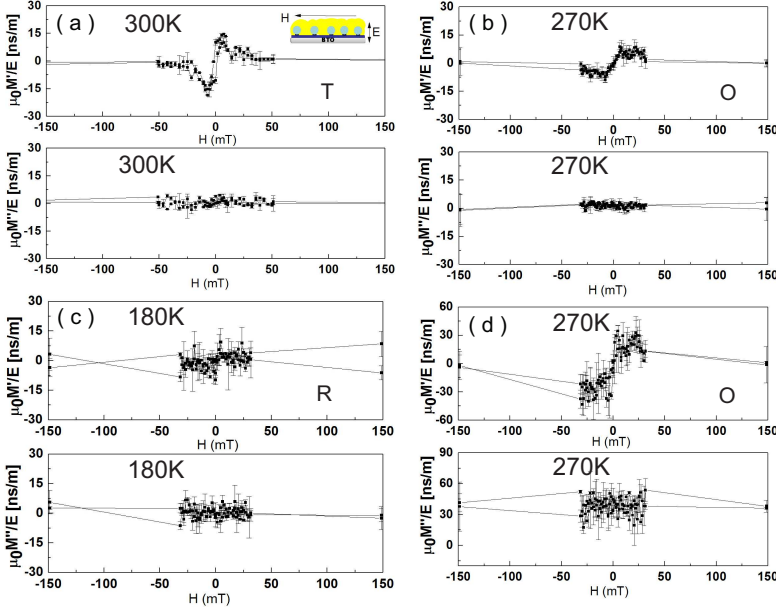
Figure 4.20: The real part and imaginary part of α_{ME} vs. magnetic field measured in an AC E field with amplitude E_{max}= 3.2 kV/cm, frequency f=9 Hz and a constant magnetic field of 5 mT, (a)at 300 K (b) at 270 K (c)at 180 K (d)at 270 K with an AC electric field of E_{max}=3.2 kV/cm and f=199 Hz, The phases of BTO in every measurement are marked. The schematic of the sample used in this measurement is represented as the inset in (a).

part of α_{ME}. The imaginary part of α_{ME} still stays constantly zero.

After decreasing the temperature to 180 K, corresponding to the R-phase of BTO, the real part of α_{ME} shows an nearly unobservable hysteresis and no maximum and minimum values can be found (Figure 4.20(c)). The imaginary part of α_{ME} remains zero,which means the imaginary part of α_{ME} is temperature independent.

An AC electric field with a larger frequency of 199 HZ was applied to the sample to investigate the frequency dependence of both parts of α_{ME}. In order to simplify the figure, only measurements in the O-phase are shown while measurements in the other two phases show similar results. As the frequency increases, the amplitude of the real part of α_{ME} increases and the maximum and minimum values shift to $\pm$ 20 mT respectively (Figure 4.20(d)). The imaginary part α_{ME} shows a sizeable value of 40 ns/m. It is due to the effect of strain mediated magnetism of iron oxide NPs via magnetostriction.

The α_{ME} is expressed as [100],

$$\alpha_{ME} \propto q_1 d_1 E_{ac} \tag{4.1}$$

where q_1 is the effective magnetostrictive coefficient of the iron oxide NPs, d_1 is the

piezoelectric coefficient of the BTO substrate and E_{ac} is the applied AC E field. q_1 can be expressed as

$$q_1 = \delta\lambda/\delta H \tag{4.2}$$

where λ is the magnetostrictive strain and H is the applied magnetic field. The hysteresis response of the real part of α_{ME} can be interpreted by the magnetostrictive coefficient curve of iron oxide. For instance, the magnetostriction of an iron oxide single crystal shows an increase tendency with a diminishingly acceleration until it becomes flat after the saturation magnetic field of 30 mT is reached [100]. Mathematically, the S-shaped α_{ME} vs. H results from the first derivative of the magnetostriction curve of iron oxide and the maximum and minimum values of real part are related to the largest magnetostrictive coefficient of iron oxide. Moreover, the zero value of the real part of α_{ME} in high magnetic field is because the strain has no effect onto the NPs beyond their magnetostriction saturation field.

The gradually disappearing hysteresis and amplitude of the real part of α_{ME} as function of frequency is because of the decreased strain. The strain strength decreases as temperature decreases under the same electric field [101] which can also be confirmed by the piezoelectric property of BTO shown in chapter 2.7.1. The decreasing strain leads to a nearly vanishing ME coefficient in the R-phase of BTO.

After increasing the E-field frequency to 199 Hz, the imaginary part of α_{ME} shows a non-zero value. The situation becomes complicated, which needs further investigation, for example, the magnetic field shift of the maximum and minimum values of the real part of α_{ME}.

4.2.2   Analysis of the magnetic depth profile

Polarized neutron reflectivity (PNR) measurements were performed to study the magnetic depth profile of the iron oxide NP monolayer of the Au / BTO / Ti / NP / Au sample. The microscopic magnetic profile is able to provide information on how the electric field and strain manipulate the spin structures of the NPs. PNR measurements were carried out at 300 K. The measurement sequence is schematically shown in Figure 4.21. The PNR data were measured at two magnetic fields: one is the coercive field of +3.3 mT and the other one is the saturation field of +0.98 T.

The magnetic field started from zero to +0.98 T indicated as red arrows. There the PNR data at saturation was recorded. In order to investigate the electric field manipulation of the magnetization of the NPs, an electric field connection was designed to apply E-field in the sequence of 0 kV/cm, +5 kV/cm and finally -5 kV/cm. Afterwards, the magnetic field was switched to -0.98 T and finally returned to the +3.3 mT. There PNR data was recorded at the guide field and measurements with the same sequence of E-field application were performed. Moreover, PNR was measured in the channels R_{++} and R_{--}. The spin flip channels were skipped since no signal was observed.

The PNR measurements performed at 300 K without electric field are displayed in Figure 4.22(a). The data shows thickness oscillations up to the third order. The difference between R_{++} and R_{--} channels are due to the magnetization of iron oxide
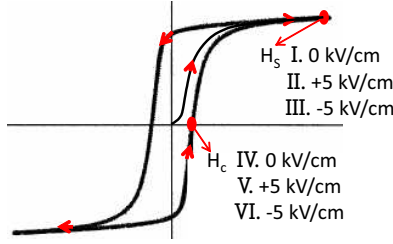
Figure 4.21: Schematic diagram of the measurements sequence, H_S indicates the saturation magnetic field while H_c indicates the coercive magnetic field. The magnetic field evolution is marked as red arrows. Different *E*-fields were applied at each magnetic field. Six measurements were performed according to the number I - VII. The experimental value of $H_c = 3.3$ mT and $H_s = 0.98$ T.

NP layers at room temperature. The ratio between the difference and the sum of two non spin-flip channels, namely the asymmetry, is displayed in Figure 4.22(b). Nearly 10 percent of the total signal is contributed by the magnetic signal from the NPs.

The software Genx was used to fit the reflectivity of both channels to deduce the magnetic profile of iron oxide NPs. The default setting of Genx is a thin film system. Each layer is defined by several parameters: thickness (Th_i), roughness (Sig_i), nuclear scattering length density ($nSLD_i$), and two additional parameters, i.e. magnetic scattering length density ($mSLD_i$) and magnetic angle ($Magangle_i$). Worth to mention is that the roughness of each layer is indicated as the slope of the curve, e.g. a sharp interface with zero roughness is represented as a steep line with a infinitely large slope, while large roughness is represented as an oblique line with a certain slope.

The sample BTO / Ti / NP / Au is regarded as a composition of a infinite thick BTO layer, a Ti layer, a iron oxide layer, a Au layer and an ambient environment. According to the macroscopic magnetic measurements and STEM investigations of the sample, the reference value of the stoichiometry and thickness of each layer are determined, hence the reference values of nSLD and mSLD are calculated depending on the stoichiometry. The schematic of the sample model is shown Figure 4.23(a). Minimum and maximum values of 25% away from the reference value are defined to give the boundaries for the fit.

However, one should note that, the default setting of Genx is thin film system with homogenous SLD and hence not suitable for NPs. Therefore, an own model, namely a spherical body model, was employed to improve the fit. In this model, NP layers are sliced into many thin layers and each layer is described by parameters as a conventional thin film. But instead of letting them change independently, both nSLD and mSLD of the slice layers vary with the volume function of a spherical body.

Another point to note is that Genx is likely to produce a better fitting with a
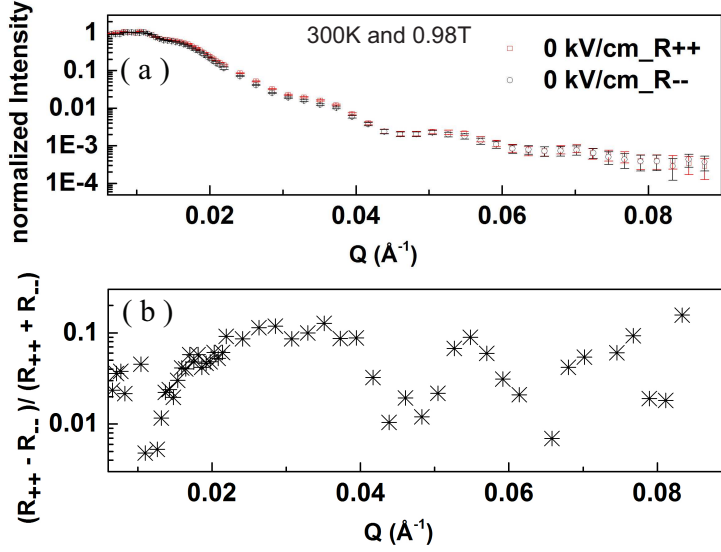
Figure 4.22: (a) PNR data of the BTO/Ti/NP/Au sample measured at 300 K in R_{++} and R_{--} channels with an applied saturation magnetic field of 0.98T. (b) Asymmetry vs. Q

lager number of parameters. However the raw data does not have too many distinct oscillations. Therefore, in order to avoid impractical and unrealistic fitting, some simplified assumptions are made.

For example, instead of separate single phase (γ-Fe_2O_3, Fe_3O_4, FeO etc.), an integrated composition (FeO_x) was used for the iron oxide NPs. Moreover, the STEM results show that the Au layer reaches about half of the particle diameter into the NPs layers. Hence the composition of each slice is modeled as $0.7((Fe_2O_3)_{0.8}$ $(Fe_3O_4)_{0.15}$ $(Fe_xO)_{0.05}) \cdot 0.3$ Au. The same treatment applied on TiO_x layer, the composition of the TiO_x layer was modified as $0.8(Ti) \cdot 0.2(TiO_2)$.

The PNR data of the R_{++} and R_{--} channels under the saturation magnetic field together with the corresponding fit are displayed in Figure 4.23(b). The fitting represents the data in a good agreement with a FOM factor of 0.033. The scattering length density (SLD) with respect to the layer thickness obtained from the fitting is plotted in Figure 4.23(c). The fitting gives a result as following: a 7.50 nm Ti + TiO_2 layer with nSLD of $-0.172 \cdot 10^{-6} Å^2$ (the reference nSLD of Ti and TiO_2 is $-1.925 \cdot 10^{-6} Å^2$ and $0.621 \cdot 10^{-6} Å^2$, respectively), a 25.1 nm NP + Au with a nSLD of $3.23 \cdot 10^{-6} Å^2$ and a peak mSLD of $0.38 \cdot 10^{-6} Å^2$, and a 3.67 nm pure Au layer with a nSLD of $4.97 \cdot 10^{-6} Å^2$ (the reference value of Au is $4.662 \cdot 10^{-6} Å^2$). The sawtooth shaped SLD curve indicates that the iron oxide slice layer has a small roughness (1.34 Å).

Both nSLD and mSLD show that at the initial state, the high roughness of BTO
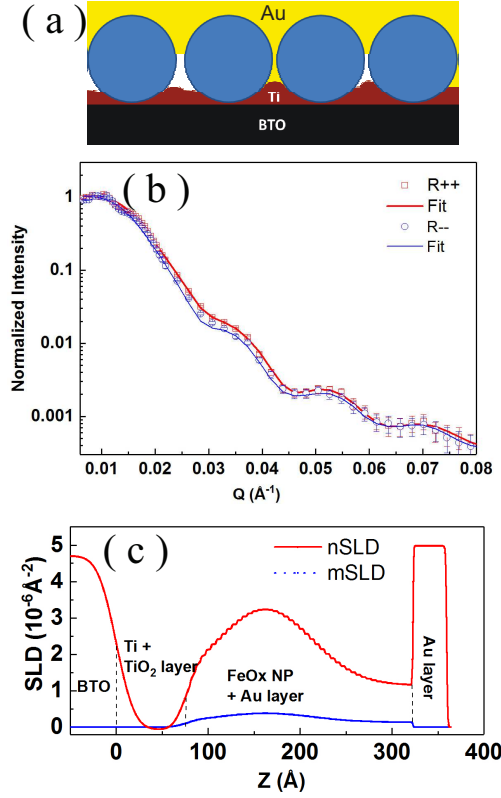
Figure 4.23: (a) The schematic spherical fitting model. (b) PNR data and the fitting of the BTO / Ti / NP / Au sample at 300 K at saturation field. (c) nSLD and mSLD profiles obtained by the fit.

is reflected by the small slope in the thickness range from -50 Å to 0 Å ($Z = 0$ indicates the interface between BTO and Ti layer), leading to the same condition of Ti layer which was directly grown on the BTO substrate. Meanwhile, the Au layer shows a relatively smooth surface on a average level. We assume that during the deposition of Au atoms using MBE method the gaps between the neighboring NPs are filled. Although microscopically, some gaps are not fully occupied, the other area are quite flat as indicated in Figure 4.13(c), on a average level, a relative flat surface is given by both XRR (see Figure 4.8) and NR. The spherical body model estimates the thickness of Ti layer to be 7.50 nm which is close to the observed thickness by STEM. The nSLD of iron oxide layer obtained from fitting is only half of the nSLD value of bulk Fe_2O_3 or Fe_3O_4 ($nSLD_{Fe_2O_3} = 7.26 \cdot 10^{-6} Å^2$, $nSLD_{Fe_3O_4} = 6.97 \cdot 10^{-6} Å^2$). The results suggest that the NPs did not fill the space completely, and the nSLD of NP layers is diluted by the space between the NPs.

In the following investigation of the E-field effect onto the magnetic profiles of

iron oxide NPs, the thicknesses and nSLD values of BTO, Ti + TiO$_2$ layer and NP + Au layer and Au layer obtained from last fitting are fixed since these values should be kept constant. Because the E-field will change the roughness of the BTO substrate and consequently the roughness of other layers, the roughnesses of every layer and mSLD of iron oxide are kept free in the following fitting process.
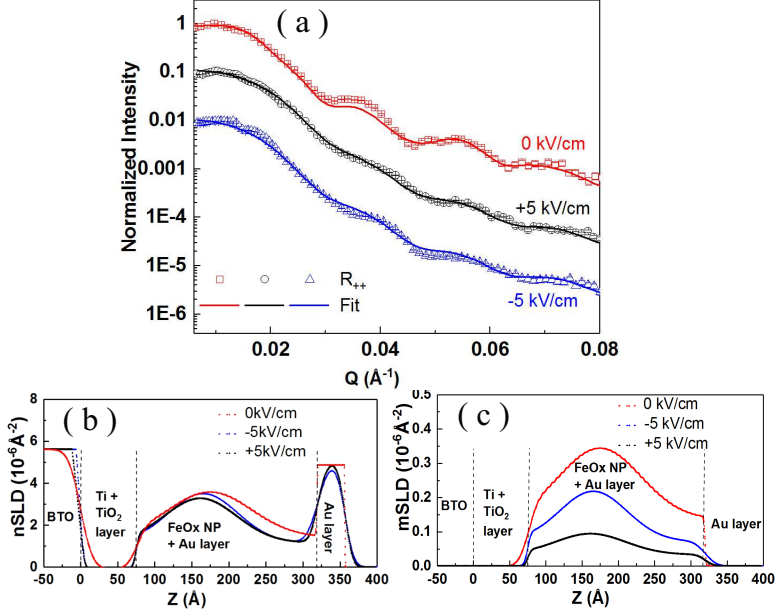
Figure 4.24: PNR data of the BTO / Ti / NP / Au sample at 300 K at coercive field. (a) Reflectivity and the fit for an electric field of 0 KV/cm, +5 KV/cm and -5 KV/cm (b) nSLD obtained from the fit (c) mSLD obtained from the fit. The dashed lines in (b) and (c) indicate the interfaces of layer.

The PNR data at coercive field with zero E-field, +5 kV/cm and -5 kV/cm are shown in Figure 4.24(a). Both non spin-flip channels were measured and fitted simultaneously, while only the R$_{++}$ channels are shown for simplicity. The R$_{++}$ data at +5 kV/cm and -5 kV/cm are divided by 10 and 100, respectively, for a better visibility.

The nSLD and mSLD of each layer are plotted in Figure 4.24 (b) and (c) (the values of fitting parameters are listed in the appendix G). The evolution of nSLD and mSLD after applying an E-field show that the BTO substrate flattens and so does the Ti layer. However, the interface of the NP layer become rough since the sawtooth disappears in the SLD curve and the Au layer becomes rough as well. The roughness change after electric field application can be interpreted as that the Au layer fills the rough surface and show a flat surface. However, after electric field application, the reconfiguration of the BTO surface will relocate the NPs slightly.

The Ti layer is too thin to fill the rough surface of the BTO substrate and hence changes its roughness depending on the BTO surface. The mSLD shows that at the coercive magnetic field, the E-field will suppress the mSLD of the iron oxide NPs. It shows that the large roughness of the Au layer is the major reason for the quick dying out of oscillations and the difference between the PNR data under different E-field. The difference in the magnetic profiles is weak.
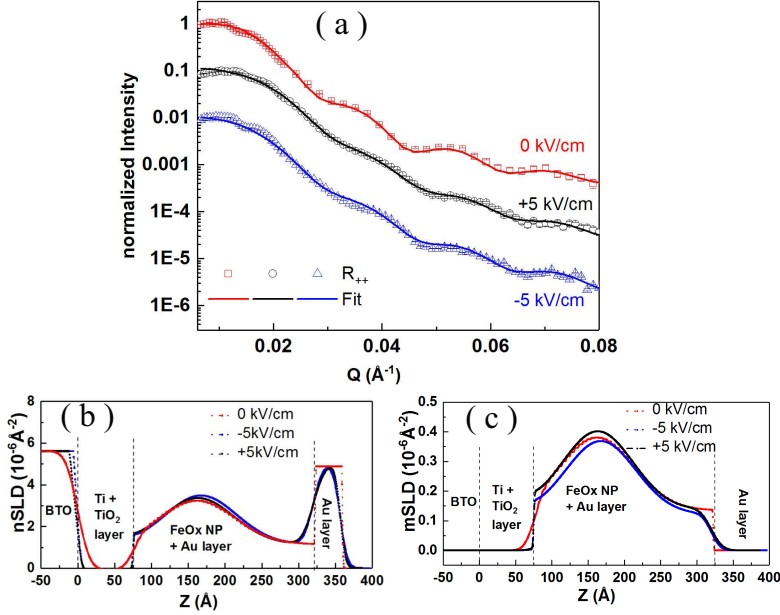
Figure 4.25: PNR data of the BTO / Ti / NP / Au sample at 300 K at saturation field. (a) Reflectivity and the fit for electric field of 0 KV/cm, +5 KV/cm and -5 KV/cm (b) nSLD obtained from the fit (c) mSLD obtained from the fit. The dashed lines in (b) and (c) indicate the interfaces of each two layers

The PNR data and the fitting under the saturation magnetic field with different electric field are shown in Figure 4.25. In the spherical model, all the parameters from the last fitting were also fixed except the mSLD of the NP + Au layers. As seen from the Figure 4.25(b) and (c), the same conclusions can be obtained in terms of roughness and nSLD as before for the coercive magnetic field. The mSLD of the NP layer at different electric fields shows only negligible differences. This is because the electric field can hardly influence the spin structures of NPs when they are saturated.

The default model from Genx was also used to fit the raw data. In this model, NP are regarded as a magnetic layer by the default setting of Genx the detailed description of the model and fitting are presented in the Appendix F. The FOM factors of the default model and spherical body model are listed in Figure 4.1, the spherical body model shows a better represent of the raw data.

Table 4.1: Factor of merit (FOM) of every PNR fitting

E field (kV/cm)	Model	Coercive ($\times 10^{-3}$)	Saturation ($\times 10^{-3}$)
0	Default	10.8	2.9
	Spherical	8.6	3.3
+5	Default	7.3	6.6
	Spherical	7.1	5.9
-5	Default	8.9	5.7
	Spherical	5.2	4.8

In summary, differences in the PNR data with respect to the applied electric field are observed at both coercive and saturation magnetic fields. The intensity change is mostly related to the increased roughness of the interfaces between layers. The modified spherical body model matches the sample geometry better and gives a better FOM factor than the default model. The prediction of the E-field effect modification of the magnetization of NPs via the spherical body model is still challenging. E-field easier to modify the in-plane magnetization component of the NPs at coercive fields than at saturation fields.

4.2.3   Discussion and outlook

The investigations of the system of iron oxide NPs coupled to BTO substrates (or films) show several interesting results. Obvious MEC effects and particularly, the modification of magnetism of iron oxide NPs by electric field shows fascinating effects. Although strain is evidenced to be the primary mechanism responsible for the observed MEC effect, the details of the microscopic mechanisms have to be eliminated. In this section, a detailed understanding of the strain induced MEC are discussed as follows.

In principle, the MEC process can be divided into three steps. The induction of strain from the BTO single crystal, the transformation of strain through the Ti and Au layers to the NPs, and finally the magnetic response of the NPs.

First, consider the induction of strain from the BTO. It is confirmed that the strain results from the BTO substrates via domain formation and lattice distortion. Both the measurements using laser reflection pattern (see Figure 4.4) and x-ray diffraction (see Figure 4.5) provide information of domain and lattice changes in dependence of the electric field and temperature, respectively.

The connection between strain and the MEC effect at 300 K is represented by the butterfly-shaped M-E curve as shown in Figure 4.17. The comparison between the temperature dependent piezoelectric coefficient d_{33} and the temperature dependent ME coefficient is displayed in Figure 4.26. d_{33} quantifies the volume change of BTO under the application of an electric field. The ME coefficient follows the behavior of the temperature dependent d_{33} of BTO single crystals in T and O phases [75] and is pronounced in proximity to the structural phase transition of the BTO substrate. This fact indicates that the strain induced MEC is present at the entire temperature
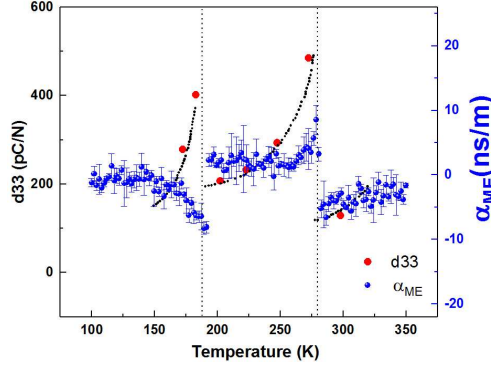
Figure 4.26: Temperature dependent piezoelectric coefficient d_{33} of the (001)-oriented BTO crystal [75] and magnetic moment of the sample BTO / Ti / NP / Au. The red dots are measured d_{33} of BTO, the black dots are calculated values for single-domain BTO crystals and the blue circles represent the ME coefficient of the sample. The dashed black lines mark the phase transition temperatures of BTO single crystals.

range and is especially pronounced at the BTO phase transition temperatures. The different behavior between d_{33} and ME coefficient at O - R phase transition might be due to the unpredicted domain deformation.

The corresponding strain from the lattice distortions in each axis can be represented by the strain tensor ε_{xx}, ε_{yy} and ε_{zz}. By symmetry, in-plane strains consist of two components, one is the even parity $\varepsilon_{\alpha} = 1/2(\varepsilon_{xx} + \varepsilon_{yy})$, which indicates the in-plane area change, while the other is $\varepsilon^* = 1/2(\varepsilon_{xx} - \varepsilon_{yy})$, which corresponds to an in-plane distortion away from square symmetry [102, 103, 104]. The observed magnetization anomalies occur at the phase transition temperatures of the BTO substrate (Figure 4.13), indicating that they are caused by the lattice distortions associated with the transitions.
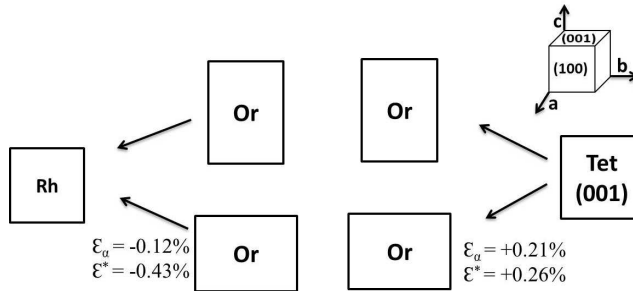
Figure 4.27: Schematical (001) in-plane lattice distortion of BTO at the phase transitions. The inset shows the reference axis of the BTO lattice.
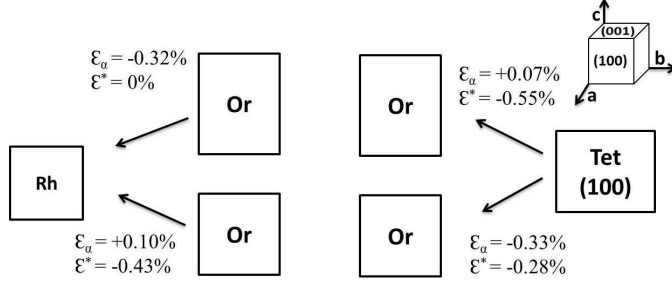
Figure 4.28: Schematical (100) in-plane lattice distortion of BTO at the phase transitions. The inset shows the reference axis of the BTO lattice.

The estimated (001) in-plane symmetry strains at the phase transitions are displayed in Figure 4.27. When BTO undergoes from T to R phase, the (001) in-plane lattice undergoes a expansion of 0.21% associated with a 0.26% distortion away from square symmetry. The subsequent transition from R to O phase induce a 0.12% in-plane area contraction accompanied with a -0.43% distortion away from square symmetry.

The lattice structure of the (100) plane of tetragonal BTO is more complicated than that of the (001) plane, because the lattice in (100) plane is not unique in the T phase [104]. The relevant values in the two phases are shown in Figure 4.28.

Since a domain twinning effect can easily be generated in BTO during the thermal cycle, one cannot eliminate the possibility of the thermally induced substrate cracking effect which can relocate the NP position. Since a cracking effect will cause irreversible magnetization anomalies [104], this can be excluded in our sample over many thermal cycles. The magnetic moment of the sample as function of temperature under various electric fields are displayed in Figure 4.29. The steps in the magnetic moment at the BTO phase transitions show the reversible behavior after several thermal cycles indicating that the MEC is intrinsic instead of the result of cracks.

Accompanied with lattice distortion, ferroelectric domains show different structures at different phases. In the T phase, BTO is a mixture of domains with the polarization pointing out of plane (c-domains) and in plane (a-domains) with the net polarization along the [001] direction being a coexistence of 90° and 180° domains [105]. In the O and R phase, the polarization is in the direction of [110] and [111], respectively. In the O phase, the polarization has the same probability to point to one of the twelve [110] directions. The adjacent ferroelectric domains are arranged with a angle of 60°, 90° and 180°. In the R phase, the polarization has eight possible directions along [111] directions and the domains with angles of 71°, 109° and 180° are formed [106].

Overall, in the (001) plane, a biaxial tensile strain was induced from the lattice distortion at the phase transition from T to O while a biaxial compressive strain was induced at the phase transition from O to R. The type of strain is difficult
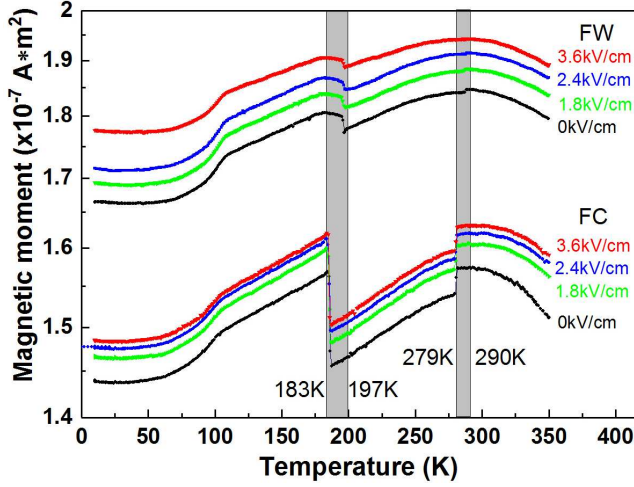
Figure 4.29: Temperature dependent magnetic moment under different electric field of the system Au / BTO / Ti / NP monolayer /Au. The measurement protocol is the same as the curves measured in Figure 4.13 and the electric field is increasingly applied at each FW and FC measurements. The black bars indicates the indicate the temperature region, where bulk BTO has first order phase transitions from T to O and O to R. To all FW curves, a value of 0.3×10^{-7} A∗m^2 has been added for a better visibility.

to analyze in the (100) plane due to the presence of two possible lattice distortion configurations. The domain structures in the T phase in both planes will reduce the strain by distorting a fraction of lattice units. The domain structures in the R and O phases are even more unpredictable due to their many more possible orientations.

Secondly, the strain transfers onto the NPs via the Ti and Au layers. Hereby, the Ti layer is necessary prerequisite for the strain mediated MEC effect. The Ti layer eliminates any interface-charge MEC mechanism as discussed in section 5.2. Meanwhile it provides the transfer path of the strain. The evidence is shown as a zero MEC versus nonzero MEC effect in Figure 4.13(a) and (b).

In order to investigate the influence of the Ti layer thickness onto the MEC effect, a reference system, which has the same geometry and preparation parameters, but with a 15.8 nm thick Ti layer was studied. The measurement protocol was kept the same as in Figure 4.13. The results shown in Figure 4.30 indicate that the magnetization jump at the T to O phase transition is nearly negligible, while the magnetization jump at the O to R phase transition is significantly reduced (1.15%) compared to the thin Ti layer sample (7.82%). This indicates that the thick Ti layer reduces the strain mediation. However, a nonzero thick Ti layer is needed to serve as mediating layer [107, 23].

The Au layer is supposed to enlarge the interface for the strain mediation. Ob-
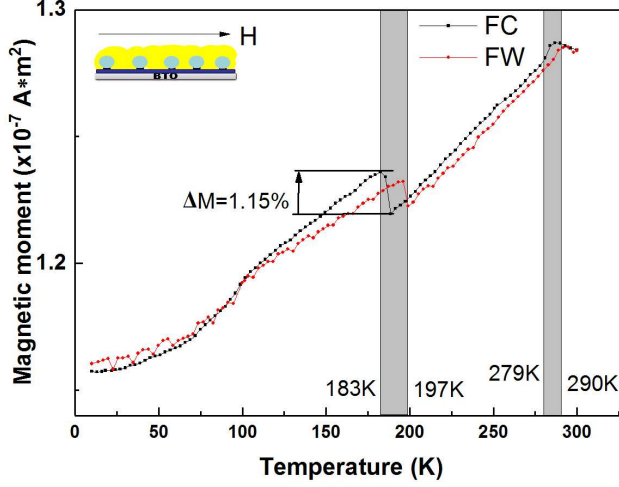
Figure 4.30: Temperature dependent magnetic moment of the reference system BTO / thick Ti (15.8 nm) / NP monolayer /Au. The measurement protocol is the same in Figure 4.13. The grey bars indicate the temperature regions of the phase transitions of BTO.

viously the MEC is significantly enhanced as shown in Figure 4.13(b) and (c). An investigation of the influence of the Au layer thickness onto the MEC effect has not been performed in this thesis, but is definitely an important step for the near future.

Thirdly, the strain onto the NPs will result in a magnetization change via its magnetostriction property. The magnetostriction vs. magnetic field for Fe_2O_3 sin-
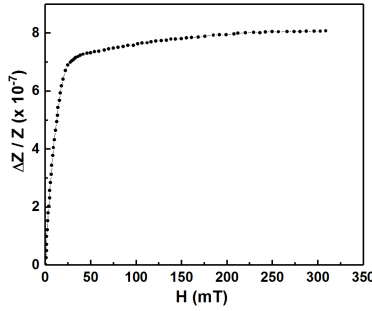
Figure 4.31: Magnetostriction of Fe_2O_3 single crystal in dependence of magnetic field at 305 K along the direction of [111], adopted from [100].

gle crystals provides a hint on how the strain affects the magnetization of the NPs. In principle, the magnetostriction property of NPs should essentially track the magnetostrictive coefficient q, which reads as $q = \delta\lambda/\delta H$, where λ is the magnetostrictive

strain and is represented as the lattice change $\Delta Z/Z$ in Figure 4.31. The figure shows the magnetostriction of Fe_2O_3 is approaching saturation around 30 mT, and consequently q will stay close to zero above 30 mT. As a consequence, the magnetization change is zero. This interpretation is evidenced by the result of magnetic field dependent MEACS coefficient which is shown in Figure 4.20.

The strain mediated magnetization change of NPs via the magnetoelastic property of iron oxide is expressed in the magneto-elastic energy equation $\Delta E = (-3/2)\lambda\Delta\sigma sin^2\theta$, which was introduced before in section 4.2.1. First, λ, the effective magnetostriction coefficient of iron oxide NPs will be discussed. Usually, the effective λ can be defined by a linear superposition of two independent longitudinal magnetostriction coefficients λ_{100} and λ_{111}, so that $\lambda = a\cdot\lambda_{100} + b\cdot\lambda_{111}$. However, since the NPs are self-assembled in a monolayer and their crystalline axes can be assumed to be randomly orientated, an assumption of isotropic magnetostriction can be made for the effective λ, which is equivalent to the magnetostriction coefficient of a polycrystalline state. For example, the magnetostriction coefficient λ for the polycrystalline magnetite at room temperature under saturation magnetic field is 35×10^{-6} [108, 109]. Maghemite exhibits the same value as magnetite, hematite has -9 $\times 10^{-6}$ and wuestite ($Fe_{0.915}O$) 8 $\times 10^{-6}$ [108]. Since the NPs being studied are multi-phase particles consisting of maghemite, magnetite and wuestite in a polycrystalline fashion and the ratio for every component in one NP is approximately 16 : 3 : 1, respectively, as indicated in section 4.2.2, the effective magnetostriction coefficient of iron oxide NPs can be estimated to be 33.7×10^{-6}.

At the T to O phase transition, a biaxial tensile strain ($\sigma > 0$) is induced and the magneto-elastic energy is reduced according to the strain energy density equation and thus the magnetic moment decreases.

In summary, the MEC effects in an artificial multiferroic heterostructure of NP monolayers and BTO substrates were observed. The results show that the magnetization of self-assembled NPs monolayers on BTO substrates can be manipulated by the variation of temperature or electric fields. At the structural transitions, the abrupt magnetization jumps are due to the deformation of lattice and domain structures of BTO. The modification of the magnetization with respect to the DC electric field shows a butterfly shape which is coincident with the piezoelectric curve of BTO single crystals.

The abrupt steps near BTO structural phase transitions shows an E field amplitude and frequency dependence, which originates from by the piezoelectric properties of BTO single crystal.

The magnetization profile under different DC electric and magnetic fields are determined by PNR, The mSLD profiles show a reduced in-plane magnetization of NPs after electric field application and the manipulation of mSLD of NPs is easier to realize at low magnetic field. This reduction of magnetization can be explained by strain induced MEC effect.

4.3   NP multilayers on BTO substrate

In order to investigate the influence of NP layer thickness onto the MEC effect, self-assembled NP multilayers were deposited on top of BTO substrates by the dropcasting method. The NP dispersion was diluted with the volume ratio of 1:10 by toluene, and then 5 μL diluted solution was dropped onto a Si substrate. The sample was treated in oxygen plasma for 5 min after drying in air for 30 min.The morphology of the as-prepared samples were characterized by SEM (Figure 4.32). The result shows that the NP multilayers sample consists of 10 - 30 layers which are arranged in a hexagonal lattice. However, the SEM result shows that NPs self-assembled by dropcasting do not form a uniform sample on a large area. In order to get an averaged information about the arrangement of the NPs, the sample morphology was studied with GISAXS (Figure 4.33(a)).
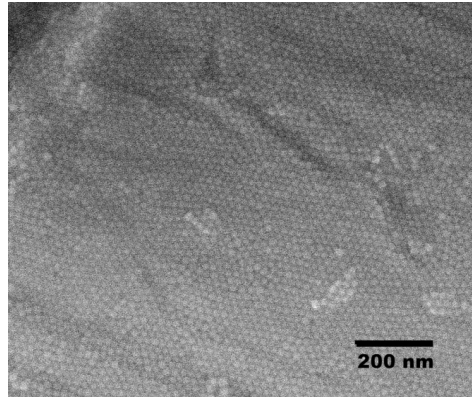
Figure 4.32: SEM image of BTO / Ti / NP multilayers.

The GISAXS measurement actually includes two measurements at the same time: the GISAXS measurement above $Q_z = 0.5$ nm^{-1} and the SAXS measurements below. The reason for the SAXS pattern is that the x-ray beam penetrated through the BTO substrate at the edge. One finds that by removing the NPs on the edge of BTO substrate, or block the penetrated x-ray beam, will eliminate the SAXS pattern. The SAXS pattern suggest a hexagonal arranged NP.

The Bragg reflections in the GISAXS pattern are superimposed by blurry powder rings, resulting from the scattering of the x-rays in the carbon tape in front of the 2-D detector. The carbon tape is used to fix the foils at the exit of the detector tube. Nevertheless, the 2d-Bragg rods were successfully indexed assuming a two-dimensional close-packed hexagonal lattice with a lattice constant of a = 22.08 $\pm$ 0.62 nm. The observed stripe positions and calculated positions based on the NP diameter match well, confirming a hexagonal arrangement. It is also in good agreement with the SEM observation depicted in Table 4.6(d). A line cut at Q_z = 0.65 nm^{-1} is shown in Figure 4.33(b). The lateral correlation of the NP array
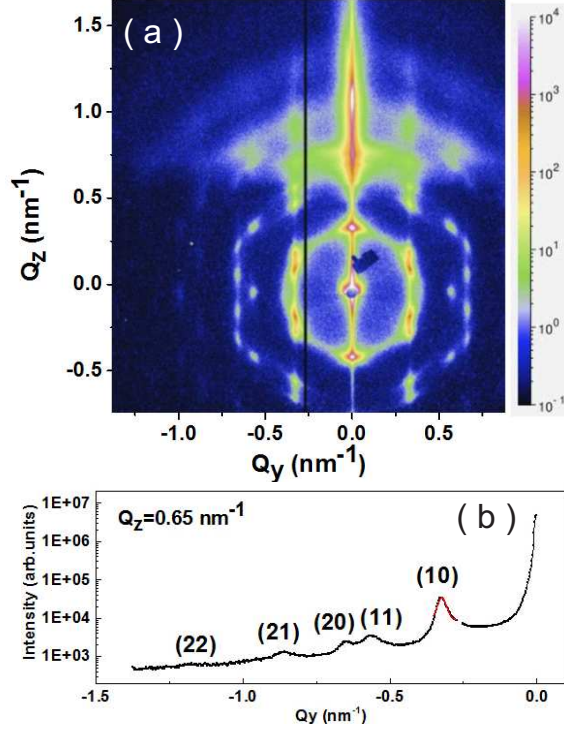
Figure 4.33: (a) GISAXS pattern of iron oxide NP multilayers self-assembled on a BTO substrate by the dropcasting method (b) In plane scattering of iron oxide NP multilayers. Projection in $Q_z = 0.65$ nm^{-1} of GISAXS intensity is shown on a logarithmic scale. Reflections of the peaks are indexed according to the *P6mm* group with $a = 22.08$ nm.

is evaluated from the correlation lengths. The correlation lengths were determined from the first order reflections (10) of the lateral scattering contribution. After taking the instrument resolution into account, a Lorentzian profile is used to fit to the first order peaks. A structural coherence length of 186 ± 7 nm is derived.

In order to investigate the ME coupling effect, the same measuring geometry used for the monolayer sample is applied to the multilayers samples. Except the preparation method for the multilayer NP self-assembly, the other preparation and treatment parameters were kept the same.

The magnetic response as function of temperature was measured in the cooling direction and subsequent warming direction for the system Au / BTO / Ti / NP multilayers / Au. The results are shown in Figure 4.34. Both curves show the typical NP superparamagnetic behavior except two small jumps at 280 K and 185 K. The magnitude of the magnetization jump is much smaller than that in the monolayer system. This is likely due to the reduced strain resulting from the BTO phase
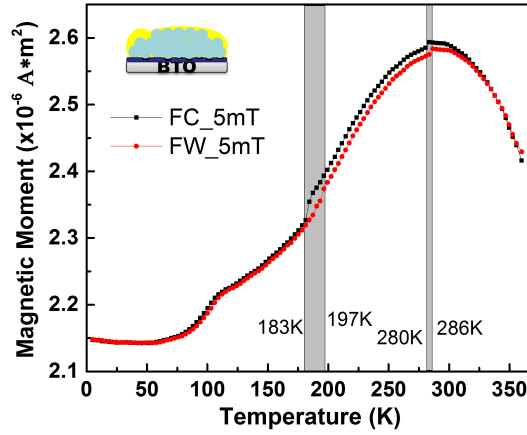
Figure 4.34: In-plane magnetic moment vs. temperature during FC and subsequent FW in 5mT for the system BTO / Ti / NP multilayers / Au. The vertical grey bars indicate the temperature regions where bulk BTO has first order phase transitions from T to O to R phase, The schematic diagram of the sample is shown in the left-upper corner of the figure.

transition acting on less NP layers and thus leaving most of the layers unaffected. One should note that the mean value of the magnetization jump $|\Delta M|$ is still two times larger than that of the monolayer. In addition, the magnetic bump at around 110 K, which is ascribed to the Verwey transition of magnetite, is also due to the oxygen plasma treatment on the NPs as shown before in NP monolayer systems. The MEC effect is not as large as for the monolayer sample. Therefore the further investigations were not performed on this system.

In summary, the NPs self-assembled in multilayers are arranged in the same hexagonal pattern as the monolayer. The MEC effect is smaller, which might due to the strain being too small to fully affect every NP layer of the sample.

In order to show more wide applications and more investigations on nanoscale materials, BTO films were prepared to replace substrates in the next chapter.

Chapter 5

Results II: Iron oxide NPs on BTO films

In this chapter, magnetoelectric composites consisting iron oxide NPs and BTO films are discussed. The characterization of the prepared BTO films and the resulting MEC effects between NPs and BTO films are reported.

5.1 Sample preparation

The preparation and characterization of samples from Nb-doped STO / BTO to the final magnetoelectric sample Nb-doped STO / BTO / NP monolayers / BTO / Au are described in the following.

5.1.1 BTO thin films

The BTO films were grown using Pulsed laser deposition (PLD) in collaboration with Dr. Jürgen Schubert from PGI-9 (Forschungszentrum Jülich). The thickness of the BTO film was chosen to be 500 nm because the thickness should be large enough to avoid the short circuiting during electric field application.

Three substrates, namely Yttrium stabilized zirconium (YSZ), YSZ film buffered Silicon (Si) and Niobium doped Strontium Titanate (Nb-doped STO) substrates, were used to prepare BTO films with good crystal quality and surface homogeneity. The best film quality was achieved using Nb-doped STO substrates. The parameters are shown in the Appendix C.

Next I discuss the properties of the BTO films.

Topography

The topography of the as-prepared BTO films was observed using SEM. Besides several defects shown in Figure 5.1(a), more details are seen in the magnified part as shown in (b). The bright dots are the BTO islands, which are due to the aggregation of BTO particles during preparation. In order to quantitatively evaluate the quality
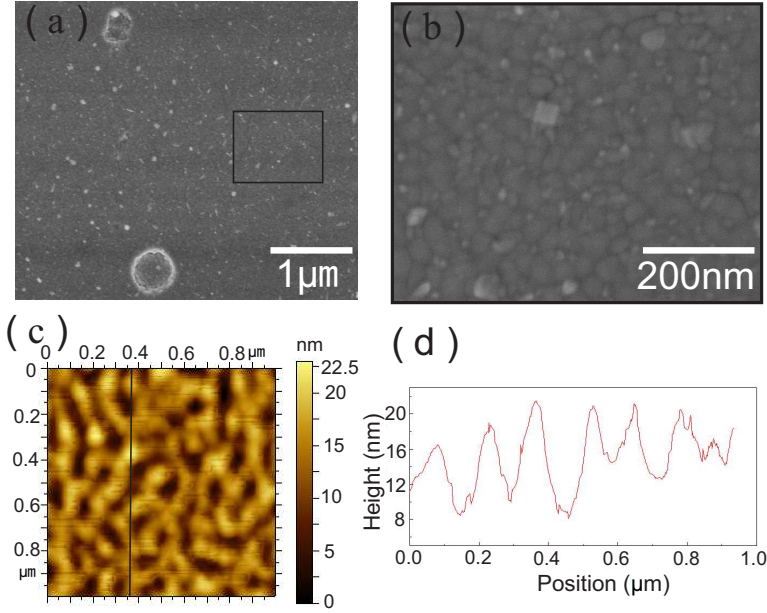
Figure 5.1: The morphology and topography of a BTO film grown on a Nb-doped STO substrate. (a) SEM image of the morphology of the film. (b) Magnified part of the black rectangle area in (a). (c) Topography of the BTO film measured by AFM, and (d) is the line cut. The position of the line cut is shown by the black line in (c).

of the prepared BTO films, the roughness of the BTO film is probed by AFM as shown in Figure 5.1(c). A line cut is plotted in Figure 5.1(d). The roughness of the BTO film is approximately 12 nm. The relatively bad quality of the surface is due the island growth mode of the BTO. The surface roughness can be improved by reducing the thickness of the film, however, at the cost of risking a larger possibility of current leakage.

Structural properties

The structural properties of the as-prepared BTO films on Nb-doped STO substrates were probed by XRD. The result is presented in Figure 5.2. The peaks were indexed by Nb-doped STO and BTO lattice parameters. The result indicates that the BTO film shows a relatively good crystalline quality. Split peaks at high angles are observable, i.e. the (004) and (400) reflections around 98°. They correspond to the lattice constants of 4.064 and 4.026 Å, respectively. The split peaks indicate that there is a tetragonal phase in the as-prepared films [110].
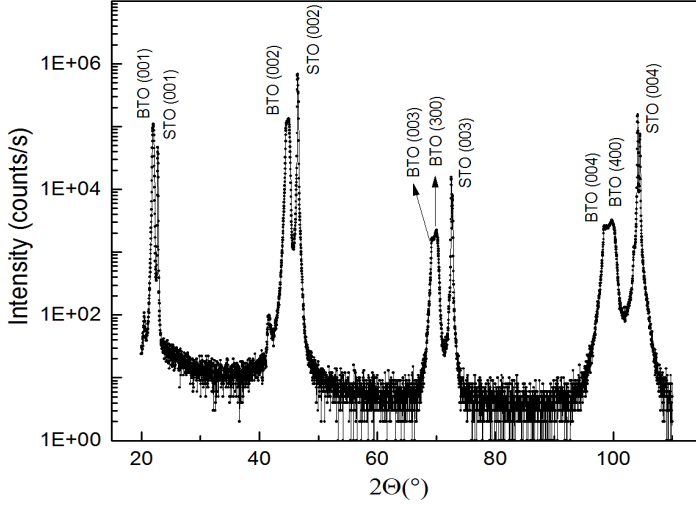
Figure 5.2: XRD pattern of the as-prepared BTO film. Bragg peaks are indexed according to Nb-doped STO and BTO lattice parameters.

Dielectric properties

In order to further investigate the phase transitions of the as-prepared BTO films, temperature dependent permittivity measurements were conducted using the CCMS. A 2×2 mm^2 Au thin film with a thickness of 25 nm was deposited onto the BTO film samples as top electrode to cover the BTO film. Since Nb-doped STO is a good electrical conductor (conductivity is 10^4 $\Omega^{-1} \cdot$ m^{-1}), the substrate itself was used as the bottom electrode. Two copper wires were attached to the top and bottom electrodes, respectively. An AC electric voltage of 2 V and 1 Hz was applied to the sample. The sample was measured in cooling direction and subsequent warming direction (Figure 5.3).

We found that the permittivity decreases as the temperature drops which is ascribed to the formation of larger ferroelectric domains at lower temperature. The increasing domain size leads to a reduction of the reversible polarization and thus a decreased net permittivity [111]. Moreover, the permittivity curve in cooling direction shows a small bump at 248 K, whereas no significant feature is observed in the warming branch. The phase transition temperatures of the BTO films usually strongly differ depending on different preparation conditions, i.e. deposition methods, chamber pressure, deposition temperature etc. [70, 112]. However, since the as-prepared BTO films show the T phase already at room temperature, the bulge is most likely related to the phase transition from T to O. On the other hand, the O to R phase transition might be too weak to be observed from the permittivity curve.
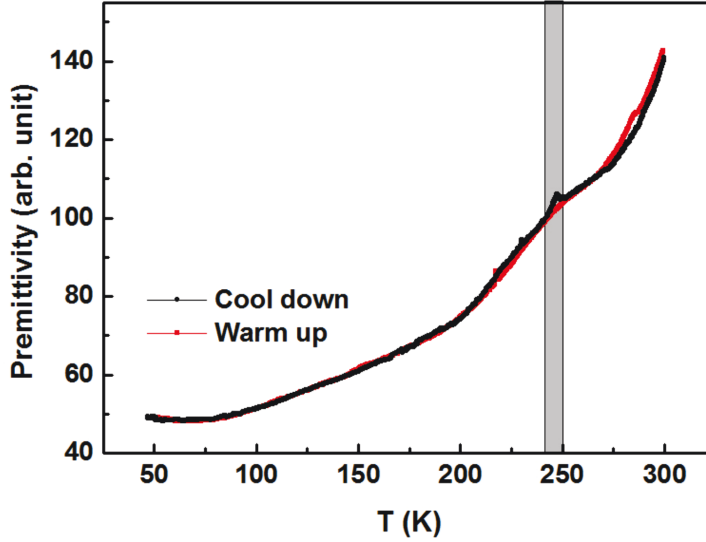
Figure 5.3: The permittivity versus temperature of Au/BTO film/Nb-doped STO. An AC electrical voltage of 2 V and 1 Hz was applied to the sample. The measurement was probed in cooling direction and subsequent warming direction.

Magnetization

In order to estimate the magnetic contribution of the BTO film to the ME system, the magnetization of the as-prepared BTO film on STO was measured using the MPMS device. The temperature dependent magnetization was measured as ZFC and FC curves and the results are presented in Figure 5.4(a). One observes only a superposition of diamagnetism, i.e. the T-independent negative magnetic value for $T \to \infty$, plus a small paramagnetic contribution which is likely due to magnetic atomic impurities in the BTO film and/or Nb-doped STO substrate. E.g. the Nb-doping could give rise to a paramagnetic contribution.

The magnetic field dependent magnetization at room temperature is shown in Figure 5.4(b). A regular diamagnetic behavior of the BTO film and of the substrate is found as a linear curve of the magnetic moment vs. magnetic field. Moreover, the magnetic moment of the BTO film is in the range of 10^{-9} A $\cdot$ m^2, which is two orders of magnitude smaller than the magnetic moment of iron oxide NP layers (See Figure 4.7(a)). Therefore, it is concluded that the as-prepared BTO film shows basically only diamagnetic properties and is negligible to the overall magnetic signal of the ME composites above 25 K.
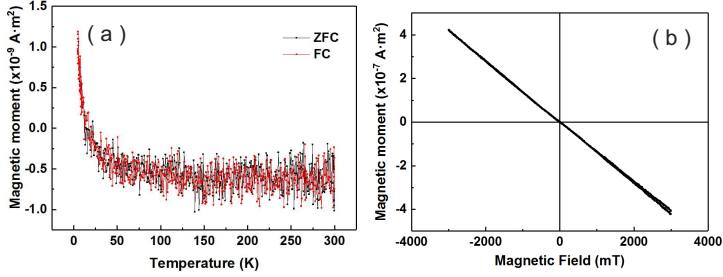
Figure 5.4: Magnetic moment of the sample BTO film / Nb-doped STO substrate. (a) ZFC and FC curves at 5 mT. (b) Magnetization vs. magnetic field at 300 K.
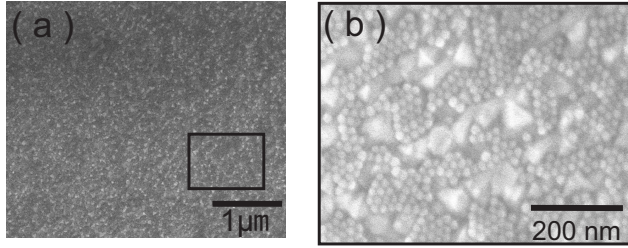
Figure 5.5: (a) SEM images of iron oxide NPs distributed on top of the BTO thin film. (b) The zoom-in was taken from the region marked by the rectangular box in (a)

5.1.2   Nb-doped STO / BTO / NP monolayers

The iron oxide NPs dispersion was diluted by toluene in the volume ratio of 1:10. After dilution, 2.5 μl of solution was taken by a transferpettor and dropped onto the BTO films and spin-coated with 50 rps for 30 s. The sample was dried in air for 10 min. In order to remove the organic oleic acid shell around the NPs, the samples were treated in an oxygen plasma asher with an oxygen pressure of 0.3 mbar, a gas flow of 200 ml/min and a power of 3000 W for 5 min.

The morphology of the sample probed by SEM is shown in Figure 5.5(a). The dots in the images are aggregated BTO islands and the brighter grey scale is due to secondary electrons emitted by the iron oxide NPs. The zoom-in of the black square marked area in Figure 5.5(a) is displayed in (b). From the figure it is seen that the NPs cover almost the entire surface of the BTO thin film. However, long range ordering of NPs is not formed due to a "perturbation" effect by the randomly distributed BTO islands. The short range order is also evidenced by the amorphous rings in GISAXS measurements as shown in Figure 5.6. The incident angle of the beam is $\alpha_i = 0.4^o$. The direct beam center is located at the crossing of the two black lines which is blocked by a beam stop at $Q_y = Q_z = 0$ nm^{-1}. The reflection of the direct beam is shown as a high intensity spot above the direct beam center at $Q_z =$
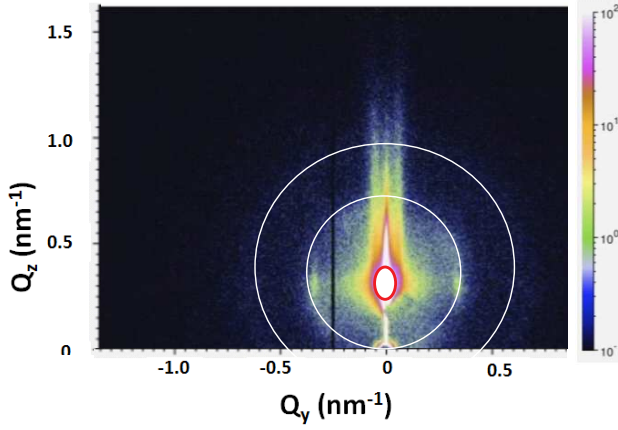
Figure 5.6: GISAXS pattern of self-assembled iron oxide NPs on the BTO film. The black line is a dead region of the detector. The red circle marks the reflected beam and the two white circles are used to visualize the two powder rings.

0.039 nm^{-1}. In the GISAXS pattern, only two powder rings are visible around the direct beam, which indicate that the NPs are randomly arranged and no long-range order established. The results also match the SEM observation.

5.1.3   Nb-doped STO / BTO / NP monolayers / BTO / Au

In order to search for a ME coupling effect, a sandwich sample geometry consisting of Nb-doped STO / BTO / NP / BTO was fabricated. Hence another 500 nm BTO film was prepared to cover the NP layers. Moreover a 25 nm Au thin film was deposited on top as a top electrode for the investigation of the electric field manipulated magnetoelectric coupling effect.

5.2   Results

The measurements in this section were carried out on the Au / BTO / NP monolayer / BTO / Nb-doped STO sample. Temperature dependent magnetization curves in the sequence of ZFC, FC and FW are shown in Figure 5.7. The FC curve is superimposed to the FW curve. The ZFC and FC curves show a typical superparamagnetic behavior of iron oxide NPs, which is similar to the magnetization of the NP monolayer / Si sample (See Ref. [26]). This indicates that BTO has an negligible contribution to the magnetization of the system. The blocking temperature (T_B) is ca. 300 K. No MEC effect can be observed between BTO and NPs according to the magnetometry measurement.

Before the discussion of the results of the effect of an electric field onto the magnetization of the system, the determination of the value of electric field has to
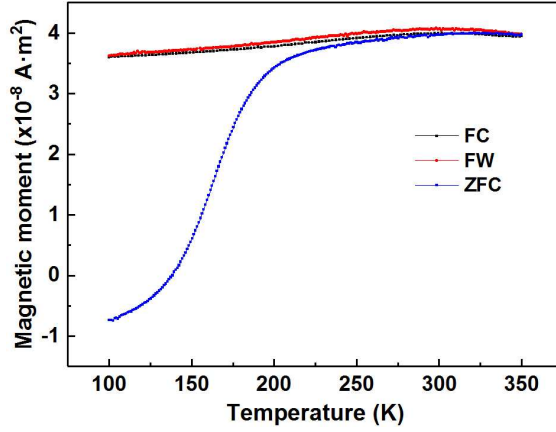
Figure 5.7: Magnetic moment versus temperature curves of Nb-doped STO / BTO / NP monolayer / BTO / Au sample in the sequence of ZFC, FC and FW. The measurements were recorded in a magnetic field of 5 mT.

be clarified. In comparison of the reference value of the resistivity between the Nb-doped STO substrates (i.e. $\sigma = 10^4 \; \Omega^{-1} \cdot$ m^{-1}, see Figure 2 in Appendix D. and Ref. [113]) and BTO single crystals (i.e. $\sigma = 10^5$ Ohm·m, [114]), the voltage loss across the Nb doped STO substrates is negligible even after taking the thickness of the Nb-doped STO substrate (0.5 mm) and BTO thin film (1 μm) into account. Hence the electric field in the following is calculated by dividing the voltage by the total thickness of BTO films (1 μm).

The effect of the electric field onto the temperature dependent magnetization was investigated with a modified SQUID magnetometer setup (see section 3.6). The sample was measured during cooling in a magnetic field of 5 mT and voltage of 0 kV/cm or 100 kV/cm (Figure 5.8). The overall magnitude of the FC curve with the voltage of 100 kV/cm is smaller than without voltage and data with a larger noise level is obtained. This is probably due to the influence of the applied voltage to the sensor coil in the SQUID magnetometer.

The effect of the electric field on the magnetization as a function of magnetic field at 5 K is shown in Figure 5.8(b). Both hysteresis loops show NPs in the blocked superparamagnetic state. However, it clearly shows that the remanent magnetization (M_r) of the hysteresis loop with applied electric field is larger than the one without field, while the saturation magnetization (M_s) remains the same. Hence, M_r / M_s, namely the "squareness", increased after field application. The squareness is a criterion for evaluating the magnetic anisotropy. Since the other values stay the same except the electric field application in both measurements, the result suggests that the electric field has the capability to manipulate the anisotropy of the sample.

The electric field manipulation of the magnetization was performed with the same setup. The samples were measured as a function of a linearly changing electric field.
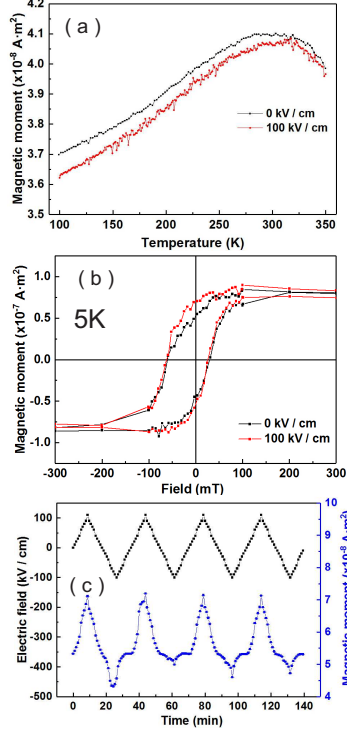
Figure 5.8: (a) FC curves of the sample at an electric field of 0 kV/cm and 100 kV/cm. (b) Hysteresis loops measured at 5 K with electric field. (c) Magnetization as a function of electric field. The black curve with the left Y-axis indicates the periodically applied voltage at the sample, while the blue curve with the right Y-axis represents the magnetic moment of the sample.

The amplitude of the electric field was varied from -100 kV/cm to +100 kV/cm with a constant magnetic field of 5 mT being applied during the measurement. The applied electric field and the time-dependent magnetization are displayed in Figure 5.8(c). The magnetization of the sample changes periodically and follows directly the electric field. This demonstrates that the electric field is able to modify the magnetic state of the system.

Apart from DC electric field measurements, the effect of an AC electric field on the magnetic properties of the sample was also probed. The temperature dependent MEACS coefficient α_{ME} was measured with the AC electric field with a frequency $f = 1$ Hz or 9 Hz and $U_0 = 4.5$ kV/cm or 9 kV/cm, respectively.

α_{ME} as a function of temperature is plotted in Figure 5.9. The sample was first investigated in cooling direction during applying an AC electric field of 4.5 kV/cm with 1 Hz and a constant magnetic field of 5 mT (Figure 5.9(a)). The α_{ME} is negative and increases smoothly as the temperature increases. Moreover, a jump at
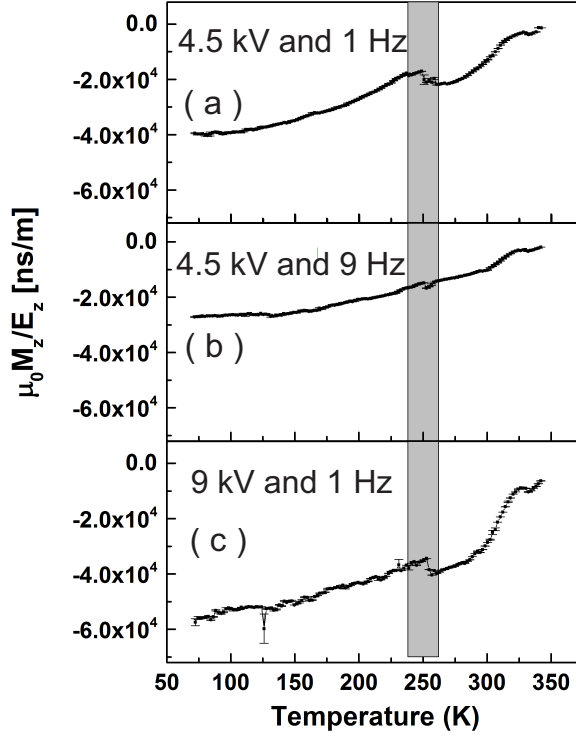
Figure 5.9: ME coefficient α_{ME} vs. temperature measured under a constant magnetic field of 5 mT and an AC electric field with different frequencies and amplitudes. The three curves are plotted with the axis with the same scale for better comparison.

around 250 K and a small jump at 340 K are observed.

The jump at around 250 K is first considered. One notes in Figure 5.3 that the permittivity as function of temperature of the sample BTO / Nb-doped STO also shows a kink at 248 K, which is ascribed to the phase transition of the BTO thin film. Therefore, the observed change in α_{ME} might be related to the BTO phase transition. When further increasing the frequency to 9 Hz, while keeping the amplitude constant, both the amplitude of α_{ME} and the signal jump at 250 K become smaller (Figure 5.9(b)).

If the frequency is kept at 1 Hz and the electric field strength increased to 9 kV/cm, both the amplitude of α_{ME} and the jump are enhanced (Figure 5.9(c)). Similar observations were made at 340 K where α_{ME} drops. Since the lock-in technique prevents interferential signals from other background frequencies, the jumps in each curve should only result from the applied electric field at the specific frequency. This means that the observed AC electric field manipulation of the magnetization is not an artifact.

5.3   Discussion and outlook

The ME coupling induced by the electric field can be interpreted as the indirect MEC effect. The induced strain via the piezoelectric property of BTO film is enhanced by the increased electric field amplitude (see Figure 2.15(a)). The enhanced strain leads to the jumps via magnetostriction in the NPs. An electric field with large frequencies decreases the ME coefficient. This is because high frequencies give rise to a non-zero imaginary part of α_{ME} in expense of the real part.

Interface charge driven MEC effects could also be the origin of the MEC effects especially for the electrically manipulated ME thin film systems [115, 116, 107]. I.e. The additional magnetic moment might be modified via screening charges induced by the polarization of the BTO film. The induced electric polarization in the BTO film would generate surface charges at the surface of the BTO film and the charges are screened by an equal number of charges of opposite sign from the NPs. Hence the screening charges would be spin-polarized due to the FM exchange interaction and result in an additional magnetic moment. An opposite electric field will give an additional magnetic moment in a opposite sign with respect to the total moment of the system. Such a scenario might explain the electric field manipulation of the magnetic moment as shown in Figure 5.8(c).
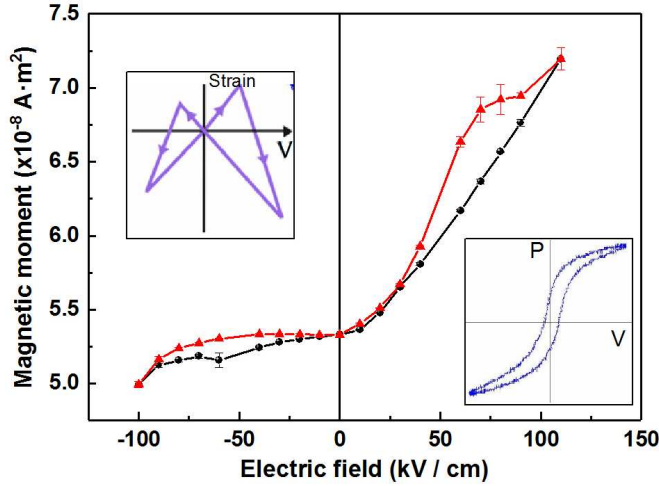
Figure 5.10: Magnetic moment vs. applied electric field at 300 K and 5 mT, the black curve is measured with increasing DC field from -100 kV/cm to +100 kV/cm, while the red square points were measured in reversed sequence. The inset shows the in-plane piezostrain vs. electric field and polarization vs. electric field of the BTO film as adapted from Ref. [107].

ME thin film systems are widely reported to be manipulated by several coexisting mechanisms [117, 118, 119, 120]. For example, a ME system consisting of BTO

and Ni films was reported by Li [107]. In this system, the magnetization vs. electric field curve shows an asymmetric shape which can be decomposed as the ferroelectric hysteresis loop and piezoelectric butterfly shape loop. It is similar as we observed in Figure 5.10. Hence, strain and interface charge co-mediated MEC mechanism is proposed to interpret our results.

In summary, an artificial ME heterostructure of Nb-doped-STO / BTO / NP / BTO / Au was prepared and an MEC effect was observed as shown by the measurements of both magnetization and MEACS. Strain and interface charge co-mediation mechanism is responsible for the MEC effect. However, the short circuit problem cannot be overcome in our film system which results in a small MEC effect.

Chapter 6

Results III: NPs self-assembled on patterned substrates

In this chapter, template-assisted self-assembly was used to produce ordered arrays of iron oxide NPs over a relatively large area. Two templates, i.e. sawtooth-patterned sapphire wafers and trench-patterned silicon substrates, were used to prepare NP arrangements as (pseudo-) 1D NP chains. The sample preparation and characterization are described. Additionally, the magnetic anisotropy and memory effect induced by the shape anisotropy of the 1D NP arrangement are discussed.

6.1   NPs / patterned sapphire substrates

Sawtooth patterned sapphire substrates were fabricated with the help of our collaborator Dr. Yinguo Xiao from JCNS-2. (1010) oriented regular sapphire wafers ($\alpha - Al_2O_3$) were commercially obtained (SurfaceNet GmbH). The thickness of the substrate is 430 μm with one side polished. The sapphire substrates were cut into the pieces with the size of 5 x 5 mm^2. The reconstruction of the sapphire wafer surface can be achieved by a special annealing treatment. The sawtooth pattern was generated after annealing the substrates under 1673 K in air for 24 h [121].

The morphology of the as-prepared samples was checked by SEM as shown in Figure 6.1. The sawtooth has a pitch of around 120 nm and a depth of around 25 nm. The period of the pattern is around 200 nm.

The spin coating method is found to be the best approach to place NPs in the sawtooth patterns while avoiding aggregations. Results of self-assembled NPs on such substrates using spin coating speed of 50 rps for 30 s are shown in the following.

The morphology of the sample was checked by SEM (Figure 6.2). The sawtooth pattern is in the shape of a nearly equilateral triangle with a period of around 80 nm [122, 123]. It is observed that a one dimensional arrangement NP chains is located inside the sawtooth valleys in Figure 6.2(a). However, the regular sawtooth pattern is not homogenously distributed over the whole substrate. The sawtooth pattern in some area are bend and misaligned and hence causing the misalignment
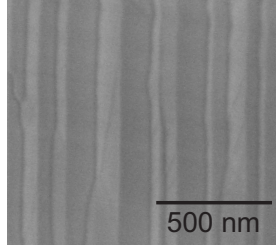
Figure 6.1: SEM image of a sawtooth patterned sapphire substrate.
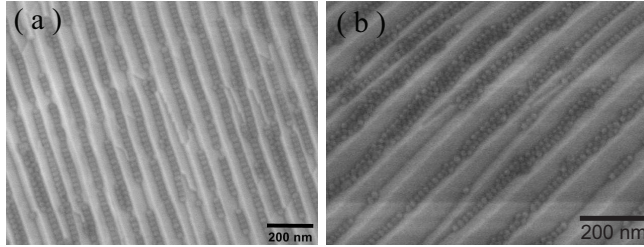
Figure 6.2: (a) SEM images of well aligned self assembled NPs inside the groves of sawtooth pattered sapphire substrates. (b) In some areas, NPs are aggregated and misaligned due to the inhomogeneity of the sawtooth pattern.

of NP chains and the aggregation of NPs, which is shown in Figure 6.2(b).

The magnetic moment as function of magnetic field of the sample was measured. The magnetic field was applied in plane, parallel and subsequently perpendicular to the sawtooth direction at 300 K and 10 K, respectively (Figure 6.3 (a) and (b)). The remanent magnetization (M_r) and coercivity (H_c) of the NPs are larger when the magnetic field is applied parallel to the sawtooth direction than when the magnetic field is perpendicular to it (ΔM_r =52% and 12%, $\Delta H_c = 1\%$ and 5% for 300 K and 10 K respectively). It can be explained by the shape anisotropy of NP chains inducing a magnetic easy axis. When the magnetic field is applied parallel to the sawtooth, the superspins of NPs align along the field direction easier due to the shape anisotropy of the chain shape.

However, the shape anisotropy induced easy axis is not so obvious in the sawtooth patterned sapphire substrate due to the inhomogeneity of the sawtooth pattern on the substrates.

6.2 NPs / patterned Si substrates

In order to improve the regularity of the patterns on substrates, linear trenches pattern of a size of 10 x 10 x 0.5 mm^3 Si substrates were co-designed with the Eulitha company. The displacement talbot lithography method was used in the
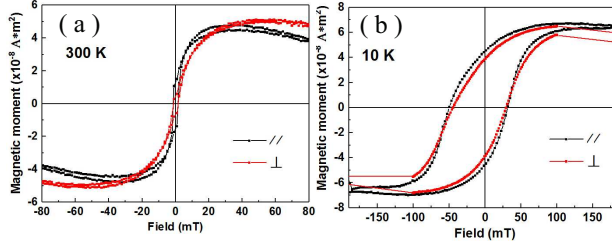
Figure 6.3: Hysteresis loops of self-assembled NPs on sapphire substrates at different directions at different temperatures, (a) 300 K and (b) 10 K. The red hysteresis loops in both figures were measured at the magnetic field parallel to the gratings, the black curves were measured perpendicular to the gratings.

substrate preparation process to generate the periodical rectangular-shaped concave trenches [124]. The details of the parameters used in the preparation are attached in the Appendix E. The trenches have a width of 150 nm, a depth of 100 nm and a period of 150 nm. The substrate was cut into small pieces with the size of 5 x 5 x 0.5 mm^3 for use in the magnetic measurement systems. The morphology of the trench-patterned Si substrates was characterized by SEM as shown in Figure 6.4.
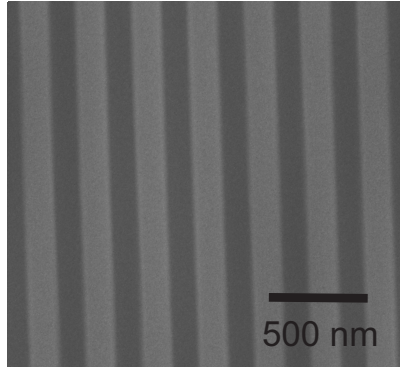
Figure 6.4: SEM image of the trench-patterned Si substrate.

Iron oxide NPs from the same batch as used before were employed for this system. The NPs dispersions were diluted with the volume ratio of 1:10 with toluene. Afterwards, the dispersion was placed into a ultra-sonic bath for 5 min to homogenously disperse the NPs. 3 μL of solution were taken by a pipette to drop on a 5 × 5 × 0.5 mm^3 Si substrate which was fixed onto a spincoating machine via a vacuum pipe. The spincoating machine was hereby kept running at the speed of 50 rps for 60 s after the NPs solution was dropped onto the substrate. In order to move the NPs into the trenches, the as-prepared samples were placed in a container with a pair of permanent magnets on both sides. The magnetic field was applied

perpendicular to the trenches. In order to slow down the evaporation process and provide sufficient time for the movement of NPs, we added 1 μL toluene onto the surface of the substrate every 3 min. Eventually the samples were prepared after 10 cycles of adding toluene and evaporation.
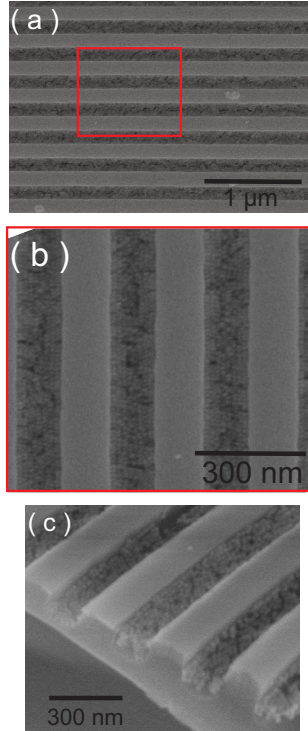
Figure 6.5: SEM images of self assembled NPs on the trench-patterned Si substrate. (a) The morphology of the sample in a wide view. (b) The magnified SEM picture indicated as the red rectangle in (a). (c) Side view of the sample.

The SEM images of the self-assembled NPs on the pattered Si substrates are displayed in Figure 6.5. NPs are well located at each trenches with very few particles on the mesa tops. As seen from Figure 6.5(a), the NPs show a continuous close-packing in the trenches. Around 7 to 8 column of particles are observed in each trench. The cross-section image of the sample shown in Figure 6.5(c) indicates that the NPs columns beside the edges are stacked in different layers.

In order to detect the structural coherence length of the NPs inside the trenches, GISAXS was employed. The measurements were performed with the incident beam parallel and perpendicular to the trenches, respectively (Figure 6.6 (a) and (b)). For the parallel case, the angle of the incident beam with respect to the long axis of the trench was $\alpha_a = 0.3^o$. The titled azimuthal angle prevents the strong scattering background from the trenches overwhelming the intensity from the NPs. A bent tail
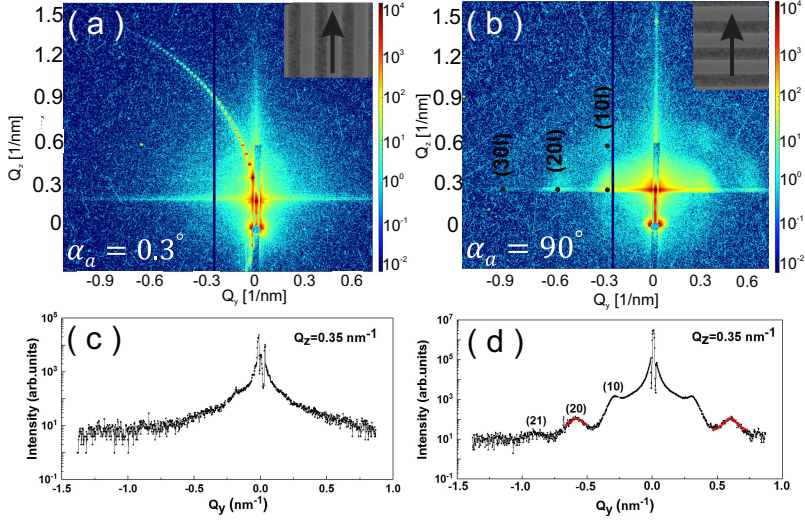
Figure 6.6: (a) GISAXS pattern of the sample with the beam almost parallel to the trench long axis. The azimuthal angle (α_a) of the sample was titled by 0.3^o to reduce the scattering intensity from the trenches (b) GISAXS pattern with the beam perpendicular to the trenches long axis ($\alpha_a = 90^o$). The angle of the incident beam (α_i) is in both cases 0.2^o. The perpendicular white line is a dead region of the detector. The direction of the X-ray beam with respect to the trenches is illustrated on the top-right corner of each figure. (c) A line cut from (a) along Q_y at $Q_z = 0.35$ nm^{-1} .(d) Line cut from (b) along Q_y at $Q_z = 0.35$ nm^{-1} along with a Lorentzian fit (red line) to the two (21) Bragg peaks. The Bragg peaks were indexed according to a hexagonal lattice with $a = 21$ nm.

can be observed from the GISAXS pattern, which results from the trenches. Apart from that, only blurry rings around the beam center are observed. It is due to the form factor of the NPs. The result indicates that the NPs have non-observable coherence in the direction perpendicular to the long axis of the trenches.

The measurement was performed again after azimuthal rotation of the sample by 90.3^o. Hereby the incident beam was perpendicular to the long axis of the trenches. Intensity dots superimposed to the rings are observed. The 2d-Bragg dots along Q_y are due to the laterally correlated structures, while the dots along Q_z provide the information on out-of-plane correlations. A line cut along Q_y at $Q_z = 0.35$ nm^{-1} was taken on both GISAXS patterns. There are no Bragg peaks when the beam is parallel to the trenches as shown in Figure 6.6(c). Bragg peaks at $Q_y = 0.30$ nm^{-1}, 0.60 nm^{-1} and 0.90 nm^{-1} can be observed when the beam is perpendicular to the trenches as shown in Figure 6.6(d).

The peaks are indexed assuming a hexagonal close-packed lattice with a lattice constant $a = 21.03 \pm 0.53$ nm. After taking the instrument resolution into account, a Lorentzian profile is used to fit to the second order peaks at $Q_y = 0.60$ nm^{-1} and -0.60 nm^{-1} which yields a structural coherence length of 60.5 ± 0.9 nm.
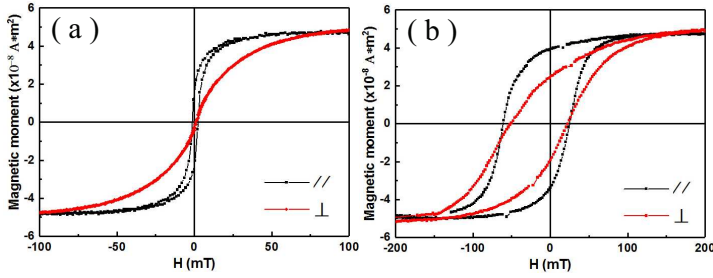
Figure 6.7: Hysteresis loops for the NPs on pattered silicon substrate (a) at 300 K and (b) at 10 K. The red hysteresis loops in both figures were measured with the field applied parallel to the trenches, the black ones were measured perpendicular to the trenches.

Hysteresis loops were measured with an external magnetic field applied parallel to the direction of the trenches at 300 K and subsequently at 10 K. Afterwards, the sample was rotated to have the field perpendicular to the trenches and the same sequence was performed. The results compared for different field directions at 300 K and 10 K are shown in Figure 6.7(a) and (b), respectively.

Magnetization in perpendicular case is slower to reach saturation than in parallel case and this difference can be quantified by the magnetic squareness, which is expressed as the ratio of the remanent magnetization (M_r) to the saturation magnetization (M_s), i.e. $\zeta = M_r / M_s$. The magnetic squareness is a widely used criteria for the evaluation of magnetic anisotropy and of the magnetization reversal mode [97]. Here we assume that the reversal mode inside the NPs will stay unchanged, hence the squareness value will give the information about a change of anisotropy.

The remanent magnetizations at both temperatures are significantly higher in the parallel versus perpendicular direction, while the saturation magnetizations are identical. Therefore, the squareness value is larger by 589% and 61% in the parallel case compared to the perpendicular case at 300 K and 10 K, respectively. The increase of squareness can be interpreted by the NP chain induced shape anisotropy. The physical shape of the assembly determines the magnetic shape anisotropy of the NP chains in the trenches. For example, the elongated strand can be approximated as an ellipsoidal particle that has a shape-induced uniaxial anisotropy with the easy axis along its length [125, 126, 127]. The demagnetization energy of the ellipsoidal body is expressed in Equation 2.18. The energy will show a minimum when the superspins align lengthwise along the long axis of the body. Hence, NPs within each chain will tend to algin easier with the applied field along the trench.

Y. Sahoo reported that 10 nm Fe_3O_4 NPs in a one dimensional structure tend to orient with their superspins in a head-to-tail configuration with their easy axes aligned with the applied field [128]. Wiedwald et.al observed that a hexagonal network of cobalt NPs has the similar superferromagnetic configuration [129]. Superferromagnetic dipolar ordering in hexagonal patterned spherical NPs are also predicted and evidenced by electron holography by Varón M. et.al [130].

Shape anisotropy gives rise to an energy barrier in the spin reversal process. As shown in Figure 6.7(a) and (b), larger coercive field are needed to reverse the spins in the measurement when the magnetic field is parallel to the trenches. The coercive fields increase by 105% and 18% at 300 K and 10 K from the parallel to the perpendicular measurement, respectively.

An exchange bias (EB) effect was observed at 5 K, in both hysteresis loops as shown in Figure 6.7(b). It is due to the antiferromagnetic wuestite inside the NPs below its Néel temperature at 198 K [94].

In order to visualize the magnetic structure, off-axis electron holography in the transmission electron microscope was employed to directly measure the projected in-plane magnetic induction, $B_\perp$, of the self-assembled NPs in the trench at its remanent state. The data were acquired at 300 kV in Lorentz mode ST TEM (Titan 80-300) with an electron biprism operated at 200 V in Ernst Rusk-Centre under the help of Fengshan Zheng and Penghan Lu.

Figure 6.8(a) shows the morphology of the NPs in a randomly-chosen trench. Figure 6.8(b) shows a uniform holographic phase map, which was obtained at remanent state after an applied magnetic field of 0.98 T perpendicular to the trench direction as indicated by the white arrow. The projected in-plane magnetic induction, Figure 6.8(c) was calculated from the gradient of the phase image. The uniform contrast over the whole trench implies that there is no ordered magnetic texture along or between the NP strands.

Similarly with an applied magnetic field of 0.98 T parallel to the trench direction, the magnetic phase at the remanent state of NPs was measured and its projected in-plane magnetic induction was calculated as shown in Figure 6.8(d, e), respectively. The periodic contrast both in the phase image and magnetic induction map indicates that there is an ordered magnetic texture in the NPs. It is worth noting that the
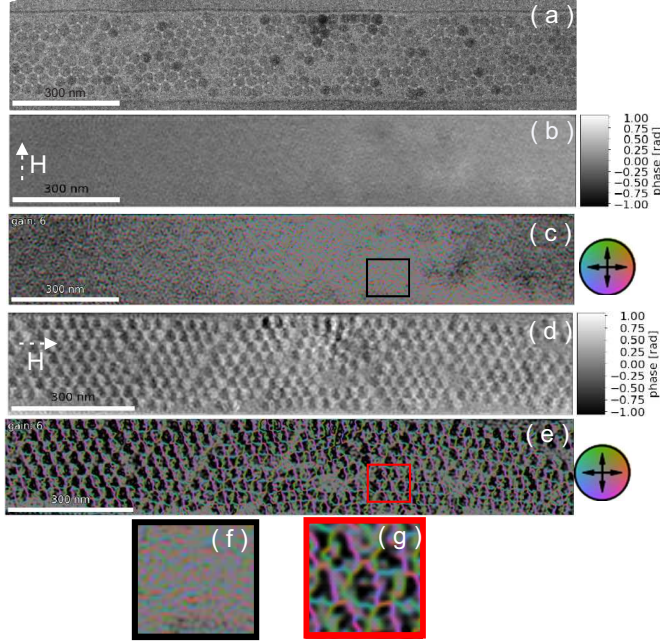
Figure 6.8: (a) Bright-field TEM image of the NPs in a randomly-chosen trench. (b, d) Magnetic phase images of NPs at remanent state after an applied magnetic field H of 0.98 T perpendicular and parallel to the trench, respectively. The scale bar of the magnetic phase is indicated on the right hand side. (c, e) The projected in-plane magnetic induction maps of the NPs corresponding to (b, d), respectively. Colors and arrows are used to indicate both the strength and the direction of the projected in-plane magnetic induction as shown by the color wheel on the right hand side.(f) and (g) are the enlarged images for the marked region in (c) and (e), respectively.

direction of the magnetic induction is inclined to trench, which may be due to the charging effects from the semiconducting substrate [131].

The ZFC and FC curves measured along different directions and at different external magnetic fields are shown in Figure 6.9.

The sample was first cooled down in zero magnetic field from room temperature to 5 K, subsequently a constant field of 5 mT was applied and the ZFC curve recorded upon warming up to 350 K. Finally, the FC measurement was done at the same field upon cooling. The measurements were performed with the field parallel and perpendicular to the trenches at 5 mT and 20 mT. It is expected that under the same field, the magnetization is larger if the magnetic field is applied parallel to the trenches than if the field is applied perpendicular to the trenches. This is because the spin alignment is more energetically favorable along trenches.

It is hard to determine the blocking temperature (T_B) from the ZFC due to the broad peaks. The broad peaks might result from the broad size distribution of the
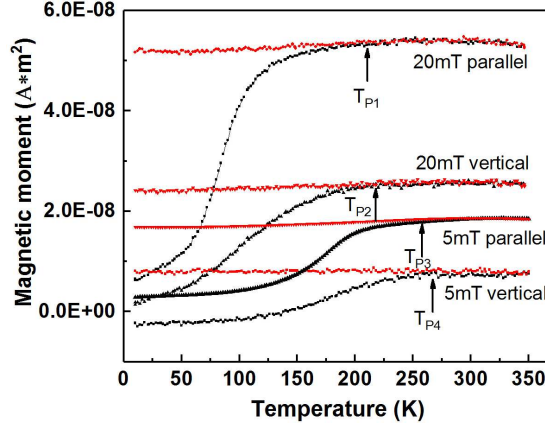
Figure 6.9: Temperature dependence of the magnetic moment of NPs self-assembled in trench-patterned Si substrates during ZFC (black) and FC (red) at a magnetic field of 20 mT and 5 mT, respectively. The magnetic field was applied along or perpendicular to the trenches. The arrows indicate the peak temperature T_p, which was defined as the first zero value of the derivative of the ZFC curve.

clusters [132, 133]. Hereby, a peak temperature T_P with a similar physical meaning as the T_B is defined. T_P is the temperature where the first zero value appears in the derivative curve of the ZFC from low temperatures upward.

We notice that a larger magnetic field will decrease the peak temperature T_P in both parallel and perpendicular measurements. This is in accordance to usual SPM-like systems, i.e. larger fields reduce the effective relaxation time of the super-spins [40, 24, 38]. While the magnetic field strength is the same, the T_P is slightly smaller when field direction is parallel to the trenches compare to the situation when the direction is perpendicular to the trenches. This might be due to the fact that in the hard axis direction the effective relaxation time is larger due to the unfavored superspin alignment.

The negative value of the ZFC curve measured perpendicularly at 5 mT is due to the diamagnetic signal of the Si substrate.

To elucidate the magnetic collective state furthermore, memory effect measurements were performed. The difference in the memory effect between the two different magnetic field application directions is shown in Figure 6.10. Firstly, a regular ZFC curve was measured as a reference measurement at a magnetic field of 5 mT. After that, the sample was cooled in zero field with a temporary pause at a temperature T_S ($< T_P$). After aging the sample for the time t_S, the cooling was resumed down to 5 K and the magnetization (M_{aging}^{ZFC}) was measured during heating in a field of 5 mT analogous to the reference curve. Such ZFC curves measured in parallel geometry with T_S= 140 K, 160 K and 190 K and t_S= 7200 s are shown in the upper part of Figure 6.10(a), while ΔM is shown in the lower part corresponding to the right

Y-axis. The aged ZFC curve coincides with the regular ZFC curve at and below T_S and also merges with it at temperatures above T_S. In the difference curve ΔM, a small peak is found near to T_S (Figure 6.9(a)). This is an evidence for superspin glass behavior [40, 24, 38].

The situation is different when the memory effect measured is in perpendicular geometry. Here the ΔM is larger than in the parallel case by a factor of 10. This indicates that in perpendicular geometry the memory effect is clearly more pronounced and in other words, the superspin glass state is more pounced.

Our interpretation is that in the parallel case, i.e. where the shape favors more a superferromagnetic state, the superspin glass behavior is largely suppressed. However, in the perpendicular case, an ordered superferromagnetic state is unfavored and hence frustration due to dipole-dipole interaction is in effect and thus favors a superspin glass state.

In summary, trench-patterned Si substrates were used as templates to guide NP self-assembly. GISAXS measurements show that NP coherent structure along the trench direction can be observed, while in the direction perpendicular to the trench, no coherent structure is observable. Hysteresis loops on these systems show a large magnetic preferential direction along the trench, which is induced by magnetic shape anisotropy. The electron holography provides the evidence of the superferromagnetic order of NPs at the remanent state after the application of a saturation magnetic field along the trenches, while it shows random magnetic state after the application of a saturation magnetic field perpendicular to the trenches. Memory effect measurements in both parallel and perpendicular geometry reveal that a superspin glass state occurs in the perpendicular geometry, in the parallel one the emerging superferromagnetic order suppresses the superspin glass state partially.
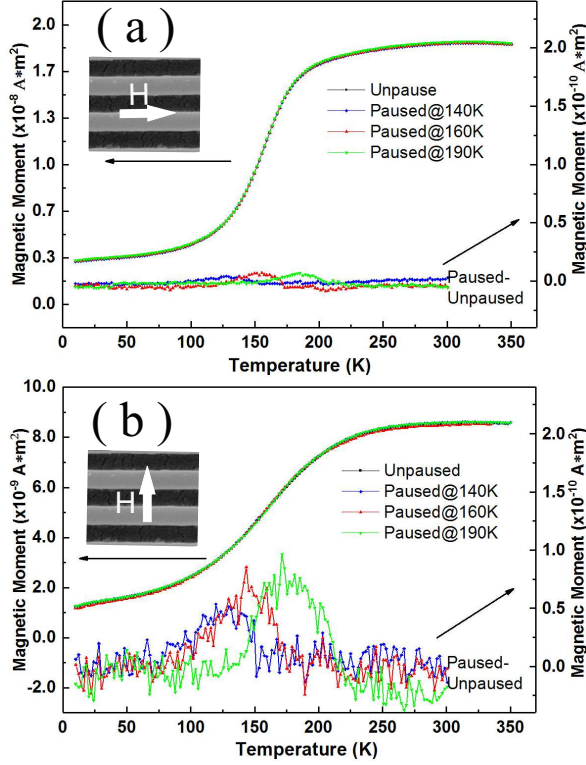
Figure 6.10: Memory effect for the field application (a) parallel and (b) perpendicular to the long axis of the trenches as indicated in the inset. For both (a) and (b), the regular ZFC curve and the ZFC curves obtained with an aging stop at 140 K and subsequently at 160 K and 190 K, respectively. The ZFC curves measured at a field of 5 mT are indicated by the left Y-axis. The curves obtained by the subtraction of paused ZFC curves from regular ZFC curves, $\Delta M = M_{reg}^{ZFC} - M_{aging}^{ZFC}$, are indicated by the right Y-axis. Every subtraction corresponds to the same color of ZFC curves.

Chapter 7

Summary and Outlook

The main task of the thesis was to investigate the MEC effects in an artificial multiferroic composite of iron oxide NPs and BTO.

Iron oxide NPs and BTO thin film is the first system for the MEC effect investigations. Ferroelectric BTO films on Nb-doped STO substrates were prepared using PLD method. X-ray diffraction and reflectivity were used to check the structural properties of these films which indicate a good film quality in terms of crystalline and surface. The morphology of the self-assembled NPs on BTO films were characterized by SEM and GISAXS, both methods show that NPs cannot form long-range-ordered structures on films with rough surface. Electrically manipulated MEC effects were observed for the sample Nb-doped STO / BTO / NP / BTO / Au. Harden effect and the manipulation of the magnetization of the NPs under DC electric field were probed. ME coefficient of the sample shows electric field amplitude and frequency dependence and abrupt signal jump at BTO phase transition. Strain and interface charge co-mediated ME mechanism is proposed for the MEC effects.

Iron oxide NPs and BTO substrate is the other system used for the MEC effects investigations. NPs were self-assembled on BTO substrate using spin coating method. The morphology of the NPs were characterized by SEM and GISAXS. Both techniques show a hexagonal close-packed crystalline order of the NP monolayer self-assembled on BTO substrates. The magnetization of the sample shows there is no MEC effect in this state. MEC effects were observed in the sample Au / BTO / Ti / NP / Au. STEM experiment provide the information about the layer structure of the sample. Magnetization, coercivity, remanent magnetization and MEACS signal as a function of temperature show abrupt jumps at the BTO phase transition temperatures. NP Multilayers on BTO substrate were prepared using dropcasting methods. The MEC effects are reduced due to the strain being too little to fully affect each NP layer.

The great success of altering magnetism by electric field has more wide applications in energy-efficient devices. The application of an DC electric field leads to a change of magnetic anisotropy represented by the change of H_c and M_r value. DC electric field manipulated the magnetization of the NPs in a butterfly shape indicating a strain induced MEC. AC electric field manipulated the MEACS sig-

nal as a function of temperature show abrupt jumps at the BTO phase transition temperatures.

Apart from MEC effects investigations, iron oxide NPs self-assembled in trenches of patterned Si substrates were employed to investigate the magnetic anisotropy and memory effect. GISAXS and electron holography were used to characterize the local structure and magnetic structure of the NPs in the trenches. Both techniques show NP parallel to trench direction behavior as long- rang-ordered coherent local and magnetic structure, while measuring NPs perpendicular to the trenches, no ordered local structure or magnetic structure is observable. Meanwhile, weak memory effect were observed in parallel direction and strong memory effect was observed in perpendicular direction. The strong memory effect is due to the strong SSG state and the weak memory effect might be due to that the superferromagnetic order of NPs suppress the SSG state.

In order to get a detailed picture of the strain mediated MEC effect, more detailed investigations of the structural properties of the BTO substrate and film are required. I.e. how much strain is induced from the ferroelectric domain deformation of BTO substrates? Which takes a dominate role in strain generation, the domain deformation or the lattice distortion? Visualizing the ferroelectric domain structures by polarized light microscopy is a simple but practical technique. Also a collimated laser system can provide some information about the domain structures, for example, coordinating the reflected beam pattern of the domain as shown in Figure 4.4 would be helpful to investigate the in-situ domain structure changes depending on temperature or electric field. However, methods which are used to quantitatively analyze the domain deformation have to be found. It would simplify an interpretation, if a method to create a reproducible domain state in the BTO substrate could be found. A more detailed investigation of the structural variation of the NPs under strain is mandatory. X-ray and neutron reflectivity only provide the in-depth nuclear and magnetic profiles, while the lateral correlation of the nuclear and magnetic profile of NP monolayers and BTO system need to be performed by GISAXS and GISANS, which will be very helpful for the complete understanding of the whole procedures of MEC effects, However, because the Au layer is largely intransparent to X-ray, a substitution is need to be find for the ME system and the electric field environment for GALAXI needs to be implemented. For Grazing Incidence Small Angle Neutron Scattering (GISANS) measurements, the magnetic signal of the sample needs to be enhanced. For example, it might be a choice that overlaying several samples together or finding the optimized number of NP layers to balance both the magnetic signal and the MEC effect, which are strong enough to be detected.

In order to further clarify the mechanism of the BTO film and iron oxide NP system, various systems with different thickness BTO film and NP layer will be benefit for the investigation of the two mechanisms. Alternatively, the insert of metallic layers between FM and FE layers to avoid the screening charge effect is helpful to realize the pure strain-mediated MEC effect [107, 23].

The understanding of the direction dependent memory effect needs further evi-

dences from experiments and simulations. For example, the simulation of the interaction energy between NPs and the one between trenches will help us to understand the spin structure of each NPs and furthermore, to determine the magnetic state of the collective NPs.

Nevertheless, the works in this thesis opens up viable possibilities for fabricating novel energy-efficient electronic devices by self-assembly techniques, for example ME data storage devices or ME sensors.

Part of the work in this thesis is published in the journal of *Nanoscale*.

Chapter 8

Bibliography

[1] M. Fiebig, V. V. Eremenko, and I. E. Chupis, *Magnetoelectric Interaction Phenomena in Crystals: Proceedings of the NATO ARW on Magnetoelectric Interaction Phenomena in Crystals, Sudak, Ukraine from 21 to 24 September 2003*.   Springer Science & Business Media, 2004, vol. 164.

[2] C.-W. Nan, M. Bichurin, S. Dong, D. Viehland, and G. Srinivasan, "Multiferroic magnetoelectric composites: historical perspective, status, and future directions," *Journal of Applied Physics*, vol. 103, no. 3, p. 1, 2008.

[3] G. Lawes and G. Srinivasan, *J. Phys. D: Appl. Phys.*, vol. 44, no. 24, p. 243001, 2011.

[4] W. Eerenstein, N. Mathur, and J. F. Scott, "Multiferroic and magnetoelectric materials," *Nature*, vol. 442, no. 7104, p. 759, 2006.

[5] M. Fiebig, "Revival of the magnetoelectric effect," *J. Phys. D: Appl. Phys.*, vol. 38, no. 8, p. R123, 2005.

[6] W. Kleemann and C. Binek, *Multiferroic and magnetoelectric materials, Magnetic Nanostructures*, H. Zabel and M. Farle, Eds. Springer Berlin Heidelberg, 2013, vol. 246.

[7] M. Bibes, A. Barthélémy *et al.*, "Towards a magnetoelectric memory," *Nat. Mater.*, vol. 7, p. 425, 2008.

[8] J. Scott, "Data storage: Multiferroic memories," *Nature materials*, vol. 6, no. 4, p. 256, 2007.

[9] Y. Tian, S. R. Bakaul, and T. Wu, "Oxide nanowires for spintronics: materials and devices," *Nanoscale*, vol. 4, no. 5, p. 1529, 2012.

[10] T. Kimura, T. Goto, H. Shintani, K. Ishizaka, T.-h. Arima, and Y. Tokura, "Magnetic control of ferroelectric polarization," *Nature*, vol. 426, no. 6962, p. 55, 2003.

[11] J. Wang, J. Neaton, H. Zheng, V. Nagarajan, S. Ogale, B. Liu, D. Viehland, V. Vaithyanathan, D. Schlom, U. Waghmare *et al.*, "Epitaxial BiFeO$_3$ multiferroic thin film heterostructures," *Science*, vol. 299, no. 5613, p. 1719, 2003.

[12] T. Goto, T. Kimura, G. Lawes, A. Ramirez, and Y. Tokura, "Ferroelectricity and giant magnetocapacitance in perovskite rare-earth manganites," *Physical Review Letters*, vol. 92, no. 25, p. 257201, 2004.

[13] T. Lottermoser, T. Lonkai, U. Amann, D. Hohlwein, J. Ihringer, and M. Fiebig, "Magnetic phase control by an electric field," *Nature*, vol. 430, no. 6999, p. 541, 2004.

[14] J. Van Suchtelen, "Product properties: a new application of composite materials," *Philips Res. Rep*, vol. 27, no. 1, p. 28, 1972.

[15] C.-W. Nan, "Magnetoelectric effect in composites of piezoelectric and piezomagnetic phases," *Physical Review B*, vol. 50, no. 9, p. 6082, 1994.

[16] S. Sahoo, S. Polisetty, C.-G. Duan, S. S. Jaswal, E. Y. Tsymbal, and C. Binek, *Physical Review B*, vol. 76, no. 9, p. 092108, 2007.

[17] G. Radaelli, D. Petti, E. Plekhanov, I. Fina, P. Torelli, B. Salles, M. Cantoni, C. Rinaldi, D. Gutiérrez, G. Panaccione *et al.*, *Nature Communication*, vol. 5, p. 3404, 2014.

[18] T. Nan, Z. Zhou, M. Liu, X. Yang, Y. Gao, B. A. Assaf, H. Lin, S. Velu, X. Wang, H. Luo *et al.*, *Scientific Reports*, vol. 4, p. 3688, 2014.

[19] G. Radaelli, D. Petti, M. Cantoni, C. Rinaldi, and R. Bertacco, *J. Appl. Phys.*, vol. 115, no. 17, p. 172604, 2014.

[20] M. Schmitz, "Strain and electric field mediated manipulation of magnetism in la (1-x) Sr$_x$MnO$_3$ / BaTiO$_3$ heterostructures," Ph.D. dissertation, Universität RWTH Aachen, Fakultät für Physik, 2015.

[21] Y. Koo, K. Song, Y. Jo, J. Cho, Y. Jeong, T. Koo, H. Lee, T. Jang, J. Jung, and N. Hur, "Strain-induced magnetoelectric coupling in BaTiO$_3$/Fe$_3$O$_4$ core/shell nanoparticles," *Applied Physics Letters*, vol. 94, no. 6, p. 032903, 2009.

[22] K. Raidongia, A. Nag, A. Sundaresan, and C. Rao, "Multiferroic and magnetoelectric properties of core-shell CoFe$_2$O$_4$@BaTiO$_3$ nanocomposites," *Applied Physics Letters*, vol. 97, no. 6, p. 062904, 2010.

[23] H. K. Kim, L. T. Schelhas, S. Keller, J. L. Hockel, S. H. Tolbert, and G. P. Carman, "Magnetoelectric control of superparamagnetism," *Nano Letters*, vol. 13, no. 3, p. 884, 2013.

[24] S. Bedanta, O. Petracic, and W. Kleemann, *Supermagnetism, Handbook of Magnetic Materials*, K.J.H.Buschow, Ed., vol. 23, Ed. K. J. H. Buschow, 2015.

[25] S. Disch, E. Wetterskog, R. P. Hermann, G. Salazar-Alvarez, P. Busch, T. Brückel, L. Bergström, and S. Kamali, "Shape induced symmetry in self-assembled mesocrystals of iron oxide nanocubes," *Nano Letters*, vol. 11, no. 4, p. 1651, 2011.

[26] D. Mishra, M. Benitez, O. Petracic, G. B. Confalonieri, P. Szary, F. Brüssing, K. Theis-Bröhl, A. Devishvili, A. Vorobiev, O. Konovalov *et al.*, "Self-assembled iron oxide nanoparticle multilayer: x-ray and polarized neutron reflectivity," *Nanotechnology*, vol. 23, no. 5, p. 055707, 2012.

[27] J. Zhuang, H. Wu, Y. Yang, and Y. C. Cao, "Supercrystalline colloidal particles from artificial atoms," *J. Am. Chem. Soc*, vol. 129, no. 46, p. 14166, 2007.

[28] J. Xiao, Z. Li, X. Ye, Y. Ma, and L. Qi, "Self-assembly of gold nanorods into vertically aligned, rectangular microplates with a supercrystalline structure," *Nanoscale*, vol. 6, no. 2, p. 996, 2014.

[29] Z. Tang and N. A. Kotov, "One-dimensional assemblies of nanoparticles: preparation, properties, and promise," *Advanced Materials*, vol. 17, no. 8, p. 951, 2005.

[30] D. Xia, A. Biswas, D. Li, and S. R. Brueck, "Directed self-assembly of silica nanoparticles into nanometer-scale patterned surfaces using spin-coating," *Advanced Materials*, vol. 16, no. 16, p. 1427, 2004.

[31] D. Xia and S. Brueck, "A facile approach to directed assembly of patterns of nanoparticles using interference lithography and spin coating," *Nano Letters*, vol. 4, no. 7, pp. 1295–1299, 2004.

[32] X. Fan, Q. Hao, R. Jin, H. Huang, Z. Luo, X. Yang, Y. Chen, X. Han, M. Sun, Q. Jing *et al.*, "Assembly of gold nanoparticles into aluminum nanobowl array," *Scientific Reports*, vol. 7, 2017.

[33] Y. S. J. Y. W. Yong-Jun Oh, Caroline A. Ross and C. V. Thompson, "Cobalt nanoparticle srrays made by ttemplated solid-state fewetting," *Small*, vol. 5, no. 7, p. 860, 2009.

[34] Y. Lee, H. Lee, P. B. Messersmith, and T. G. Park, "A bioinspired polymeric template for 1d assembly of metallic nanoparticles, semiconductor quantum dots, and magnetic nanoparticles," *Macromolecular Rapid Communications*, vol. 31, no. 24, p. 2109, 2010.

[35] R. M. Penner, "Mesoscopic metal particles and wires by electrodeposition," 2002.

[36] M. Kang, Y. Yuwen, W. Hu, S. Yun, K. Mahalingam, B. Jiang, K. Eyink, E. Poutrina, K. Richardson, and T. S. Mayer, "Self-organized freestanding one-dimensional au nanoparticle arrays," *ACS nano*, vol. 21, p. 5844, 2017.

[37] T. Jonsson, J. Mattsson, C. Djurberg, F. Khan, P. Nordblad, and P. Svedlindh, "Aging in a magnetic particle system," *Physical Review Letters*, vol. 75, no. 22, p. 4138, 1995.

[38] S. Sahoo, O. Petracic, C. Binek, W. Kleemann, J. Sousa, S. Cardoso, and P. Freitas, "Superspin-glass nature of discontinuous co 80 fe 20/al 2 o 3 multilayers," *Physical Review B*, vol. 65, no. 13, p. 134406, 2002.

[39] M. Sasaki, P. Jönsson, H. Takayama, and H. Mamiya, "Aging and memory effects in superparamagnets and superspin glasses," *Physical Review B*, vol. 71, no. 10, p. 104405, 2005.

[40] O. Petracic, "Superparamagnetic nanoparticle ensembles," *Superlattices and Microstructures*, vol. 47, no. 5, pp. 569–578, 2010.

[41] S. Blundell, "Magnetism in condensed matter," 2003.

[42] ——, *magnetism in condensed matter*.   Oxford University Press, 2003.

[43] K. Binder and A. P. Young, "Spin glasses: Experimental facts, theoretical concepts, and open questions," *Reviews of Modern Physics*, vol. 58, no. 4, p. 801, 1986.

[44] J. A. Mydosh, *Spin glasses: an experimental introduction.*   Taylor and Francis, 1993.

[45] T. Taniguchi, K. Yamanaka, H. Sumioka, T. Yamazaki, Y. Tabata, and S. Kawarazaki, "Direct observation of chiral susceptibility in the canonical spin glass aufe," *Physical Review Letters*, vol. 93, no. 24, p. 246605, 2004.

[46] D. Chu, G. Kenning, and R. Orbach, "Dynamic measurements in a heisenberg spin glass: Cumn," *Physical Review Letters*, vol. 72, no. 20, p. 3270, 1994.

[47] B. A. Berg and T. Celik, "New approach to spin-glass simulations," *Physical Review Letters*, vol. 69, no. 15, p. 2292, 1992.

[48] H. Kawamura, "Anomalous hall effect as a probe of the chiral order in spin glasses," *Physical Review Letters*, vol. 90, no. 4, p. 047202, 2003.

[49] S. Bedanta and W. Kleemann, "Supermagnetism," *Journal of Physics D: Applied Physics*, vol. 42, no. 1, p. 013001, 2008.

[50] B. Aslibeiki, P. Kameli, H. Salamati, M. Eshraghi, and T. Tahmasebi, "Superspin glass state in $MnFe_2O_4$ nanoparticles," *Journal of Magnetism and Magnetic Materials*, vol. 322, no. 19, p. 2929, 2010.

[51] J. Osborn, "Demagnetizing factors of the general ellipsoid," *Physical review*, vol. 67, no. 11, p. 351, 1945.

[52] D. Garanin and H. Kachkachi, "Surface contribution to the anisotropy of magnetic nanoparticles," *Physical Review Letters*, vol. 90, no. 6, p. 065504, 2003.

[53] M. Respaud, J. Broto, H. Rakoto, A. Fert, L. Thomas, B. Barbara, M. Verelst, E. Snoeck, P. Lecante, A. Mosset *et al.*, "Surface effects on the magnetic properties of ultrafine cobalt particles," *Physical Review B*, vol. 57, no. 5, p. 2925, 1998.

[54] Y. Labaye, O. Crisan, L. Berger, J. Greneche, and J. Coey, "Surface anisotropy in ferromagnetic nanoparticles," *Journal of Applied Physics*, vol. 91, no. 10, p. 8715, 2002.

[55] S. Chikazumi, *Physics of magnetism*. Wiley, 1964.

[56] Wikipedia, "Inverse magnetostrictive effect," https://en.wikipedia.org/wiki/Inverse_magnetostrictive_effect#cite_note-Bozorth1951-1, accessed September 4, 2017.

[57] B. D. Cullity and C. D. Graham, *Introduction to magnetic materials*. John Wiley & Sons, 2011.

[58] O. Petracic, "Superparamagnetic nanoparticle ensembles," *Superlattices and Microstructures*, vol. 47, no. 5, p. 569, 2010.

[59] R. Skomski, "Nanomagnetics," *Journal of Physics: Condensed Matter*, vol. 15, no. 20, p. R841, 2003.

[60] R. Cornell and U. Schwertmann, "The iron oxides," *Structure, properties*, 2001.

[61] C. McCammon and L.-g. Liu, "The effects of pressure and temperature on nonstoichiometric wüstite, Fe_xO: The iron-rich phase boundary," *Physics and Chemistry of Minerals*, vol. 10, no. 3, p. 106, 1984.

[62] D. S. Tannhauser, "Conductivity in iron oxides," *Journal of Physics and Chemistry of Solids*, vol. 23, no. 1, p. 25, 1962.

[63] I. für Elektrische Messtechnik und Grundlagen der Elektrotechnik, "Figure: Wüstite crystal structure." http://www.emg.tu-bs.de/forschung/material/wuestite_e.html, accessed September 4, 2017.

[64] W. Roth, "Defects in the crystal and magnetic structures of ferrous oxide," *Acta Crystallographica*, vol. 13, no. 2, p. 140, 1960.

[65] D. J. Dunlop and Ö. Özdemir, *Rock magnetism: fundamentals and frontiers*. Cambridge university press, 2001, vol. 3.

[66] I. für Elektrische Messtechnik und Grundlagen der Elektrotechnik, "Fig. 1: Maghemite crystal structure with the space group of Fd$_3$m cubic lattice." http://www.emg.tu-bs.de/forschung/material/maghemite_e.html, accessed September 4, 2017.

[67] Y. Cudennec and A. Lecerf, "Topotactic transformations of goethite and lepidocrocite into hematite and maghemite," *Solid State Sciences*, vol. 7, no. 5, p. 520, 2005.

[68] H. F. Kay and P. Vousden, *The London, Edinburgh, and Dublin Philosophical Magazine and Journal of Science*, vol. 40, no. 309, p. 1019, 1949.

[69] A. delicated to Science of Mothin, "Theory and applications of piezo actuators and pzt nanopositioning systems," https://www.aerotech.com/product-catalog/piezo-nanopositioners/piezo-engineering-tutorial.aspx, accessed September 5, 2017.

[70] H. F. Kay and P. Vousden, "Xcv. symmetry changes in barium titanate at low temperatures and their relation to its ferroelectric properties," *The London, Edinburgh, and Dublin Philosophical Magazine and Journal of Science*, vol. 40, no. 309, p. 1019, 1949.

[71] A. F. Devonshire, "Xcvi. theory of barium titanate: Part i," *The London, Edinburgh, and Dublin Philosophical Magazine and Journal of Science*, vol. 40, no. 309, p. 1040, 1949.

[72] W. Zhong, D. Vanderbilt, and K. Rabe, "First-principles theory of ferroelectric phase transitions for perovskites: The case of BaTiO$_3$," *Physical Review B*, vol. 52, no. 9, p. 6301, 1995.

[73] M. E. Lines and A. M. Glass, *Principles and applications of ferroelectrics and related materials*. Oxford University Press, 1977.

[74] E. Burcsu, G. Ravichandran, and K. Bhattacharya, "Large electrostrictive actuation of barium titanate single crystals," *Journal of the Mechanics and Physics of Solids*, vol. 52, no. 4, p. 823, 2004.

[75] S.-E. Park, S. Wada, L. Cross, and T. R. Shrout, "Crystallographically engineered BaTiO$_3$ single crystals for high-performance piezoelectrics," *Journal of Applied Physics*, vol. 86, no. 5, p. 2746, 1999.

[76] M. Caspari and W. Merz, "The electromechanical behavior of bati o 3 single-domain crystals," *Physical Review*, vol. 80, no. 6, p. 1082, 1950.

[77] J. Kreisel and M. Kenzelmann, "Multiferroics-the challenge of coupling magnetism and ferroelectricity," *Europhysics News*, vol. 40, no. 5, p. 17, 2009.

[78] S. Markus, *starin and electric field mediated manipulation of magnetism in $SrTiO_3/BaTiO_3$ heterostructures*. Forschungszentrum Jülich GmbH, 2016, vol. 129.

[79] R. Ramesh and N. A. Spaldin, "Multiferroics: progress and prospects in thin films," *Nature materials*, vol. 6, no. 1, p. 21, 2007.

[80] L. Wang, O. Petracic, E. Kentzinger, U. Rücker, S. Markus, X.-k. Wei, M. Heggen, and T. Brückel, "Strain and electric-field control of magnetism in supercrystalline iron oxide nanoparticle-$BaTiO_3$composites," *Nanoscale*, vol. 9, p. 12957, 2017.

[81] G. Radaelli, D. Petti, M. Cantoni, C. Rinaldi, and R. Bertacco, "Absence of strain-mediated magnetoelectric coupling at fully epitaxial $Fe/BaTiO_3$ interface," *Journal of Applied Physics*, vol. 115, no. 17, p. 172604, 2014.

[82] H. Katsura, A. V. Balatsky, and N. Nagaosa, "Dynamical magnetoelectric coupling in helical magnets," *Physical Review Letters*, vol. 98, no. 2, p. 027203, 2007.

[83] T. Brückel, G. Heger, D. Richter, G. Roth, and R. Zorn, *Neutron Scattering Lectures of the JCNS Laborator Course held at Forschungszentrum Jülich and the research reactor FRM II of TU Munich In cooperation with RWTH Aachen and University of Münster*. Forschungszentrum Jülich, 2012, vol. 39.

[84] J. Lekner, *Theory of reflection*. Springer, 1987.

[85] L. G. Parratt, "Surface studies of solids by total reflection of x-rays," *Physical review*, vol. 95, no. 2, p. 359, 1954.

[86] M. Björck and G. Andersson, "Genx: an extensible x-ray reflectivity refinement program utilizing differential evolution," *Journal of Applied Crystallography*, vol. 40, no. 6, p. 1174, 2007.

[87] S. Bader, "Colloquium: Opportunities in nanomagnetism," *Reviews of Modern Physics*, vol. 78, no. 1, p. 1, 2006.

[88] J. Martın, J. Nogues, K. Liu, J. Vicent, and I. K. Schuller, "Ordered magnetic nanostructures: fabrication and properties," *Journal of magnetism and magnetic materials*, vol. 256, no. 1, p. 449, 2003.

[89] D. McMullan, "Scanning electron microscopy 1928–1965," *Scanning*, vol. 17, no. 3, p. 175, 1995.

[90] Quantum Design, San Diego, CA, "Magnetic property measurement system hardware reference manual," vol. 1, p. 16.

[91] P. Borisov, A. Hochstrat, V. Shvartsman, and W. Kleemann, *Rev. Sci. Instrum.*, vol. 78, no. 10, p. 106105, 2007.

[92] A. Baji, Y.-W. Mai, Q. Li, and Y. Liu, "Nanoscale investigation of ferroelectric properties in electrospun barium titanate/polyvinylidene fluoride composite fibers using piezoresponse force microscopy," *Composites Science and Technology*, vol. 71, no. 11, p. 1435, 2011.

[93] R. Rhodes, *Acta Cryst.*, vol. 4, no. 2, p. 105, 1951.

[94] M. Benitez, D. Mishra, P. Szary, G. B. Confalonieri, M. Feyen, A. Lu, L. Agudo, G. Eggeler, O. Petracic, and H. Zabel, "Structural and magnetic characterization of self-assembled iron oxide nanoparticle arrays," *Journal of Physics: Condensed Matter*, vol. 23, no. 12, p. 126003, 2011.

[95] G. Wilbs, T. Brückel, and R. Waser, "Magnetic proximity effects in nanoparticle composite systems and macrocrystals," Universität RWTH Aachen, Fakultät für Materials, Tech. Rep., 2017.

[96] H. Tian, T. Qu, L. Luo, J. Yang, S. Guo, H. Zhang, Y. Zhao, and J. Li, *Applied Physics Letters*, vol. 92, no. 6, p. 63507, 2008.

[97] R. McCurrie and G. Carswell, *Philosophical Magazine*, vol. 23, no. 182, p. 333, 1971.

[98] M. Lund, W. Macedo, K. Liu, J. Nogués, I. K. Schuller, and C. Leighton, *Physical Review B*, vol. 66, no. 5, p. 054422, 2002.

[99] J.-M. Hu, C.-W. Nan, and L.-Q. Chen, *Physical Review B*, vol. 83, no. 13, p. 134408, 2011.

[100] H. M. Urquhart and J. Goldman, "Magnetostrictive effects in an antiferromagnetic hematite crystal," *Physical Review*, vol. 101, no. 5, p. 1443, 1956.

[101] B. Jaffe, *Piezoelectric ceramics*.   Elsevier, 2012, vol. 3.

[102] A. Millis, T. Darling, and A. Migliori, "Quantifying strain dependence in "colossal" magnetoresistance manganites," *Journal of Applied Physics*, vol. 83, no. 3, p. 1588, 1998.

[103] F. Tsui, M. Smoak, T. Nath, and C. Eom, "Strain-dependent magnetic phase diagram of epitaxial la 0.67 sr 0.33 mno 3 thin films," *Applied Physics Letters*, vol. 76, no. 17, p. 2421, 2000.

[104] M. K. Lee, T. K. Nath, C.-B. Eom, M. C. Smoak, and F. Tsui, "Strain modification of epitaxial perovskite oxide thin films using structural transitions of ferroelectricBaTiO$_3$ substrate," *Applied Physics Letters*, vol. 77, no. 22, p. 3547, 2000.

[105] S. Brivio, D. Petti, R. Bertacco, and J. Cezar, "Electric field control of magnetic anisotropies and magnetic coercivity in Fe/BaTiO$_3$ (001) heterostructures," *Applied Physics Letters*, vol. 98, no. 9, p. 092505, 2011.

[106] G. Venkataiah, Y. Shirahata, M. Itoh, and T. Taniyama, "Manipulation of magnetic coercivity of fe film in $Fe/BaTiO_3$ heterostructure by electric field," *Applied Physics Letters*, vol. 99, no. 10, p. 102506, 2011.

[107] L. Shu, Z. Li, J. Ma, Y. Gao, L. Gu, Y. Shen, Y. Lin, and C. Nan, "Thickness-dependent voltage-modulated magnetism in multiferroic heterostructures," *Applied Physics Letters*, vol. 100, no. 2, p. 022405, 2012.

[108] R. Lefever, "4.1. 1.4 magnetostriction and elastic constants," in *Part B: Spinels, Fe Oxides, and Fe-Me-O Compounds*. Springer, 1980, p. 62.

[109] E.-L. Salabas, "Structural and magnetic investigations of magnetic nanoparticles and core-shell colloids," Ph.D. dissertation, Universität Duisburg-Essen, Fakultät für Physik, 2004.

[110] X. Deng, X. Wang, H. Wen, A. Kang, Z. Gui, and L. Li, "Phase transitions in nanocrystalline barium titanate ceramics prepared by spark plasma sintering," *Journal of the American Ceramic Society*, vol. 89, no. 3, p. 1059, 2006.

[111] S. J. Trithaveesak O. and B. Ch., "Ferroelectric properties of epitaxial $BaTiO_3$ thin films and heterostructures on different substrates," *Journal of applied Physics*, vol. 98, no. 11, p. 114101, 2005.

[112] M. El Marssi, F. Le Marrec, I. Lukyanchuk, and M. Karkut, "Ferroelectric transition in an epitaxial barium titanate thin film: Raman spectroscopy and x-ray diffraction study," *Journal of Applied Physics*, vol. 94, no. 5, p. 3307, 2003.

[113] J. Karczewski, B. Riegel, M. Gazda, P. Jasinski, and B. Kusz, "Electrical and structural properties of nb-doped srtio3 ceramics," *Journal of Electroceramics*, vol. 24, no. 4, p. 326, 2010.

[114] G. Jonker, "Some aspects of semiconducting barium titanate," *Solid-State Electronics*, vol. 7, no. 12, p. 895, 1964.

[115] H. J. Molegraaf, J. Hoffman, C. A. Vaz, S. Gariglio, D. Van Der Marel, C. H. Ahn, and J.-M. Triscone, "Magnetoelectric effects in complex oxides with competing ground states," *Advanced materials*, vol. 21, no. 34, p. 3470, 2009.

[116] G. Radaelli, D. Petti, E. Plekhanov, I. Fina, P. Torelli, B. Salles, M. Cantoni, C. Rinaldi, D. Gutiérrez, G. Panaccione *et al.*, "Electric control of magnetism at the $Fe/BaTiO_3$ interface," *Nature communications*, vol. 5, p. 3404, 2014.

[117] T. Nan, Z. Zhou, M. Liu, X. Yang, Y. Gao, B. A. Assaf, H. Lin, S. Velu, X. Wang, H. Luo *et al.*, "Quantification of strain and charge co-mediated magnetoelectric coupling on ultra-thin permalloy/pmn-pt interface," *Scientific reports*, vol. 4, 2014.

[118] J.-M. Hu, C.-W. Nan, and L.-Q. Chen, "Size-dependent electric voltage con-trolled magnetic anisotropy in multiferroic heterostructures: Interface-charge and strain comediated magnetoelectric coupling," *Physical Review B*, vol. 83, no. 13, p. 134408, 2011.

[119] S. R. Spurgeon, J. D. Sloppy, D. M. Kepaptsoglou, P. V. Balachandran, S. Ne-jati, J. Karthik, A. R. Damodaran, C. L. Johnson, H. Ambaye, R. Goyette *et al.*, "Thickness-dependent crossover from charge-to strain-mediated mag-netoelectric coupling in ferromagnetic/piezoelectric oxide heterostructures," *ACS nano*, vol. 8, no. 1, p. 894, 2013.

[120] Z. Li, J. Hu, L. Shu, Y. Gao, Y. Shen, Y. Lin, and C. Nan, "Thickness-dependent converse magnetoelectric coupling in bi-layered Ni/PZT thin films," *Journal of Applied Physics*, vol. 111, no. 3, p. 033918, 2012.

[121] D. Lu, J. J. Kan, E. E. Fullerton, and Z. Liu, "Enhancing spontaneous emission rates of molecules using nanopatterned multilayer hyperbolic metamaterials," *Nature nanotechnology*, vol. 9, no. 1, p. 48, 2014.

[122] S. Park, D. H. Lee, and T. P. Russell, "Self-assembly of block copolymers on flexible substrates," *Advanced Materials*, vol. 22, no. 16, p. 1882, 2010.

[123] S. Park, D. H. Lee, J. Xu, B. Kim, S. W. Hong, U. Jeong, T. Xu, and T. P. Russell, "Macroscopic 10-terabit–per–square-inch arrays from block copoly-mers with lateral order," *Science*, vol. 323, no. 5917, pp. 1030–1033, 2009.

[124] H. H. Solak, C. Dais, and F. Clube, "Displacement talbot lithography: a new method for high-resolution patterning of large areas," *Optics express*, vol. 19, no. 11, p. 10686, 2011.

[125] K. Butter, P. Bomans, P. Frederik, G. Vroege, and A. Philipse, "Direct obser-vation of dipolar chains in iron ferrofluids by cryogenic electron microscopy," *Nature materials*, vol. 2, no. 2, pp. 88–91, 2003.

[126] J. Ku, D. M. Aruguete, A. P. Alivisatos, and P. L. Geissler, "Self-assembly of magnetic nanoparticles in evaporating solution," *Journal of the American Chemical Society*, vol. 133, no. 4, pp. 838–848, 2010.

[127] V. Salgueiriño-Maceira, M. A. Correa-Duarte, A. Hucht, and M. Farle, "One-dimensional assemblies of silica-coated cobalt nanoparticles: Magnetic pearl necklaces," *Journal of magnetism and magnetic materials*, vol. 303, no. 1, pp. 163–166, 2006.

[128] T. Wen, D. Zhang, Q. Wen, H. Zhang, Y. Liao, Q. Li, Q. Yang, F. Bai, and Z. Zhong, "Magnetic nanoparticle assembly arrays prepared by hierarchical self-assembly on a patterned surface," *Nanoscale*, vol. 7, no. 11, p. 4906, 2015.

[129] U. Wiedwald, M. Spasova, M. Farle, M. Hilgendorff, and M. Giersig, "Ferro-magnetic resonance of monodisperse Co particles," *Journal of Vacuum Science & Technology A: Vacuum, Surfaces, and Films*, vol. 19, no. 4, p. 1773, 2001.

[130] M. Varón, M. Beleggia, T. Kasama, R. Harrison, R. Dunin-Borkowski, V. Puntes, and C. Frandsen, "Dipolar magnetism in ordered and disordered low-dimensional nanoparticle assemblies," *Scientific reports*, vol. 3, 2013.

[131] R. E. Dunin-Borkowski, S. B. Newcomb, T. Kasama, M. R. McCartney, M. Weyland, and P. A. Midgley, "Conventional and back-side focused ion beam milling for off-axis electron holography of electrostatic potentials in transistors," *Ultramicroscopy*, vol. 103, no. 1, pp. 67–81, 2005.

[132] Y. Sahoo, M. Cheon, S. Wang, H. Luo, E. Furlani, and P. Prasad, "Field-directed self-assembly of magnetic nanoparticles," *The Journal of Physical Chemistry B*, vol. 108, no. 11, p. 3380, 2004.

[133] C. Liu and Z. J. Zhang, "Size-dependent superparamagnetic properties of mn spinel ferrite nanoparticles synthesized from reverse micelles," *Chemistry of Materials*, vol. 13, no. 6, p. 2092, 2001.

List of Figures

List of Tables

List of Acronyms

1D	One Dimensional
2D	Two Dimensional
3D	Three Dimensional
AF	AntiFerromagnetic
AFM	Atomic Force Microscopy
BTO	Barium Titanate
C	Cubic
CCMS	Closed Cycle Measurement System
EB	Exchange Bias
EDX	Energy Dispersive X-ray
EELS	Electron Energy Loss Spectroscopy
FC	Field Cooling
FE	FerroElectric
FERAMs	Ferroelectric Random Access Memories
FiM	Ferrimagnetic
FiM-FE	FerriMagnetic-FerroElectric
FM	Ferromagnetic
FM-FE	FerroMagnetic-FerroElectric
FOM	Factor of Merit
FW	Field Warming

GISANS	Grazing Incidence Small Angle Neutron Scattering
GISAXS	Grazing Incidence Small Angle X-ray Scattering
HAADF	High Angle Annular Dark Field
HCP	Hexagonal Close Packed
MACS	Magnetic AC Susceptibility
ME	MagnetoElectric
MEACS	MagnetoElectric AC Susceptibility
MBE	Molecular Beam Epitaxy
MEC	MagnetoElectric Coupling
MLZ	Heinz Maier-Leibnitz Zentrum
MPMS	Magnetic Property Measurement System
MRAMs	Magnetic Random Access Memories
mSLD	magnetic Scattering Length Density
Nb doped STO	Niobium doped Strontium Titanate
NP	NanoParticle
NPs	NanoParticles
nSLD	nuclear Scattering Length Density
O	Orthorhombic
PE	PiezoElectric
PFM	Piezoresponse Force Microscopy

PLD	Pulsed Laser Deposition
PNR	Polarized Neutron Reflectivity
PPMS	Physical Property Measurement System
R	Rhombohedral
RSO	Reciprocating Sample Option
SEM	Scanning Electron Microscopy
SG	Spin Glass
SPM	SuperParaMagnetic
SQUID	Superconducting Quantum Interference Device
SSG	SuperSpin Glass
STEM	Scanning Transmission Electron Microscopy
T	Tetragonal
VSM	Vibrating Sample Magnetometer
XRD	X-ray Diffractometry
XRR	X-ray reflectivity
YSZ	Yttrium Stabilized Zirconium
ZFC	Zero Field Cooling

Appendix

A. The unit evolution of α_{ME}

$$M_{ME} = \alpha_{ME} \cdot E$$

$$\Rightarrow \alpha_{ME} = \frac{M_{ME}}{E} = \frac{\mu_0 m'}{V} \cdot \frac{1}{E}$$

$$\Rightarrow \frac{s}{m} = \frac{emu}{m^3} \cdot \frac{1}{V/m}$$

$$\because T = \frac{emu}{m^3} \, and \, T = \frac{V \cdot S}{m^2}$$

$$\therefore emu = V \cdot s \cdot m$$

$$\therefore \frac{s}{m} = \frac{V \cdot s \cdot m}{m^3} \cdot \frac{m}{V}$$

$$\Rightarrow \alpha_{ME} = \frac{s}{m}$$

B. Nanoparticle data sheet

Ocean NanoTech, LLC
7964 Arjons Dr. Ste G, San Diego, CA 92126
Phone : (858) 689-8808; Fax: (858) 689-8809
E-mail: orders@oceannanotech.com

Cetificate of Analysis

Catalog number:	SOR-20
Product name:	Iron Oxide Nanocrystals with Oleic Acid Coating
Lot number:	010411
Solvent:	Chloroform / Toluene
Size tolerance:	±2.5 nm
Surface group:	Oleic Acid
Concentration:	25 mg/mL
Volume:	2 mL
Storage:	4-25°C
Shelf life:	08-14-2014

Analysis

PROPERTY	SPECIFICATIONS	METHOD
IO Size	20 nm	TEM
Absorbance	N/A	Spectrophotometry

TEM Image
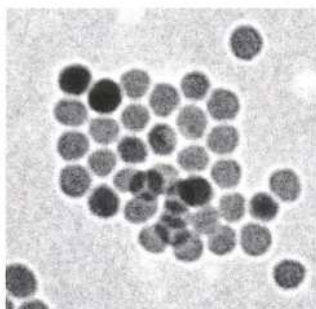
Absorption Spectra
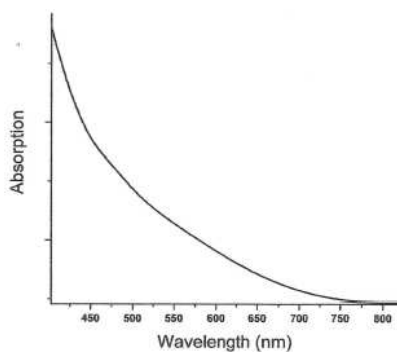
Figure 1: The 20 nm iron oxide nanoparticle data sheet from Ocean NanoTech

C. Preparation parameters of BTO film fabricated by PLD

Substrate: (001) Nb-doped STO 5 x 5 x 0.5 mm^3

Laser: 150 seconds @ 10 Hz (constant high voltage mode, HV=21,0 KV)

Heat: 4.5 A for 12 mins

Substrate angle: 37°

Oxygen flow: 30,00 ml/min

Vacuum state: 8E-4 mbar

D. Resistivity of Nb-doped SrTiO$_3$ substrate
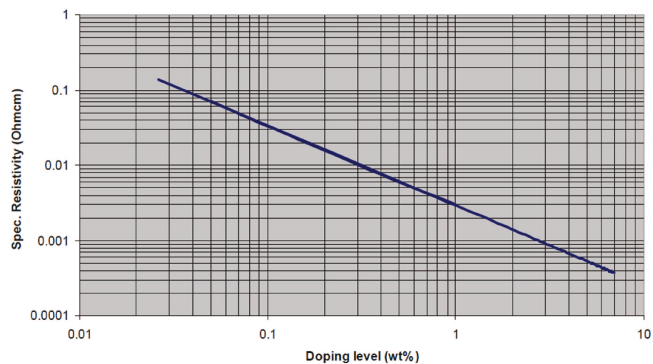
Figure 2: The resistivity vs. Nb doping level in SrTiO$_3$. Taken from Ref. [114]

E. Preparation parameters of EUV trenches
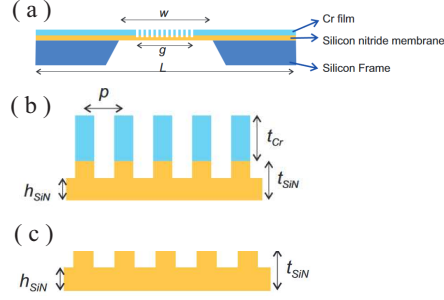
Figure 3: Diagram of the process for linear grating patterned silicon substrates. (a) to (c) corresponding to the first step to the third step correspondingly. where L is Si substrate frame width which is 5 to 10 nm, w is the silicon nitride membrane width 2 to 5nm, g is the grating width which is around 1mm, p is the grating period with a minimum value of 80nm, t_{Cr} is the thickness of the Cr film which is typically around 0 to 50nm. t_{SIN} is the thickness of silicon nitride membrane around 100 to 300nm, h_{SIN} is the thickness of the Remaining (support) silicon nitride which is smaller than 30nm Taken from [124].

Lithographie oxidmaske:
-resist coation (WB 5) UV6
-in Dehydriren at 413K for 90s
-cool down 60s
-UV6-06: 4000rpm (Prg4)
-relax resist for 60s
-soft bake at 413K for 60s
-Exposure Mask Aligner 3 (SUSS MA6)
-Mask Wash 5 in 0.2mJ/cm^2
Development:
-Post exposure bake: 413K for 90s
-immerse MF 24A for 60s
RIE oxide hard mask:
-RIE 4: Ar/CHF3 Oxid etch, endpoint by interferometer
-Resist stripping: DMSO/syslopentanone 15 min, Acetone 15 min, IPA 60s and DI 30s.
Dicing: -Protection resist: in dehydrieren 413K for 90s
-cool down 60s
-AZ5214: 4000rpm (Prg 4)
-relax resist 60s
-soft bake at 384K for 60s
-peel of foil, remove resist: Ac+IPA+DI

The parameters were taken from the sample preparation report of Eulitha company.

F. PNR Fit by default model
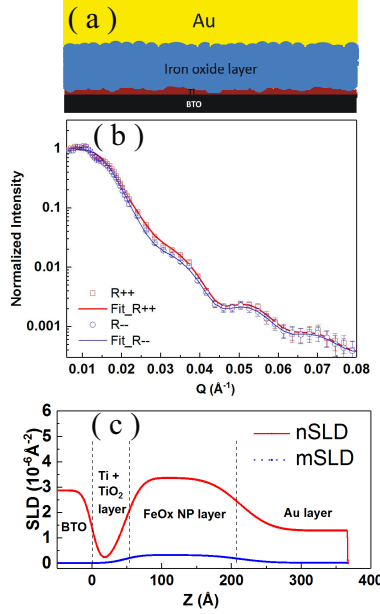
Figure 4: (a) The schematic spherical fitting model. (b) PNR data and the fitting of the BTO / Ti / NP / Au sample at 300 K at saturation field. (c) nSLD and mSLD profiles obtained by the fits via the model.

In the default model, BTO / Ti / NP / Au is regarded as a sample consisting of a infinite thick BTO layer, a Ti layer, a iron oxide layer, a Au layer and an ambient environment. Each layer is defined by several parameters: thickness (Th_i), roughness (Sig_i), nuclear scattering length density ($nSLD_i$), and two additional parameters, magnetic scattering length density ($mSLD_i$) and magnetic angle ($Magangle_i$), are used to define the magnetic profile of iron oxide layer.

The schematic diagram of the default model is displayed in Figure 4(a), the composition of the iron oxide layer is described as $(Fe_2O_3)_{0.8}$ $(Fe_3O_4)_{0.15}$ $(Fe_xO)_{0.05}$ and Ti layer is described as $0.8(Ti) \cdot 0.2(TiO_2)$, the reference thickness of each layer are obtained from the STEM observation and XRR measurement while the reference nSLD and mSLD values are calculated depending on the stoichiometry. Minimum and maximum values of 25% away from the reference value are defined to give the boundaries for the fit.

The PNR data of the R_{++} and R_{--} channels under the saturation magnetic field together with the corresponding fit via the default model are displayed in Figure 4(b). The default model gives a FOM factor of 0.029. The situation of the roughness of each interface is similar as the conclusion obtained from the fitting by spherical body model. Both SLDs show that at the initial state, the roughness

of BTO is reflected by the high slop in Z range from -50 Å to 0 Å, leading to the same condition of Ti layer. Meanwhile, the Au layer was a very smooth surface, and thus leading to a flat surface. The nSLD and mSLD with respect to the layer thickness obtained from the fitting is plotted in Figure 4.23(b) and (c) respectively. The results give a 5.20 nm Ti layer with a nSLD of $-0.042 \cdot 10^{-6} \mathring{A}^2$, a 15.80 nm iron oxide with a nSLD of $3.36 \cdot 10^{-6} \mathring{A}^2$, a mSLD of $0.44 \cdot 10^{-6} \mathring{A}^2$ and a 15.70 nm Au layer with a nSLD of $2.56 \cdot 10^{-6} \mathring{A}^2$. The roughness of each layer is indicated by the gradient slop of the SLD curve.
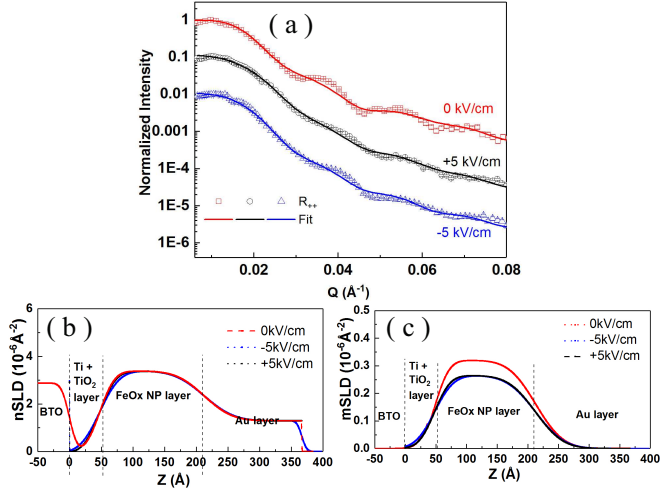
Figure 5: PNR data of the BTO / Ti / NP / Au sample at 300 K at coercive field. (a) Reflectivity and the fit for an electric field of 0 KV/cm, +5 KV/cm and -5 KV/cm (b) nSLD obtained from the fit (c) mSLD obtained from the fit. The dashed lines in (b) and (c) indicate the interfaces of layer.

The PNR data of the R_{++} and R_{--} channels under the coercive magnetic field together with the corresponding fit via the default model are displayed in Figure 5(a).

In the default model, all the parameters from last fitting are fixed except the mSLD of NP layer, the roughness of each layer and the nSLD of Au. The SLD profiles obtained from the best fit are shown in Figure 4.25(b) and (c), the similar conclusion on roughness of the saturation field is obtained. The nSLD of each layer keep basically the same as coercive magnetic field.

In the default model, only the roughness of each layer and the mSLD of NP layer were open, all the parameters were fixed from last fitting. Figure 5(b) and (c) show the nSLD and mSLD for each layer. The results give a 5.20 nm Ti layer with a nSLD of $-0.042 \cdot 10^{-6} \mathring{A}^2$, a 15.80 nm iron oxide with a nSLD of $3.36 \cdot 10^{-6} \mathring{A}^2$, a mSLD of $0.44 \cdot 10^{-6} \mathring{A}^2$ and a 15.70 nm Au layer with a nSLD of $2.56 \cdot 10^{-6} \mathring{A}^2$. The roughness of each layer is indicated by the gradient slop of the SLD curve.
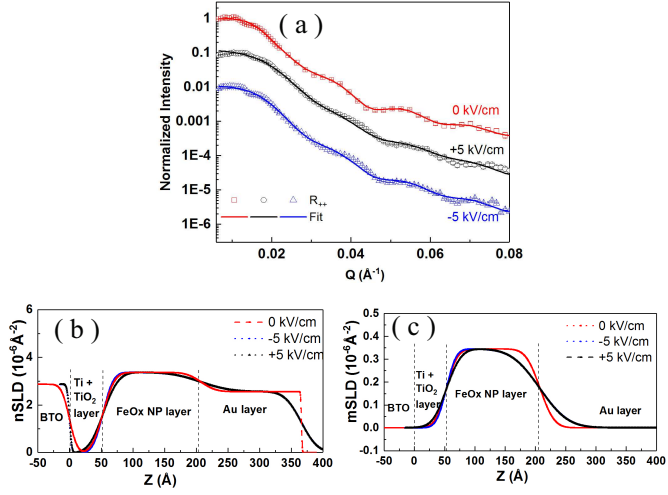
Figure 6: PNR data of the BTO / Ti / NP / Au sample at 300 K at saturation field. (a) Reflectivity and the fit for electric field of 0 KV/cm, +5 KV/cm and -5 KV/cm (b) nSLD obtained from the fit (c) mSLD obtained from the fit. The dashed lines in (b) and (c) indicate the interfaces of each two layers

The PNR data and the fit by the default model under the saturation magnetic field and different electric field are shown in Figure 6(a).

Compared to the fit of Figure 4, all the parameters are fixed except the mSLD of NP layer, the roughness of each layer. The SLD profiles obtained from the best fit are shown in Figure 6(b) and (c), the similar conclusion on roughness of the saturation field is obtained. The mSLD of the NP layer under different electric field are the same which indicate the electric field is hard to tune the spin structures of NPs after the NPs are saturated.

G. PNR Fit parameters by two models

The parameter of the PNR fits are presented in the following tables.

Table 1: PNR 300 K at saturation field and $E = 0$ KV/cm

Parameter	Spherical model		Default model	
	Value	Fit	Value	Fit
Dens_{sub}	0.05946 atom/Å^3	True	0.05493 atom/Å^3	True
Sig_{sub}	13.01296 Å	True	20.99000 Å	True
Th_{Au}	36.69360 Å	True	157.22000 Å	True
Dens_{Au}	0.07363 atom/Å^3	True	0.03250 atom/Å^3	True
Sig_{Au}	0.45627 Å	True	1.52040 Å	True
Th_{Ti}	75.00000 Å	True	52.76200 Å	True
Dens_{Ti}	0.00206 atom/Å^3	True	0.003000 atom/Å^3	True
Sig_{Ti}	10.32880 Å	True	13.2550000 Å	True
$\text{Th}_{FiMlayer}$ [*1]	250.93593 Å	True	158.9300 Å	True
$\text{Sig}_{FiMlayer}$	1.34625 Å	True	35.14900 Å	True
$\text{maxDens}_{FiMlayer}$	0.08544 atom/Å^3	True	0.00918 atom/Å^3	True
$\text{minDens}_{FiMlayer}$	0.00414 atom/Å^3	True	\	\
$\text{Mag}_{FiMlayer}$	1.00602 μ_B/atom	True	1.22420 μ_B/atom	True
$\text{Magangle}_{FiMlayer}$	62.82374 degree	True	47.99685 degree	True
Sig_{sphere}	4.37180 Å	True	\	\
Slices	39	True	\	\

[*1] 'FiMlayer' with respect to the default model hereby and in the following indicate the layer $(Fe_2O_3)_{0.8}$ $(Fe_3O_4)_{0.15}$ $(Fe_xO)_{0.05}$ while it indicate the layer $0.7((Fe_2O_3)_{0.8}$ $(Fe_3O_4)_{0.15}$ $(Fe_xO)_{0.05}) \cdot 0.3$ Au with respect to the spherical model.
Dens_{sub} indicates the atomic density, the nuclear scattering length density is calculated by atomic density times nuclear scattering length. Sig_{sub} represents the roughness of the BTO substrate.
Th_{Au}, Dens_{Au} and Sig_{Au} indicates the thickness, the nuclear scattering density and roughness of the Au layer The same parameters apply for Ti layer.
For FiM layer, Slices indicates the number of slices averagely divided in fitting process. The $\text{maxDens}_{FiMlayer}$ and $\text{minDens}_{FiMlayer}$ in spherical model in used to give the gradient of the nuclear scattering density of the slices under the spherical function. $\text{Mag}_{FiMlayer}$ indicates the magnetic scattering density of the FiM layer. $\text{Magangle}_{FiMlayer}$ represents direction of the magnetic moment with respect to the in-plane x-axis.

Table 2: PNR 300 K at coercive field and $E = 0$ KV/cm

Parameter	Spherical model		Default model	
	Value	Fit	Value	Fit
Dens_{sub}	0.05946 atom/Å^3	False	0.05493 atom/Å^3	False
Sig_{sub}	13.01296 Å	False	20.99000 Å	False
Th_{Au}	36.69360 Å	False	157.22000 Å	False
Dens_{Au}	0.06519 atom/Å^3	True	0.016899 atom/Å^3	True
Sig_{Au}	1.00538 Å	True	0.013549 Å	True
Th_{Ti}	75.00000 Å	False	52.76200 Å	False
Dens_{Ti}	0.00206 atom/Å^3	False	0.003000 atom/Å^3	False
Sig_{Ti}	10.45924 Å	True	13.2550000 Å	True
$\mathrm{Th}_{FiMlayer}$	250.93593 Å	False	158.9300 Å	False
$\mathrm{Sig}_{FiMlayer}$	0.64299 Å	True	35.14900 Å	True
$\mathrm{maxDens}_{FiMlayer}$	0.08544 atom/Å^3	False	0.00918 atom/Å^3	False
$\mathrm{minDens}_{FiMlayer}$	0.00414 atom/Å^3	False	\	\
$\mathrm{Mag}_{FiMlayeru}$	0.36963 μ_B/atom	True	1.18500 μ_B/atom	True
$\mathrm{Magangle}_{FiMlayer}$	65.71860 degree	True	37.09585 degree	True
Sig_{sphere}	4.51679 Å	True	\	\
Slices	45	True	\	\

Table 3: PNR 300 K at coercive field and $E = +5$ KV/cm

Parameter	Spherical model		Default model	
	Value	Fit	Value	Fit
Dens_{sub}	0.05946 atom/Å^3	False	0.05493 atom/Å^3	False
Sig_{sub}	3.99891 Å	True	20.99000 Å	True
Th_{Au}	36.69360 Å	False	157.22000 Å	False
Dens_{Au}	0.04524 atom/Å^3	True	0.016899 atom/Å^3	False
Sig_{Au}	8.00050 Å	True	12.52170 Å	True
Th_{Ti}	75.00000 Å	False	52.76200 Å	False
Dens_{Ti}	0.00206 atom/Å^3	False	0.003000 atom/Å^3	False
Sig_{Ti}	3.69725 Å	True	0.73500 Å	True
$\mathrm{Th}_{FiMlayer}$	250.93593 Å	False	158.9300 Å	False
$\mathrm{Sig}_{FiMlayer}$	9.17690 Å	True	38.26950 Å	True
$\mathrm{maxDens}_{FiMlayer}$	0.08544 atom/Å^3	False	0.00918 atom/Å^3	False
$\mathrm{minDens}_{FiMlayer}$	0.00414 atom/Å^3	False	\	\
$\mathrm{Mag}_{FiMlayer}$	0.30116 μ_B/atom	True	0.98005 μ_B/atom	True
$\mathrm{Magangle}_{FiMlayer}$	74.72129 degree	True	15.09585 degree	True
Sig_{sphere}	4.34233 Å	True	\	\
Slices	45	True	\	\

Table 4: PNR 300 K at coercive field and E = -5 KV/cm

Parameter	Spherical model		Default model	
	Value	Fit	Value	Fit
Dens_{sub}	0.05946 atom/Å^3	False	0.05493 atom/Å^3	False
Sig_{sub}	3.59275 Å	True	20.99000 Å	False
Th_{Au}	36.69360 Å	False	157.22000 Å	False
Dens_{Au}	0.04419 atom/Å^3	True	0.016899 atom/Å^3	False
Sig_{Au}	0.04400 Å	True	11.69180 Å	True
Th_{Ti}	75.00000 Å	False	52.76200 Å	False
Dens_{Ti}	0.00206 atom/Å^3	False	0.003000 atom/Å^3	False
Sig_{Ti}	2.61132 Å	True	0.60500 Å	True
$\mathrm{Th}_{FiMlayer}$	250.93593 Å	False	158.9300 Å	False
$\mathrm{Sig}_{FiMlayer}$	7.31541 Å	True	39.15760 Å	True
$\mathrm{maxDens}_{FiMlayer}$	0.08544 atom/Å^3	False	0.00918 atom/Å^3	False
$\mathrm{minDens}_{FiMlayer}$	0.00414 atom/Å^3	False	\	\
$\mathrm{Mag}_{FiMlayer}$	0.23356 μ_B/atom	True	0.945105 μ_B/atom	True
$\mathrm{Magangle}_{FiMlayer}$	79.50890 degree	True	17.13585 degree	True
Sig_{sphere}	4.42618 Å	True	\	\
Slices	42	True	\	\

Table 5: PNR 300 K at saturation field and E = +5 KV/cm

Parameter	Spherical model		Default model	
	Value	Fit	Value	Fit
Dens_{sub}	0.05946 atom/Å^3	False	0.05493 atom/Å^3	False
Sig_{sub}	3.79997 Å	True	21.05420 Å	True
Th_{Au}	36.69360 Å	False	157.22000 Å	False
Dens_{Au}	0.04519 atom/Å^3	True	0.03250 atom/Å^3	True
Sig_{Au}	6.00001 Å	True	16.30140 Å	True
Th_{Ti}	75.00000 Å	False	52.76200 Å	False
Dens_{Ti}	0.00206 atom/Å^3	False	0.003000 atom/Å^3	False
Sig_{Ti}	3.05024 Å	True	0.62500 Å	True
$\mathrm{Th}_{FiMlayer}$	250.93593 Å	False	158.9300 Å	False
$\mathrm{Sig}_{FiMlayer}$	6.24733 Å	True	29.24690 Å	True
$\mathrm{maxDens}_{FiMlayer}$	0.08544 atom/Å^3	False	0.00918 atom/Å^3	False
$\mathrm{minDens}_{FiMlayer}$	0.00414 atom/Å^3	False	\	\
$\mathrm{Mag}_{FiMlayer}$	0.35097 μ_B/atom	True	1.248082 μ_B/atom	True
$\mathrm{Magangle}_{FiMlayer}$	57.44762 degree	True	13.45870 degree	True
Sig_{sphere}	4.11567 Å	True	\	\
Slices	57	True	\	\

Table 6: PNR 300 K at saturation field and E = -5 KV/cm

Parameter	Spherical model		Default model	
	Value	Fit	Value	Fit
Dens_{sub}	0.05946 atom/Å^3	False	0.05493 atom/Å^3	False
Sig_{sub}	3.76461 Å	True	21.05420 Å	True
Th_{Au}	36.69360 Å	False	157.22000 Å	False
Dens_{Au}	0.04524 atom/Å^3	True	0.03250 atom/Å^3	True
Sig_{Au}	0.13446 Å	True	15.16400 Å	True
Th_{Ti}	75.00000 Å	False	52.76200 Å	False
Dens_{Ti}	0.00206 atom/Å^3	False	0.003000 atom/Å^3	False
Sig_{Ti}	3.28260 Å	True	0.62500 Å	True
$\text{Th}_{FiMlayer}$	250.93593 Å	False	158.9300 Å	False
$\text{Sig}_{FiMlayer}$	7.24733 Å	True	28.54590 Å	True
$\text{maxDens}_{FiMlayer}$	0.08544 atom/Å^3	False	0.00918 atom/Å^3	False
$\text{minDens}_{FiMlayer}$	0.00414 atom/Å^3	False	\	\
$\text{Mag}_{FiMlayer}$	0.36202 μ_B/atom	True	0.903805 μ_B/atom	True
$\text{Magangle}_{FiMlayer}$	57.58486 degree	True	10.15070 degree	True
Sig_{sphere}	4.92358 Å	True	\	\
Slices	57	True	\	\

Acknowledgements

I would like to sincerely thank Prof. Dr. Thomas Brückel for leading me to the field of neutron scattering and providing me the opportunity to work at the Jülich Center for Neutron Science, I want to thank him also for supporting me to travel to different places and to participate conferences and beamtimes.

I would like to thank Prof. Joachim Mayer for the efforts to accept the second revision of the thesis.

Special appreciations I would like to give to my supervisor Dr. Oleg Petracic for all the support and the discussions during my thesis. I am very grateful for his patience and the elaborate explanations in every discussion. I thank you for the careful revisions of my thesis. The four years of research with you was fruitful and has a profound meaning for my future scientific career.

Many thanks to Dr. Stefan Mattauch and Dr. Alexandros Koutsioumpas for the scientific support during the neutron reflectivity measurements performed at MARIA in MLZ and especially to the discussions about the results afterwards.

Many thanks to Dr. Emmanuel Kentzinger for the help with GISAXS measurements, thanks to Marina Ganeva and Asma Qdemat for the help with data reduction and fitting.

I thank Berthold Schmitz for the help on the instruments.

I would like to thank Prof. C. Schneider (PGI-6) for providing us the opportunity to use their equipment.

I thank XianKui Wei, Fengshan Zheng and Penghan Lu for the help with TEM, STEM and electron holography measurements.

I give my thanks to Dr. Yinguo Xiao for the help on CCMS measurements.

I would like to thank all my Chinese colleges Dr. Yinguo Xiao, Xiao Sun, Wenhai Ji, Lei Cao and Erxi Feng. Thank you for all the pleased moments we had together, the scientific atmosphere with a lot of fun was always very motivating.

I want to thank all the members of the institute JCNS-2 for both the rigorous scientific environment and a lovely research atmosphere.

Financial support from China Scholarship Council (CSC) is gratefully acknowledged.

Last but not least I would like to thank my parents for always supporting and encouraging me at my back.

Schriften des Forschungszentrums Jülich
Reihe Schlüsseltechnologien / Key Technologies

Schriften des Forschungszentrums Jülich
Reihe Schlüsseltechnologien / Key Technologies

Band / Volume 174
Interfacing EuO in confined oxide and metal heterostructures
P. Lömker (2018), vi, 140 pp
ISBN: 978-3-95806-337-2

Band / Volume 175
**Operando Chemistry and Electronic Structure
of Electrode / Ferroelectric Interfaces**
S. Gonzalez (2018), 159 pp
ISBN: 978-3-95806-341-9

Band / Volume 176
**Magnetic Properties of Self-assembled Manganese Oxide
and Iron Oxide Nanoparticles**
Spin Structure and Composition
X. Sun (2018), ii, 178 pp
ISBN: 978-3-95806-345-7

Band / Volume 177
**Model-based reconstruction of magnetisation distributions
in nanostructures from electron optical phase images**
J. Caron (2018), XXI, 183 pp
ISBN: 978-3-95806-346-4

Band / Volume 178
**Simultaneous dual-color imaging on single-molecule level
on a Widefield microscope and applications**
R. Ledesch (2018), ix, 119 pp
ISBN: 978-3-95806-348-8

Band / Volume 179
**Methoden der Leitfähigkeitsuntersuchung mittels Rasterkraftmikroskop
und deren Anwendung auf Barium Titanat Systeme**
B. Reichenberg (2018), x, 144 pp
ISBN: 978-3-95806-350-1

Band / Volume 180
**Manipulation of magnetism in iron oxide nanoparticle / BaTiO$_3$
composites and low-dimensional iron oxide nanoparticle arrays**
L. Wang (2018), VI, 151 pp
ISBN: 978-3-95806-351-8

Weitere *Schriften des Verlags im Forschungszentrum Jülich* unter
http://wwwzb1.fz-juelich.de/verlagextern1/index.asp

JÜLICH
Forschungszentrum